Engineered spin and orbital currents in epitaxial IrO_2 thin film heterostructures

by

Michael Vincent Patton

A dissertation submitted in partial fulfillment

of the requirements for the degree of

Doctor of Philosophy

(Materials Science and Engineering)

at the

University of Wisconsin-Madison

2024

Date of Final Oral Exam: 06/24/2024

The dissertation is approved by the following members of the Final Oral Committee:

Chang-Beom Eom, Professor, Materials Science and Engineering

Mark Rzchowski, Professor, Physics

Jason Kawasaki, Associate Professor, Materials Science and Engineering

Jiamian Hu, Professor, Materials Science and Engineering

Evgeny Tsymbol, Professor, UNL - Physics and Astronomy

Abstract

Spintronic devices that utilize the spins of electrons as an additional degree of freedom for logic, memory, sensor, and other technologies are a promising avenue for highly efficient low power consumption electronics. Understanding the relationship between the crystal structure and spin transport relationship is critical for developing highly efficient spintronic materials. Additionally, studying orbital current may be just as important for technological spintronic advances due to the intricate relationship between the two properties. Many different material platforms have shown unique spin transport phenomena such as heavy metals (Pt, W, etc.) for highly efficient charge-spin conversion, low symmetry materials such as transition metal dichalcogenides and antiferromagnets for unconventional spin-orbit torque, and light metals (Ti, Cr, etc.) have shown large orbital currents that have similar properties and applications as spin currents. However, studying all three of these properties and the relationship to crystallographic symmetries has not been achieved in a single material before. In this thesis, I present a detailed study on IrO_2, a heavy semimetal oxide demonstrating large spin-charge conversion and is able to generate unconventional spin and orbital currents making it an ideal platform for understanding and developing next generation spintronic devices.

Crystal symmetries can restrict the polarization of spin currents to only be along certain directions. However, for applications such perpendicular magnetic switching that requires the spin to be polarized out-of-plane, high symmetry materials won't work. We show that using epitaxial design in higher symmetry materials, where the crystal orientation and

relative crystal symmetries can be controlled, can lead to large unconventional spin-orbit torques. This work, discussed in Chapter 3 of this thesis, highlights which crystal symmetries to avoid in spintronic materials to generate unconventional spin currents by studying IrO_2 in the (001), (110), and (111) orientations. Additionally, we can predict the conventional and unconventional spin Hall conductivity for any orientation (i.e. (110), (101), (111)) with high accuracy using the experimental results from the high symmetry orientations (001) and (100). This work, which is discussed in Chapter 4, demonstrates that the spin Hall conductivity truly is an intrinsic property of IrO_2 and follows the crystalline symmetries as we would expect, which has not been demonstrated before.

Orbital currents have recently been shown in several material platforms including light element metals which have dominating orbital currents compared to spin currents. However, few to no studies have looked at orbital currents in materials with high spin-charge conversion. Additionally, no studies have demonstrated unconventional orbital currents. We show evidence for large conventional as well as unconventional spin and orbital currents in IrO_2. These results, discussed in Chapter 5, agree with theoretical calculations and demonstrate the interplay between spin and orbital currents.

Field-free switching of perpendicular magnetic materials has promising applications for highly efficient and low power consumption spintronics devices. Field-free switching have been achieved in low symmetry materials such as antiferromagnets, transition metal dichalcogenides, magnetic trilayers, and other low crystalline symmetry materials. However, the z-spin polarized spin-orbit torque that is required to switch out-of-plane magnetic moments have typically been small leading to large current densities which is a

disadvantage for commercial applications. Chapter 6 demonstrates field-free perpendicular magnetic switching using $IrO_2(111)/[Pt/Co]_N/Pt$ heterostructures.

Acknowledgements

I would like to thank my advisor, Prof. Chang-Beom Eom, for all of his guidance and commitment towards making me a better researcher. Chang-Beom's efforts towards developing his students has not only affected me during my graduate studies but also my undergraduate development where I had the chance to be mentored by his former undergraduate researcher, Prof. Brittany Nelson-Cheeseman. Making the switch from mechanical engineering to condensed matter physics was not easy. However, Chang-Beom's patience as I gained knowledge in his area of expertise was critical for my development in this field. I would also like to thank the other committee members including Prof. Mark Rzchowski, Prof. Evgeny Tsymbol, Prof. Jason Kawasaki, and Prof. Jiamian Hu for their insightful discussion to push my research to higher impact.

Additionally, I would like to thank my collaborator Prof. Tianxiang Nan who trained and mentored me on the fundamentals of spintronics and spintronic measurements. Tian has not only provided critical data and measurements needed for my publications, but also has shared their expertise and expanded my knowledge in his research areas. I would also like to thank collaborators at Cornell including Prof. Dan Ralph for his extensive efforts additional spintronic measurements and manuscript revisions. Dan has been a great mentor offering his expertise in the field of spintronics and has guided me to be a better researcher and critical thinker. I would also like to thank his student, Dan Pharis, for the spintronic measurements for several of my manuscripts. I would also like to thank all of the theorists including Prof. Evgeny Tsymbol, Gautam Gurung, Ding-Fu Shao, Prof. Yuriy Mokrousov, and

Dongwook Go, that have provided not only critical theoretical calculations for my work, but also their fundamental understanding of spintronics and condensed matter physics.

I would also like to thank all of the current and former Oxide lab members for providing their expertise and guidance towards making me a better researcher. I would like to specifically thank Anthony Edgeton, Shane Lindemann, Jonathan Schad, and Patrick Strohbeen for not only their guidance but also being great friends outside of the lab. Lastly, I would like to thank my friends and family for their support during my time in graduate school including my mother Prof. Corrine Carvalho, my father John Patton, my sister Julie Marka, and my fiancé Naomi Kahnke. All of their love and support helped me along the way and I am grateful for them.

Table of Contents

List of Figures

Chapter 1 Introduction

1.1 Introduction to spintronics

Spintronics uses the spins of electrons as an additional degree of freedom that can act as a probe for information processing and manipulate magnetic materials for higher efficient memory devices which is promising for next generation electronics such as transistors, data storage, magnetic random access memory (MRAM), and quantum computing. Some of the most notable spintronic mechanisms useful for next generation electronics include giant and tunneling magnetoresistance, spin transfer torque, spin Hall effect, Rashba effect, and spin Seebeck effect. Of these effects, the spin Hall effect (SHE), where a spin-polarized current is generated from a transverse charge current, is an intrinsic mechanism in materials with large spin orbit coupling (SOC) that can be used to exert torque on adjacent magnetic materials. [1,2,3]

Spin-orbit torques generated by a spin current are key to magnetic switching in spintronic applications. The polarization of the spin current dictates the direction of switching required for energy-efficient devices. Conventionally, the polarizations of these spin currents are restricted to be along a certain direction due to the symmetry of the material allowing only for efficient in-plane magnetic switching. Unconventional spin-orbit torques arising from novel spin current polarizations, however, have the potential to switch other magnetization orientations such as perpendicular magnetic anisotropy which is desired for higher density spintronic-based memory devices. To date, these unconventional spin polarizations have only been observed intrinsically in materials with low crystalline symmetry or magnetic

ordering, limiting the potential materials that can be integrated in next generation spintronic devices. [4,5,6,7,8,9 10,11,12,13,14]

Measuring spin orbit torques can be done by detecting the magnetic dynamics of an adjacent ferromagnetic as spins are pumped into it. The magnetic dynamics under applied magnetic fields in the presence of damping-like spin orbit torques can be modelled using the Landau-Lifshitz-Gilbert-Slonczewski equation:

$$\frac{dM}{dt} = -\gamma M \times H_{eff} + \alpha M \times \frac{dM}{dt} + \tau_{DL} M \times (\sigma \times M) \qquad (1)$$

Where M is the magnetization, γ is the gyromagnetic ratio, H_{eff} is the applied magnetic field, α is the Gilbert damping coefficient, τ_{DL} is the damping-like torque coefficient, and σ is the polarization direction of the spin current. There are several techniques to experimentally determine this, the most common being spin torque ferromagnetic resonance measurements.

1.2 Spin Torque Ferromagnetic Resonance (ST-FMR)

During the ST-FMR measurements, a microwave current is applied at a fixed frequency and fixed power while sweeping an in-plane magnetic field through the ferromagnetic resonance conditions. The microwave current was modulated at a fixed frequency which can be detected using a lock-in amplifier by measuring the DC mixing voltage across the device at the same modulated frequency. The mixing voltage was fitted vs applied field to extract the symmetric and antisymmetric Lorentzian components. Conventionally, torques generated from Oersted fields acting on the magnetization are in the form of $\boldsymbol{m} \times \boldsymbol{y}$ where $\boldsymbol{y}$ is an in-plane direction perpendicular to the charge current direction $\boldsymbol{x}$ resulting in a field-like

torque ($\tau_\perp$). In addition to the out-of-plane torques, spin currents resulting from the SHE (or other spin generating effects) can also generate torques in the form of $\boldsymbol{m} \times (\boldsymbol{m} \times \boldsymbol{y})$ resulting in a damping-like torque ($\tau_\parallel$). The out-of-plane ($\tau_\perp$) and the in-plane ($\tau_\parallel$) torques are proportional to the mixing voltage V_{mix} as the ferromagnetic layer goes through its resonance condition which can be fitted as a sum of a symmetric and an antisymmetric Lorentzian:

$$V_{mix,S} = -\frac{I_{rf}}{2}\left(\frac{dR}{d\varphi}\right)\frac{1}{\alpha(2\mu_0 H_{FMR}+\mu_0 M_{eff})}\tau_\parallel \quad (2)$$

$$V_{mix,A} = -\frac{I_{rf}}{2}\left(\frac{dR}{d\varphi}\right)\frac{\sqrt{1+M_{eff}/H_{FMR}}}{\alpha(2\mu_0 H_{FMR}+\mu_0 M_{eff})}\tau_\perp \quad (3)$$

Where R is the resistance of the device, φ is the magnetization angle with respect to the applied current, α is the Gilbert damping coefficient, $\mu_0 H_{FMR}$ is the resonance field, and $\mu_0 M_{eff}$ is the effective magnetization. The effective magnetization of Py can be obtained using Kittel's equation $f = \frac{\gamma}{2\pi}\sqrt{(H_{FMR}+H_K)(H_{FMR}+H_K+M_{eff})}$ where γ is the gyromagnetic ratio and H_K is the in-plane anisotropy field. The Gilbert damping coefficient α is obtained by fitting the linear relationship between the linewidth (w) and the frequency $w = w_0 + \left(\frac{2\pi}{\gamma}\right) * f$. Calibration of the microwave current (I_{rf}) can be determined by measuring the resistance change due to Joule heating across the Hall bar device while varying the microwave power.[151613] We can then find $I_{rf} = \sqrt{2} I_{dc}$ due to the joule heating relationship between AC and DC current.

To quantitatively determine all torque contributions, ST-FMR measurements were performed as a function of applied in-plane magnetic field angle (φ). In conventional heavy-

metal/ferromagnetic bilayers the AMR of the ferromagnetic layer ($\frac{dR}{d\varphi}$) has an angular dependance proportional to sin(2φ) and the out-of-plane ($\tau_{\perp}$) and the in-plane ($\tau_{\parallel}$) torques are proportional to cos(φ) resulting in the $V_{mix,S}$ and $V_{mix,A}$ being in the form of sin (2φ)cos(φ). Additional unconventional torques that have different spin polarization directions, however, can contribute to the angular dependance resulting in a more general form of the angular dependance:

$$\tau_{\parallel} = \tau_{x,AD}\sin(\varphi) + \tau_{y,AD}\cos(\varphi) + \tau_{z,FL} \quad (4)$$

$$\tau_{\perp} = \tau_{x,FL}\sin(\varphi) + \tau_{y,FL}\cos(\varphi) + \tau_{z,AD} \quad (5)$$

$V_{mix,S}$ and $V_{mix,A}$ can then be expressed in the form of $\sin(2\varphi)(\tau_{x,AD}\sin(\varphi) + \tau_{y,AD}\cos(\varphi) + \tau_{z,FL})$ and $\sin(2\varphi)(\tau_{x,FL}\sin(\varphi) + \tau_{y,FL}\cos(\varphi) + \tau_{z,AD})$, respectively.

DC-tuned ST-FMR measurements are an alternative approach to characterize the spin Hall angle of a material where a DC current is applied along with the RF current via a bias tee during ST-FMR measurements. Some oxide substrates including $SrTiO_3$, $KTaO_3$, and TiO_2 have high dielectric loss resulting in current shunting when using high frequency rf currents, which can lead to a large symmetric V_{mix} during ST-FMR measurements[17]. DC tuned measurements have been used as an independent way to measure the spin Hall conductivity which applies a constant dc current in addition to the rf current during ST-FMR measurements, which can be used to isolate the true SHC of a material as the rf current shunting should not be affected by the applied dc current[17–19]. The linear relationship between the linewidth of the mixing voltage signal during ST-FMR measurements and the DC current can be used to determine the SHC. The spin Hall angle can be determined using the following equation:

$$\theta_{DL} = \frac{2e}{\hbar}\left(\frac{(H_{FMR} + \frac{M_{eff}}{2})\mu_0 M_s t_{Py}}{\sin(\varphi)}\right)\frac{\Delta\alpha_{eff}}{\Delta J_c} \quad (6)$$

Where t_{Py} is the thickness of permalloy and $\frac{\Delta\alpha_{eff}}{\Delta J_c}$ is the linear slope of effective damping coefficient, determined from the linear relationship between the linewidth (w) and the frequency $w = w_0 + \left(\frac{2\pi}{\gamma}\right) * f$, vs the charge current going through the spin source material layer determined using parallel resistor model.

1.3 Density Functional Theory (DFT) calculations

DFT calculations were performed using a Quantum-ESPRESSO code[20]. The plane-wave pseudopotential method with the fully relativistic ultrasoft pseudopotentials[21] was employed in the calculations. The exchange and correlation effects were treated within the generalized gradient approximation (GGA)[22]. The plane-wave cut-off energy of 40 Ry and a 16 × 16 × 16 k-point mesh in the irreducible Brillouin zone were used in the calculations. Spin-orbit coupling was included in all the calculations.

The spin Hall effect is given by:

$$\sigma_{ij}^{k} = \frac{e^2}{\hbar}\int \frac{d^3\vec{k}}{(2\pi)^3}\sum_n f_{n\vec{k}}\Omega_{n,ij}^{k}(\vec{k}), \quad (7)$$

$$\Omega_{n,ij}^{k}(\vec{k}) = -2Im\sum_{n\neq n'}\frac{\langle n\vec{k}|J_i^k|n'\vec{k}\rangle\langle n'\vec{k}|v_j|n\vec{k}\rangle}{\left(E_{n\vec{k}} - E_{n'\vec{k}}\right)^2} \quad , \quad (8)$$

where $f_{n\vec{k}}$ is the Fermi-Dirac distribution for the *n*th band, $J_i^k = \frac{1}{2}\{v_i, s_k\}$ is the spin current operator with spin operator s_k, $v_j = \frac{1}{\hbar}\frac{\partial H}{\partial k_j}$ is the velocity operator, and $i, j, k = x, y, z$. $\Omega_{n,ij}^{k}(\vec{k})$

is referred to as the spin Berry curvature in analogy to the ordinary Berry curvature. In order to calculate the spin Hall conductivities, we construct the tight-binding Hamiltonians using PAOFLOW code[23,24] based on the projection of the pseudo-atomic orbitals (PAO) from the non-self-consistent calculations with a 16 × 16 × 16 *k*-point mesh. The spin Hall conductivities were calculated using the tight-binding Hamiltonians with a 48 × 48 × 48 *k*-point mesh by the adaptive broadening method to get the converged values. The elements of the spin Hall conductivity tensors for different plane $[111]$, $[110]$ etc. can be transformed from the spin Hall conductivity tensors of [001] plane as

$$\sigma^{s}_{ij,[plane]} = \sum_{l,m,n} R_{il} R_{jm} R_{kn}\, \sigma^{s}_{lm,[001]}, \tag{9}$$

Where *i* is the spin current direction j is the charge current direction, *s* is the spin polarization direction, and R_{il} is an element of the rotation matrix R which transforms from [001] to the desired orientation.

1.4 Spintronic properties of IrO_2

Rutile iridium dioxide (IrO_2), a non-magnetic metallic oxide, has been shown to have a large spin-charge conversion efficiency and high electrical conductivity making this material promising for spintronic applications[25,26,27,28,29]. Due to the 5d orbitals in IrO_2, large spin orbit coupling along with other properties related to the Berry curvature result in a large intrinsic SHE.[30–33] There have been several reports of spintronic measurements in IrO_2 including polycrystalline[34,35], in both the (001) and (110) orientations showing the anisotropy of the spintronic properties[32], as well as in (100) semi-epitaxial IrO_2[36]. These results demonstrate not only the existence of a large SHE, but also the anisotropy of the spintronic properties due

to the anisotropy of the crystal structure. IrO_2 (space group $P4_2/mnm$ No. 136) has a tetragonal rutile crystal structure with mirror symmetry (m) along the (001), (110), and (1-10) planes, two-fold rotational symmetries along (C_2) [001],[110] and [1-10], and nonsymmorphic symmetries that include a fourfold rotational screw axis ($\tilde{C}_4$) along [001] and glide mirror planes along the ($\tilde{m}$) (100) and (010) planes. Combinations of these symmetry elements in high symmetry orientations forbid any unconventional SOTs arising from the bulk of the material. These symmetries and their influence on the spintronic properties will be discussed in Chapter 3.

Chapter 2 Growth and characterization of IrO_2 epitaxial thin films

2.1 RF magnetron sputtering

All of IrO_2 the results throughout this thesis have been grown epitaxially single-crystal TiO_2 substrates via RF magnetron sputtering using the growth conditions mentioned in this section. The chamber used for IrO_2 deposition can be seen in Figure 2.1a which is equipped with 4 confocal 1.3" on-axis sputtering guns seen in Figure 2.1b where the center gun is the IrO_2 target, left is ferromagnetic Permalloy (Py) or nickel (Ni), right is RuO_2, and the back is platinum (Pt). The IrO_2 films were grown at temperatures between 300-400°C, at a pressure of between 15-30 mTorr, and with 10% oxygen partial pressure at a background pressure of ~3E-7 Torr. The target used was a 1.3" diameter ceramic IrO_2 target from RHP Technology at a power of 20 W with 150-200V DC bias. The substrate was heated up 300°C prior to every growth and held for ~15 minutes to remove any surface contamination. After growth the sample was cooled in an O_2 atmosphere. For heterostructures such as IrO_2/Py, the chamber was again pumped down to ~3E-7 Torr without breaking vacuum for in situ growth.

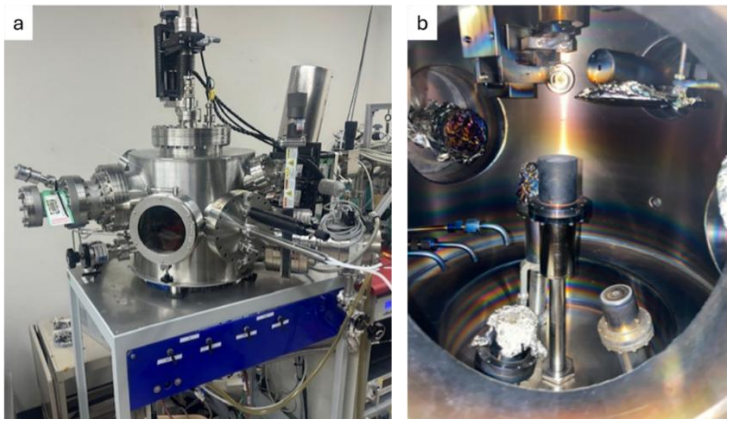

Figure 2.1: a sputtering chamber used to grow up to 4 materials using the confocal design seen in b.

2.2 X-ray diffraction (XRD) and atomic force microscopy (AFM)

High resolution x-ray diffraction (HR-XRD) was done in our lab using the Bruker D8 Davinci diffractometer. Fully epitaxial IrO_2 samples were achieved for (001), (100), (110), (101), and (111) oriented films and with out-of-plane HR-XRD seen in Figure 2.2a-e with each orientation showing Kiessig fringes indicating smooth surfaces which agrees with the atomic force microscopy (AFM) of the surfaces of each orientation seen in Figure 2.2f-j. Single phases for each orientation were also confirmed with an out-of-plane 2θ-ω scan from 10° - 100° (not shown).

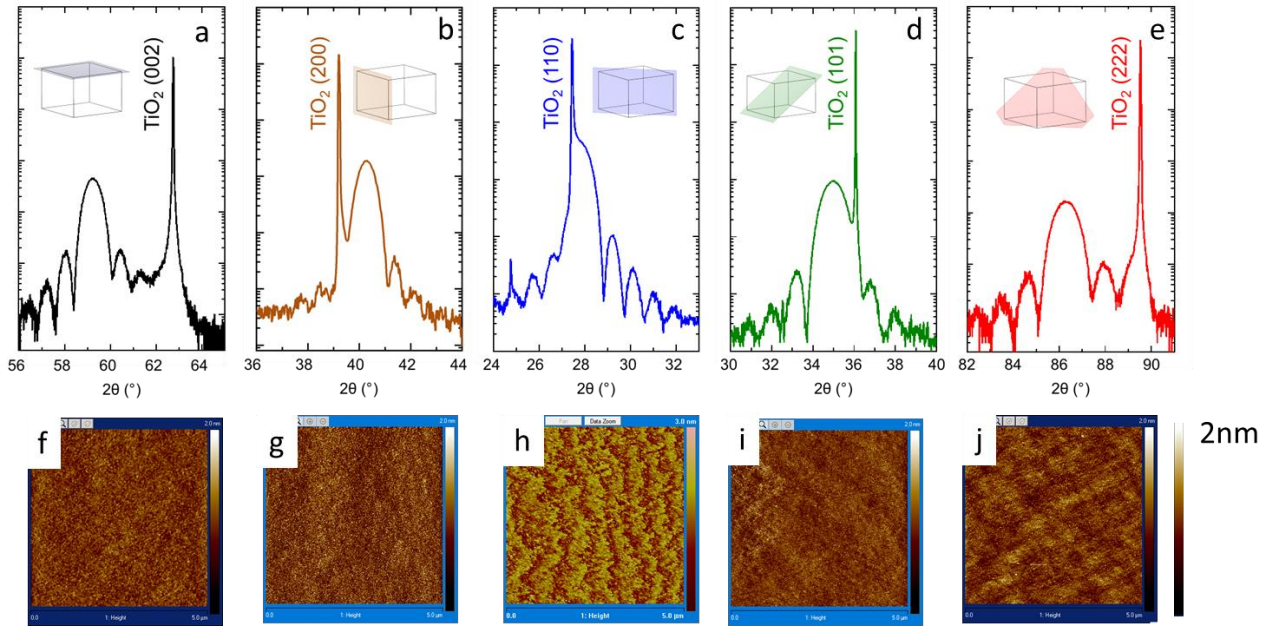

Figure 2.2: a-e out-of-plane XRD for the (001), (100), (110), (101), and (111) IrO_2 orientations and f-j AFM images of the surface with 2nm scale bar.

X-ray diffraction reciprocal space mapping (RSM) was performed on IrO_2 (7-10nm) thin films for all five orientations as shown in Figure 2.3. The (001) orientated IrO_2 shows coherent growth with slight relaxation (not shown). Figure 2.3a and 2.3b show the (001) in-plane strain for the [010] and [001] direction, respectively, where we see fully coherent along the [010]

and full relaxation along the [001] direction. Figure 2.3c and 2.3d show the (110) in-plane strain for the [1-10] and [001] direction, respectively, where we see relaxation along both directions. Figure 2.3e and 2.3f show the (101) in-plane strain for the [010] and [-101] direction, respectively, where we see fully coherent growth. Figure 2.3g and 2.3h show the (111) in-plane strain along the [1-10] and [11-2] directions, respectively, where we see fully coherent growth.

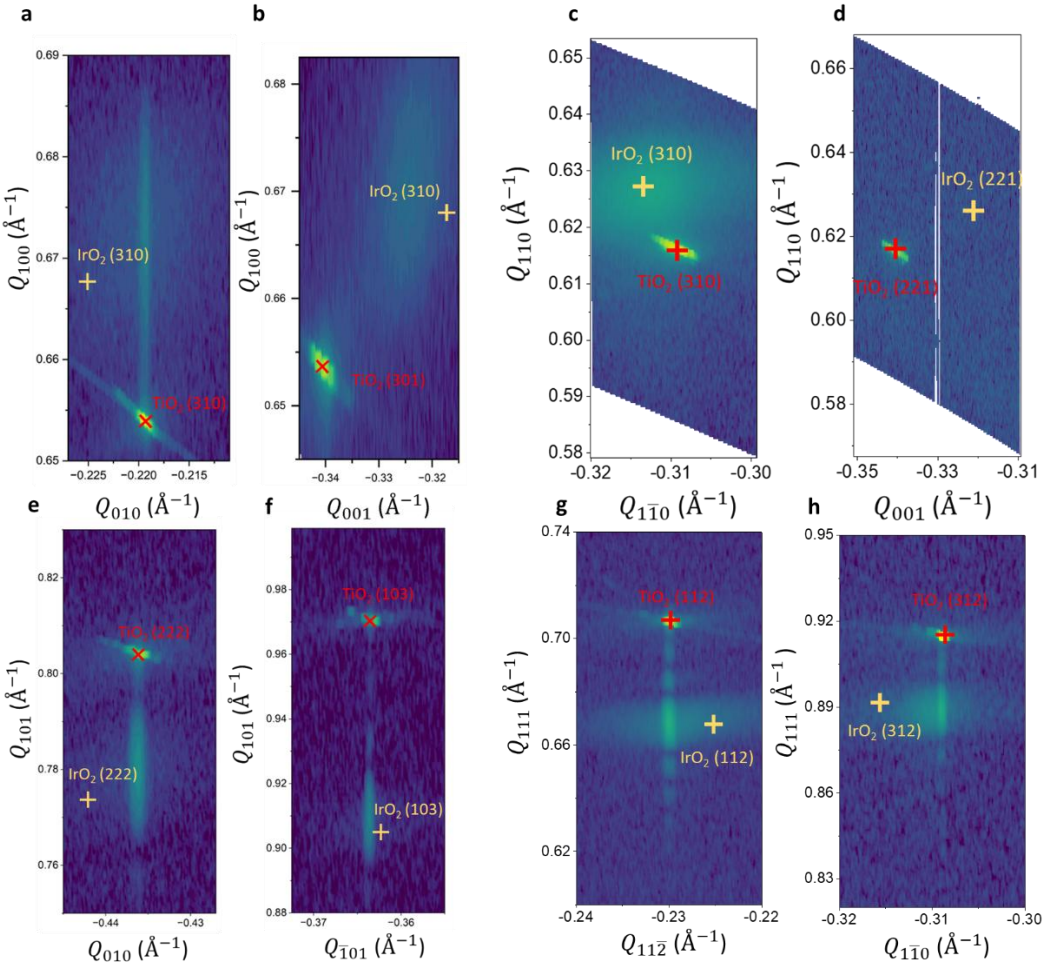

Figure 2.3: a and b RSMs of the (100) orientation, c and d RSMs of the (110) orientation, e and f RSMs of the (101) orientation, and g and h RSMs of the (111) orientation.

2.3 Scanning transmission electron microscopy (STEM)

Scanning transmission electron microscopy (STEM) was done for each orientation which demonstrates the sharp interface between IrO_2 and Py and between IrO_2 and TiO_2, which helps rule out any extrinsic effects that may contribute to the SOTs. Py/IrO_2/TiO_2 interfaces were visualized using STEM (JEM-ARM200F, JEOL) at 200 kV equipped with the aberration corrector (ASCOR, CEOS GmbH). The optimum size of the electron probe was set to be ~0.7 Å. The collection semi-angle of the HAADF detector was ranged from 54 to 216 mrad for clear Z-contrast images. The images were obtained using Smart Align and were conducted on multi-stacking images and aligned these images using rigid registration to correct for drift and scan distortions. The raw STEM images were filtered to reduce background noise by using Difference Filter (Filters Pro, HREM Research Inc., Japan). STEM samples were prepared by mechanical flat polishing and ion milling process. The polished samples were milled using a 3keV Ar ion beam. To minimize surface damage, the samples were milled with an acceleration voltage of 100 meV (PIPS II; Gatan, Pleasanton, CA, USA).

The crystal systems of rutile IrO_2 and rutile TiO_2 are the same tetragonal structure but different lattice constants (a=b=4.594 Å, c=2.959 Å for TiO_2; a=b=4.498 Å, c=3.154 Å for IrO_2) and thus the different strains could be accumulated depending on the substrate orientation. We analyze the strain states of IrO_2 films by using geometric phase analysis (GPA). In the case of IrO_2 (001) film, a and b lattice parameters are same and therefore the strain only through [110] projection is extracted, as shown in Figure 2.4. The strain of IrO_2 film (Figure S2b) is measured compared to the lattice parameter of TiO_2 and therefore the similar colors in IrO_2 and TiO_2 in Figure 2.4b indicate that IrO_2 film is roughly matched with TiO_2 substrate.

Thus, it should be noted that the measured strain from IrO_2 film (Figure 2.4b) is not the real strain. To understand the actual strain, the lattice mismatch between the bulk IrO_2 and the substrate TiO_2 must be plotted together, as indicated by the green line in Figure 2.4c. The black line, obtained by profiling the intensity from the rectangle box of Figure 2.4b becomes comparable to bulk IrO_2 lattice parameter, which means that in-plane tensile strain along [1-10] is applied with slight relaxation.

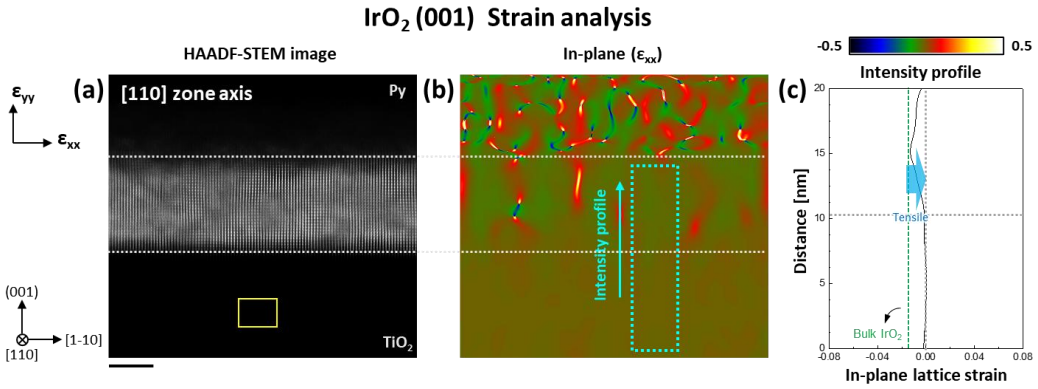

Figure 2.4: Strain analysis in IrO_2 (001) film. a, HAADF-STEM image of IrO_2 (001) films in [110] projection. Scale bar is 5nm. b, Map of in-plane (ε_{xx}) strain analysis of a. c, Intensity profile of In-plane (GPA) image b. The lattice strain is calculated based on the lattice parameter of reference region, which is yellow box in TiO_2 substrate. The interfaces between IrO_2/TiO_2 and Py/IrO_2 are identified by white dashed line. In-plane strain in [1-10] direction is roughly applied.

IrO_2 (100) film experiences anisotropic strain states as shown in Figure 2.5c and Figure 2.5d because the lattice spacings along [001] and [010] are different to ones of TiO_2. The IrO_2 film along [001] is not fully relaxed, exhibiting ~ 2% compressive strain as shown in Figure 2.5e, similar to the strain states in the (110) film along the [001] direction while the IrO_2 film along [010] is mostly coherent with the TiO_2 substrate as shown in Figure 2.5f.

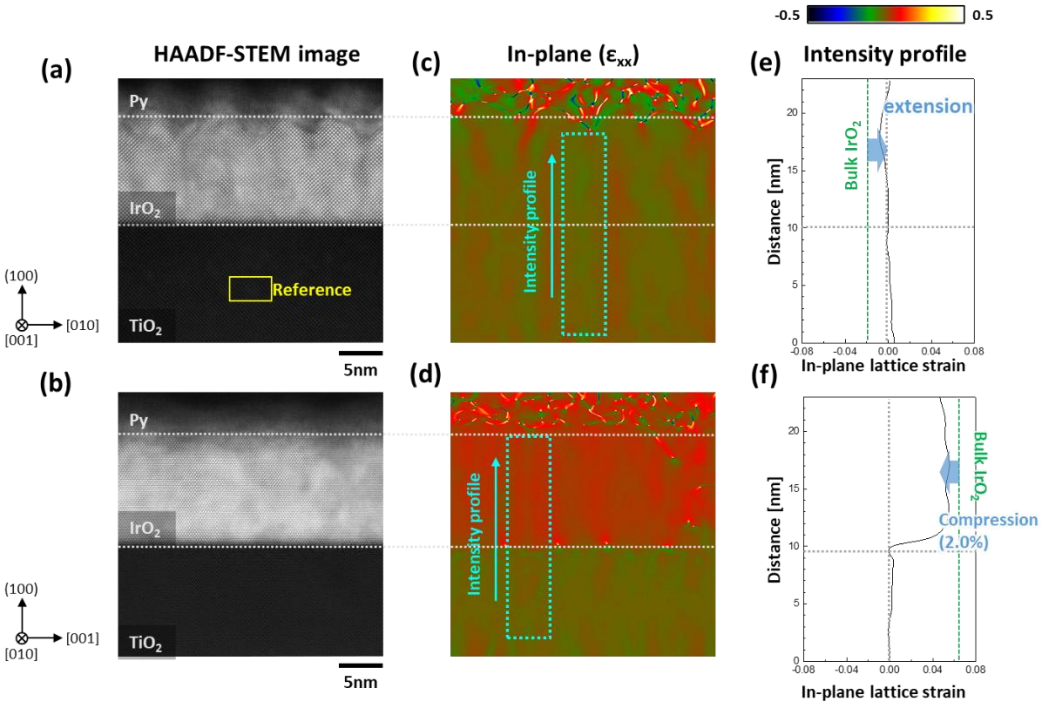

Figure 2.5: Strain analysis in IrO_2 (100) film. a, HAADF-STEM image of IrO_2 (100) films in [110] projection. Scale bar is 5nm. b, Map of in-plane (ε_{xx}) strain analysis of a. c, Intensity profile of In-plane (GPA) image b. The lattice strain is calculated based on the lattice parameter of reference region, which is yellow box in TiO_2 substrate. The interfaces between IrO_2/TiO_2 and Py/IrO_2 are identified by white dashed line.

IrO_2 (110) film is not coherently matched with the TiO_2 substrate as shown in Figure 2.6c and Figure 2.6d because the lattice spacings along [001] and [1-10] are different to ones of TiO_2. However, the IrO_2 film along [001] is not fully relaxed, exhibiting ~ 2.5% compressive strain as shown in Figure 2.6e while the IrO_2 film along [1-10] is mostly relaxed as shown in Figure 2.6f.

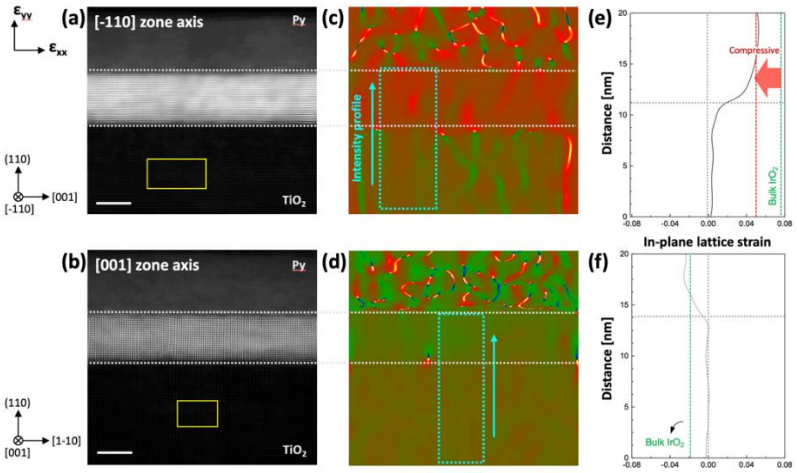

Figure 2.6: Strain analysis in IrO_2 (110) film. a, b HAADF-STEM image of IrO_2 (110) films in [001] and [-110] projection. Scale bar is 5nm. c, d Map of in-plane (ε_{xx}) strain analysis of a and b. e, f Intensity profile of In-plane GPA image c and d. The lattice strain is calculated based on the lattice parameter of reference region, which is yellow box in TiO_2 substrate. The interfaces between IrO_2/TiO_2 and Py/IrO_2 are identified by white dashed line. Tensile strain in [1-10] direction is fully relaxed, but compressive strain is partially relaxed. A compressive strain of about 2.5% is applied in the [001] direction.

IrO_2 (101) film is coherently matched with the TiO_2 substrate as shown in Figure 2.7c and Figure 2.7b. (101) appears to grow similarly with the (111) orientation which is the highest quality of all the orientations.

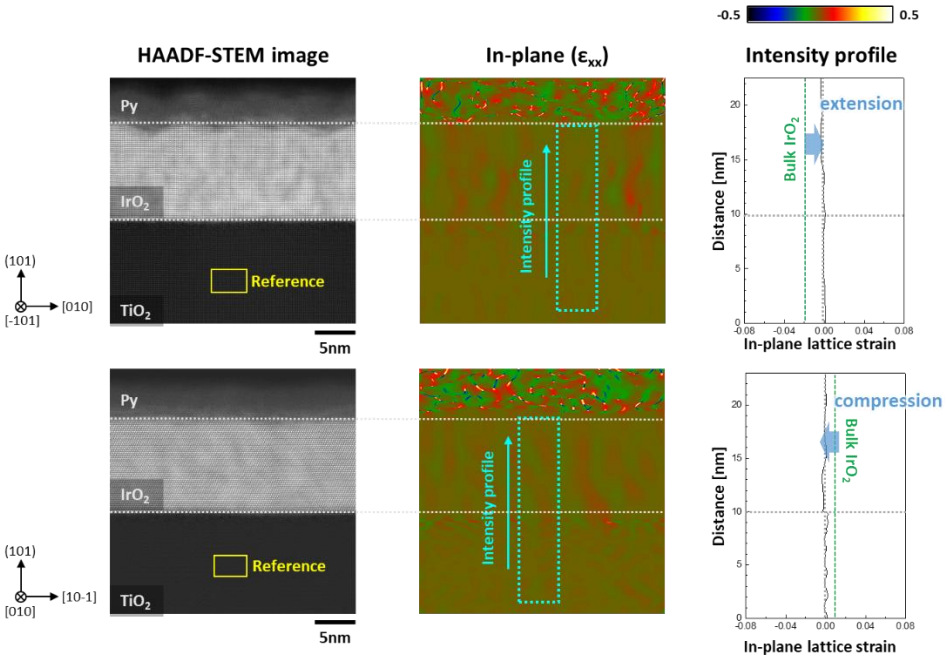

Figure 2.7: Strain analysis in IrO_2 (101) film. a, HAADF-STEM image of IrO_2 (101) films in [110] projection. Scale bar is 5nm. b, Map of in-plane (ε_{xx}) strain analysis of a. c, Intensity profile of In-plane (GPA) image b. The lattice strain is calculated based on the lattice parameter of reference region, which is yellow box in TiO_2 substrate. The interfaces between IrO_2/TiO_2 and Py/IrO_2 are identified by white dashed line.

Finally, for IrO_2 (111) film, the lattice spacing of IrO_2 along [11-2] is coherently matched with TiO_2 substrate as shown in Figure 2.8c and Figure 2.8e and therefore ~2% compressive strain along [11-2] exist in IrO_2 film. On the other hand, the lattice spacing of IrO_2 along [-110] is also mostly matched with that of the substrate, exhibiting ~1.8% tensile strain although this tensile strain is locally relaxed with an introduction of edge dislocations as indicated by the arrows in Figure 2.8b and Figure 2.8d.

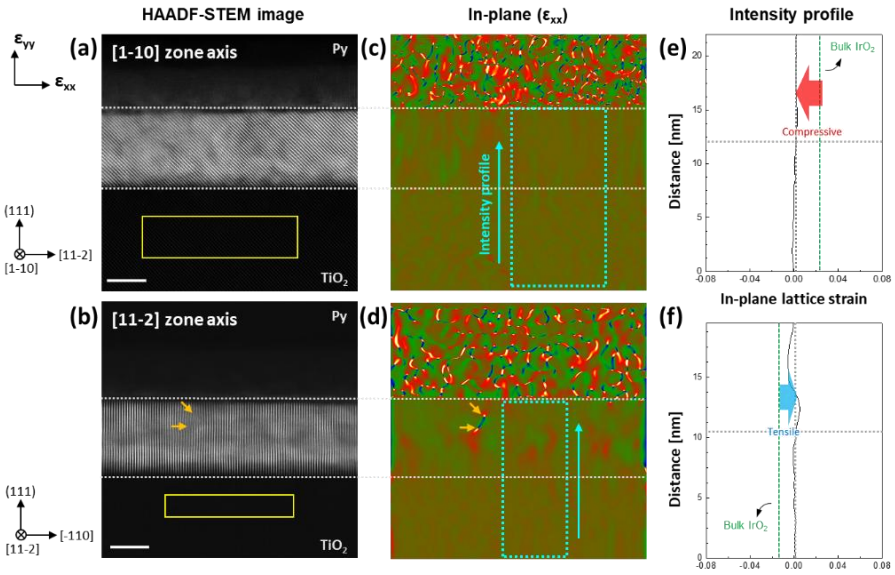

Figure 2.8: Strain analysis in IrO_2 (111) film. a, b HAADF-STEM image of IrO_2 (111) films in [1-10] and [11-2] projection. Scale bar is 5nm. c, d Map of in-plane (ε_{xx}) strain analysis of a and b. e, f Intensity profile of In-plane GPA image c and d. The lattice strain is calculated based on the lattice parameter of reference region, which is yellow box in TiO_2 substrate. The interfaces between IrO_2/TiO_2 and Py/IrO_2 are identified by white dashed line. Tensile strain in [1-10] direction and compressive strain in [11-2] direction are fully applied.

2.4 Triclinic distortions in IrO_2 (111)

The lattice mismatch between IrO_2 and TiO_2 in the (111) plane when grown epitaxially generates compressive strain along the [11-2] direction and tensile strain along the [1-10] direction resulting in a triclinic distortion where $\alpha \,\&\, \beta < 90°$ and $\gamma > 90°$ due to the tetragonality of the rutile unit cell. To fully characterize the structural information for epitaxial IrO_2(111) films, synchrotron measurements were performed on a IrO_2(9nm)/TiO_2(111) sample at beamline 6-ID-B at the Advanced Photon Source at room temperature. Synchrotron x-ray measurements aligned to 9 different Bragg reflections which were used to refine the structure of a 9 nm thick IrO_2 film. The 9 different reflections include (222), (132), (112), (223), (113), (322), (232), (122), and (212). The optimal fit for the 9 reflections results in the measured structure shown in table S1 indicating that the compressive strain along the [-1-12] and tensile strain along the [1-10] direction result in a triclinic distortion of the rutile

structure. We can see the shift of the (223) and (113) peaks seen in Figure 2.10b for the IrO_2 film indicates that $\boldsymbol{\alpha}$ and $\boldsymbol{\beta}$ are no longer 90° and shifting of the (113) further from the substrate peak is a clear marker that the angles are smaller than 90°. When comparing the (222) and (132) reflections, shifts between the IrO_2 film peaks not evident in Figure 2.10a indicating there is no shear-like strain along the [1-10] direction.

Table 2.1: Lattice parameters for bulk TiO_2, bulk IrO_2, and distorted IrO_2 (111) 9nm film.

Lattice Parameter	a (Å)	b (Å)	c (Å)	$\boldsymbol{\alpha}$ (°)	$\boldsymbol{\beta}$ (°)	$\boldsymbol{\gamma}$ (°)
TiO_2 bulk	4.594	4.594	2.959	90	90	90
IrO_2 Bulk	4.498	4.498	3.154	90	90	90
IrO_2 (111) films	4.536	4.536	3.13	89.1	89.1	91.5

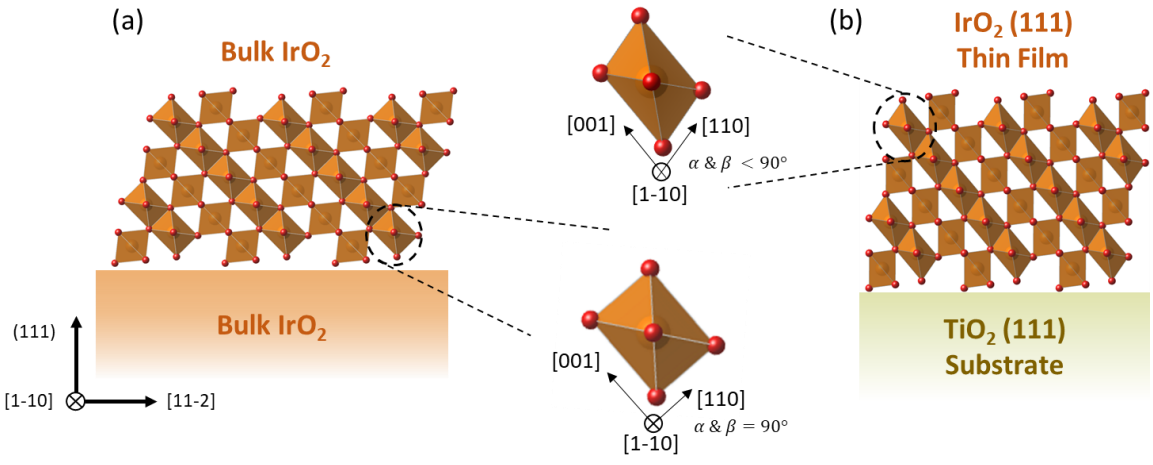

Figure 2.9: Triclinic distortions due to anisotropic epitaxial strain inducing octahedral distortions.

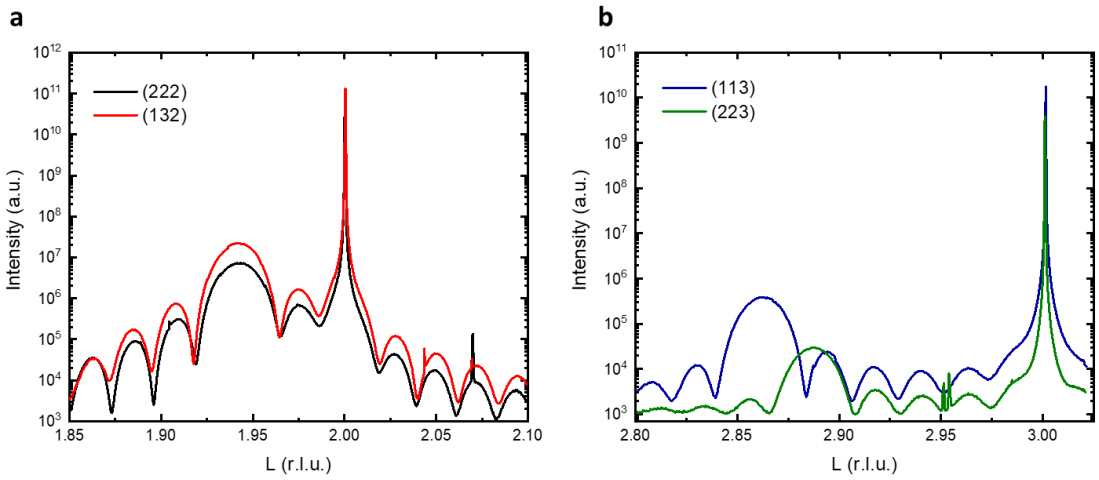

Figure 2.10: Synchrotron x-ray measurements for IrO_2 (111) films. a, synchrotron x-ray data for the (222) (black) and (132) (red) reflections. b, synchrotron x-ray data for the (223) (green) and (113) (blue) reflections where the shift in the IrO_2 (113) (green) away from the TiO_2 (113) relates to the angle change of α and β.

Chapter 3 Design and control of spin-orbit torques in epitaxial IrO_2 thin films

Spin-orbit torques generated by a spin current are key to magnetic switching in spintronic applications. The polarization of the spin current dictates the direction of switching required for energy-efficient devices. Conventionally, the polarizations of these spin currents are restricted to be along a certain direction due to the symmetry of the material allowing only for efficient in-plane magnetic switching. Unconventional spin-orbit torques arising from novel spin current polarizations, however, have the potential to switch other magnetization orientations such as perpendicular magnetic anisotropy which is desired for higher density spintronic-based memory devices. To date, these unconventional spin polarizations have only been observed intrinsically in materials with low crystalline symmetry or magnetic ordering, limiting the potential materials that can be integrated in next generation spintronic devices. Here, we demonstrate that low crystalline symmetry is not required for unconventional spin-orbit torques and can be generated in a non-magnetic high symmetry material, iridium dioxide (IrO_2), using epitaxial design. We show by reducing the relative crystalline symmetry with respect to the growth direction we can generate large unconventional spin currents and hence spin-orbit torques. Furthermore, we compare the spin polarizations detected in (001), (110), and (111) oriented IrO_2 thin films to show which crystal symmetries restrict unconventional spin transport. Understanding and tuning unconventional spin transport generation in high symmetry materials can provide a new route towards energy-efficient magnetic switching in spintronic devices.

3.1 Introduction

Magnetic manipulation via spin-orbit torques (SOTs) generated by spin currents are at the heart of spintronic devices and have been heavily studied in materials hosting charge-to-spin conversion mechanisms such as the spin Hall effect (SHE) [1,2,3]. In heavy metal/ferromagnetic bilayers for spintronic devices, magnetic switching via spin currents requires the spins to be polarized along a certain direction. In high symmetry materials the spin polarization of the spin currents generated via the SHE is restricted to be orthogonal to the spin flow and charge current directions which limits magnetization switching in one direction. Lower symmetry materials, however, can host additional spin currents with polarizations aligned along the charge current direction or aligned along the spin flow direction. These unconventional spin currents have been observed in transition-metal dichalcogenide (TMD)/ferromagnetic bilayers due to the symmetry breaking at the interface[4,5,6,7,8,9], ferromagnetic interfaces due to spin scattering [37,38], and in antiferromagnetic materials due to the low magnetic symmetry [10,11,12,13,14]. Most of the studies to date that show unconventional SOTs occur in systems that have low symmetry throughout the bulk of the material, however, higher symmetry materials still have potential to generate unconventional spin transport. In high symmetry materials, unconventional spin transport is typically forbidden due to crystal symmetries relative to the flow of charge current (J_c), spin current (J_s), and spin polarization (S). Reorienting the crystal structure to lower the symmetry relative to J_c, J_s, and S using epitaxial design, however, could allow for unconventional spin transport in high symmetry materials.

Rutile iridium dioxide (IrO_2), a non-magnetic metallic oxide, has been shown to have a large spin-charge conversion efficiency and high electrical conductivity making this material promising for spintronic applications[25,26,27,28,29]. Only conventional spin-orbit torques have been observed in IrO_2 in previous studies of polycrystalline films and high symmetry orientations such as (001) crystalline films[25,26] due to combinations of symmetry elements that forbid unconventional SOTs. However, lower symmetry orientations can be achieved by utilizing the structural anisotropy due to tetragonality of the rutile crystal structure. IrO_2 in lower symmetry orientations where the crystal symmetry relative to the growth direction is reduced has yet to be studied and could result in unconventional spin transport similar to TMD/ferromagnetic bilayers that support unconventional SOTs[6]. Other studies have compared different crystallographic orientations in IrO_2 and Pt epitaxial films, however, the primary focus of these studies were to show the orientational and strain effects on the conventional SOTs[26,39,40]. Studying the unconventional SHE in different relative symmetry states in a material such as IrO_2 would refine the search for materials with unconventional spin transport and give insight into which symmetries restrict this novel property for next generation spintronic devices.

Here we show unconventional SOT generation in IrO_2 based devices by controlling the relative crystal orientation of IrO_2 using epitaxial design. The SOTs in IrO_2 were studied for (001), (110), and (111) oriented thin films along different in-plane crystallographic directions using spin-torque ferromagnetic resonance (ST-FMR), which agree well with our theoretical calculations. We find unconventional in-plane SOTs for both the (110) and (111) oriented

films as well as out-of-plane unconventional SOTs in the (111) orientation. These results demonstrate how unconventional spin transport can be observed even in higher symmetry materials expanding our understanding of crystal symmetries that allow for unconventional SOTs which could lead to more efficient spintronic devices using any arbitrary magnetization direction.

3.2 Rutile crystal structure and symmetry restrictions of SHC

The spin Hall conductivity (SHC) denoted as σ_{jk}^{i} (where *i* is the spin polarization direction, *j* is the spin flow direction, and *k* is the charge current direction) is a third order tensor calculated from the spin Berry curvature of a material [29,41]. The symmetry of a material restricts which SHC elements can have non-zero values leading to high symmetry materials only hosting conventional SHC where the spin polarization direction, charge current direction, and spin flow direction are all orthogonal. Materials that have lower intrinsic crystalline symmetry such as TMDs can allow for spin polarizations that have not been observed in high symmetry spin source materials. WTe_2, for example, only hosts one mirror plane perpendicular to the surface orientation, leading to unconventional out-of-plane spin currents. No experimental studies thus far have demonstrated unconventional SOTs in materials with higher crystalline symmetry.

IrO_2 (space group $P4_2/mnm$ No. 136) has a tetragonal rutile crystal structure with mirror symmetry (m) along the (001), (110), and (1-10) planes, two-fold rotational symmetries along (C_2) [001],[110] and [1-10], and nonsymmorphic symmetries that include a fourfold rotational screw axis ($\tilde{C}_4$) along [001] and glide mirror planes along the ($\tilde{m}$) (100) and (010) planes. Combinations of these symmetry elements in high symmetry orientations forbid any

unconventional SOTs arising from the bulk of the material. Considering the (001) orientation, for example, both the in-plane unconventional SHCs, i.e. σ_{zx}^{y} or σ_{zy}^{y}, and the out-of-plane unconventional SHCs, , i.e. σ_{zx}^{z} or σ_{zy}^{z}, are not allowed, due to the existence of the (001), (110) and (1-10) mirror planes, and the 4-fold screw axis along [001], as shown in Figure 3.1a. In the (110) orientation, similar to the (001) orientation, no out-of-plane unconventional SHCs would be expected due to the (110) mirror plane. Due to the crystalline anisotropy as a result of the tetragonality of the rutile structure, the in-plane unconventional SHCs are no longer restricted due to the combination of out-of-plane and in-plane mirror symmetries seen in Figure 3.1b. These unconventional in-plane SHCs would, however, vanish when charge current is applied along the high symmetry directions [001] and [1-10] which was seen in a previous study[26]. Symmetry analysis of the SHC indicate a $\sin(2\psi)$ dependance of the in-plane unconventional SOTs as current is applied at an angle ψ away from the (001) mirror plane. Lastly, considering a low symmetry orientation in IrO_2 (111), there is only one in-plane mirror (1-10) plane parallel to the out-of-plane spin currents, as shown in Figure 3.1c. The (1-10) mirror plane restricts any z-polarized out-of-plane spin current with charge current applied parallel to the mirror plane, however, current applied perpendicular should allow for out-of-plane unconventional SHCs. Likewise, in-plane unconventional SHCs are restricted with current applied parallel and perpendicular to the (1-10) mirror plane, however, these in-plane SHCs should be non-zero when charge current is applied at some in-plane angle between 0 and 90 degrees with respect to the mirror plane. With these unconventional SHCs, the low symmetric oriented IrO_2 film can be used as a promising spin source to exert unconventional SOTs on the adjacent ferromagnetic layer.

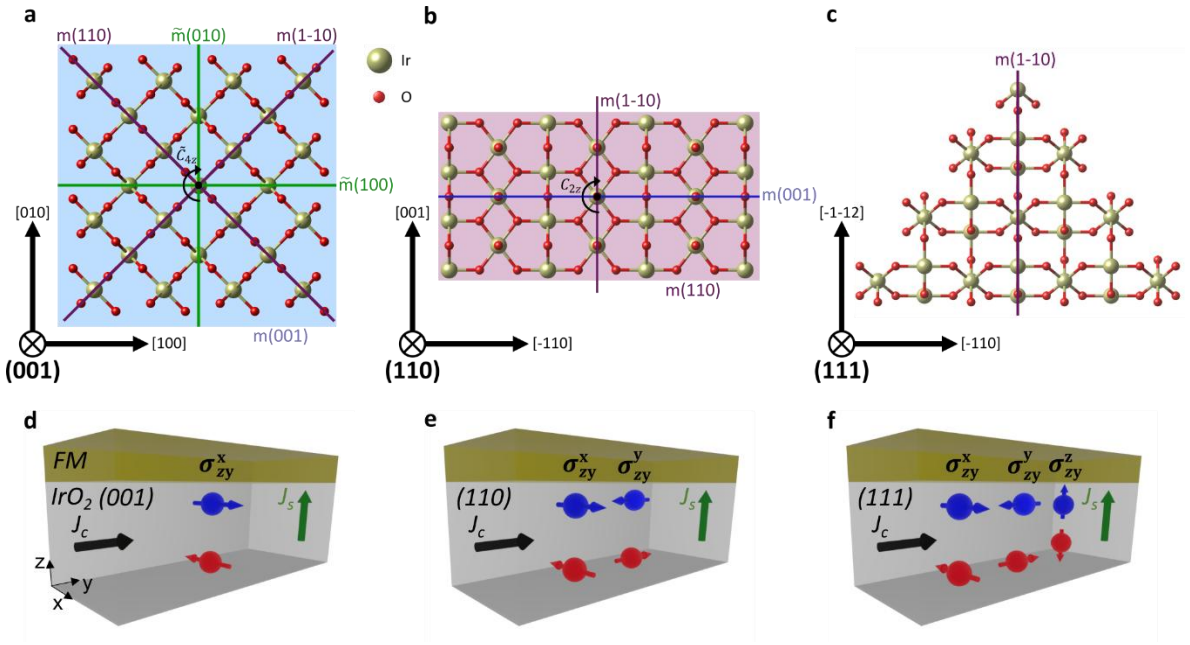

Figure 3.1: Epitaxial design for unconventional SOTs in IrO_2. a, b, c The IrO_2 (001), (110), and (111) projections of the rutile crystal structure with crystal symmetries. d, e, f, The allowed spin Hall conductivity tensors for the (001), (110), and (111) orientations for a resulting spin current (J_s) in the z-directions generated from a charge current (J_c) applied in the y direction.

3.3 IrO_2 growth and characterization

Epitaxial IrO_2 thin films were grown on single-crystal TiO_2 (001), (110), and (111) oriented substrates via RF magnetron sputtering with a ferromagnetic Permalloy (Py) overlayer used as the spin detector for the spintronic measurements. The IrO_2 films were grown at 400°C at a pressure of 30 mTorr with 10% oxygen partial pressure. The target power was 20 W. After growth the sample was cooled in an O_2 atmosphere. Py was then grown in situ at room temperature, 4 mTorr of Ar, power of 35W, and a background pressure of 3E-7 Torr. The samples were then fabricated using photolithography and ion beam milling, followed by sputter deposition of 100 nm Pt/10nm Ti and lift off techniques for the electrodes. Fully epitaxial IrO_2 samples were achieved for each orientation and confirmed with high resolution x-ray diffraction (HRXRD) seen in Figure 3.2a-c for each orientation.

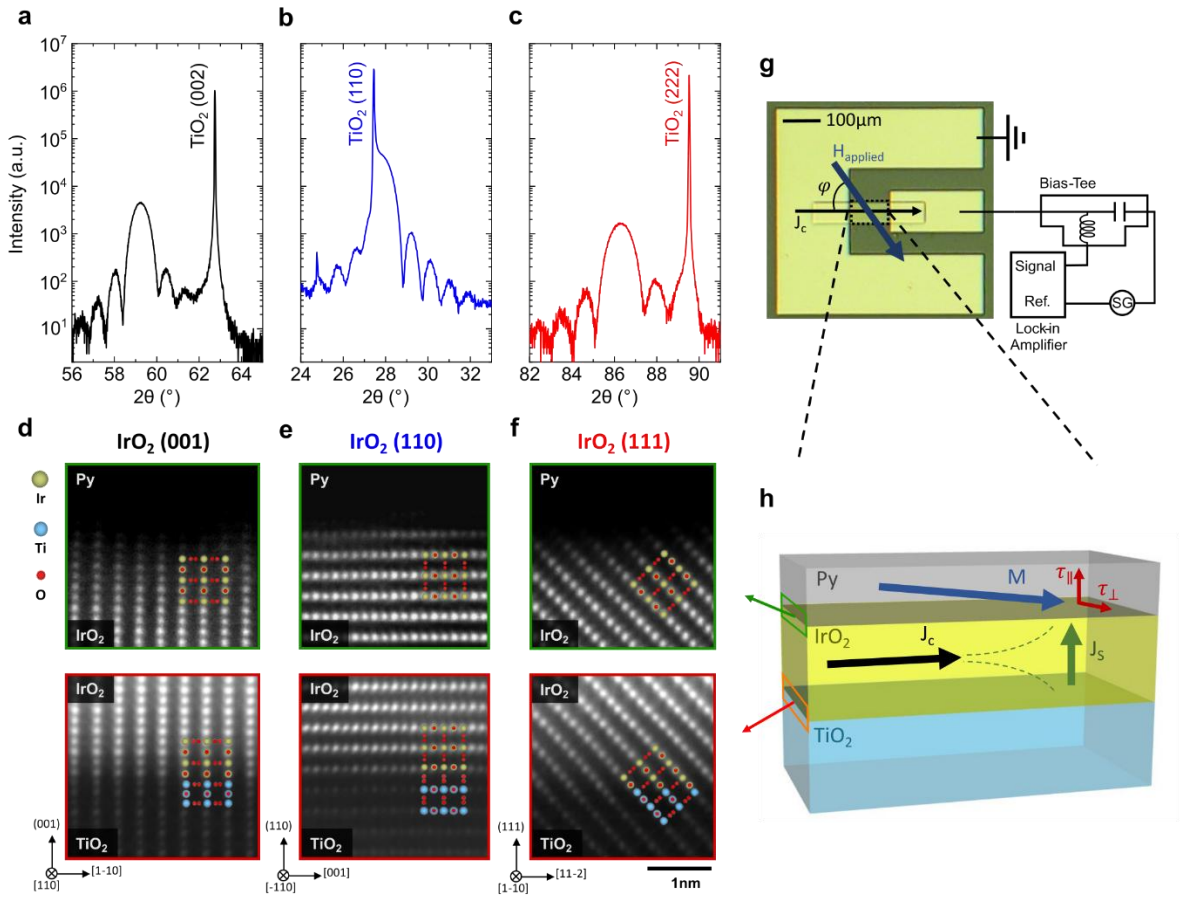

Figure 3.2: Film characterization and ST-FMR device schematic. a-c, Out-of-plane XRD showing epitaxial growth of IrO_2 on TiO_2 for the (001), (110), and (111) orientations. d-f, High-angle annular dark-field (HAADF)-STEM images of Py/IrO_2 and IrO_2/TiO_2 interfaces for the (001), (110), and (111) orientations with simulated unit cell. g, Schematic showing device and measurement geometry for ST-FMR measurements and h, schematic showing external applied field and resulting field-like and damping like torques in the ST-FMR measurements.

3.4 ST-FMR lineshape analysis and magnetic properties of Py

To determine the SHC for (001), (110), and (111) oriented IrO_2, samples were patterned into 50 μm x 100 μm microstrips with a ground-source-ground electrode pattern for spin-torque ferromagnetic resonance (ST-FMR) measurements seen in Figure 3.2g. Angular ST-FMR measurements[42] were performed to determine the SHC for IrO_2 films where a magnetic field is swept in-plane at different angles with respect to the microstrip while applying a microwave current I_{rf}. During the ST-FMR measurements, a microwave current was applied

at a fixed frequency (5-12GHz) and fixed power (10-13 dBm) while sweeping an in-plane magnetic field through the Py resonance conditions from 0 to 0.15 T. The microwave current was modulated at a fixed frequency of 437 Hz and the mixing voltage across the device was measured using a lock-in amplifier. The mixing voltage was fitted vs applied field to extract the symmetric and antisymmetric Lorentzian components. For the angular-dependent ST-FMR, the applied field was rotated in-plane 360° and the symmetric and antisymmetric components were plotted as a function of angle. Conventionally, torques generated from Oersted fields acting on the magnetization are in the form of $\boldsymbol{m} \times \boldsymbol{y}$ where $\boldsymbol{y}$ is an in-plane direction perpendicular to the charge current direction $\boldsymbol{x}$ (Figure 3.2h), resulting in a field-like torque ($\tau_{\perp}$). In addition to the out-of-plane torques, spin currents resulting from the SHE (or other spin generating effects) can also generate torques in the form of $\boldsymbol{m} \times (\boldsymbol{m} \times \boldsymbol{y})$ resulting in a damping-like torque ($\tau_{\parallel}$)[43]. The out-of-plane ($\tau_{\perp}$) and the in-plane ($\tau_{\parallel}$) torques are proportional to the mixing voltage V_{mix} as the ferromagnetic layer goes through its resonance condition which can be fitted as a sum of a symmetric and an antisymmetric Lorentzian:

$$V_{mix,S} = -\frac{I_{rf}}{2}\left(\frac{dR}{d\varphi}\right)\frac{1}{\alpha(2\mu_0 H_{FMR}+\mu_0 M_{eff})}\tau_{\parallel} \quad (1)$$

$$V_{mix,A} = -\frac{I_{rf}}{2}\left(\frac{dR}{d\varphi}\right)\frac{\sqrt{1+M_{eff}/H_{FMR}}}{\alpha(2\mu_0 H_{FMR}+\mu_0 M_{eff})}\tau_{\perp} \quad (2)$$

Where R is the resistance of the device, φ is the magnetization angle with respect to the applied current, α is the Gilbert damping coefficient, $\mu_0 H_{FMR}$ is the resonance field, and $\mu_0 M_{eff}$ is the effective magnetization. The lineshape for IrO_2 (111) can be seen in Figure S6a. The effective magnetization of Py can be obtained using Kittel's equation $f =$

$\frac{\gamma}{2\pi}\sqrt{(H_{FMR}+H_K)(H_{FMR}+H_K+M_{eff})}$ where γ is the gyromagnetic ratio and H_K is the in-plane anisotropy field. By measuring H_{FMR} vs rf frequency with current applied along the [100] direction for (001), [1-10] for the (110), and [1-10] for the (111) and an applied field 45° from the current direction, we found the effective magnetization for (001) to be 0.51 T, (110) to be 0.85 T, and (111) to be 0.85 T extracted from the fittings seen in Figure S6d. The Gilbert damping coefficient α is obtained by fitting the linear relationship seen in Figure S6e between the linewidth (w) and the frequency $w = w_0 + \left(\frac{2\pi}{\gamma}\right) * f$. To calibrate the microwave current (I_{rf}) we compare the resistance change due to Joule heating across the Hall bar device while varying the microwave power. We can then find $I_{rf} = \sqrt{2}I_{dc}$ due to the joule heating relationship between ac and dc current seen in Figure 3.

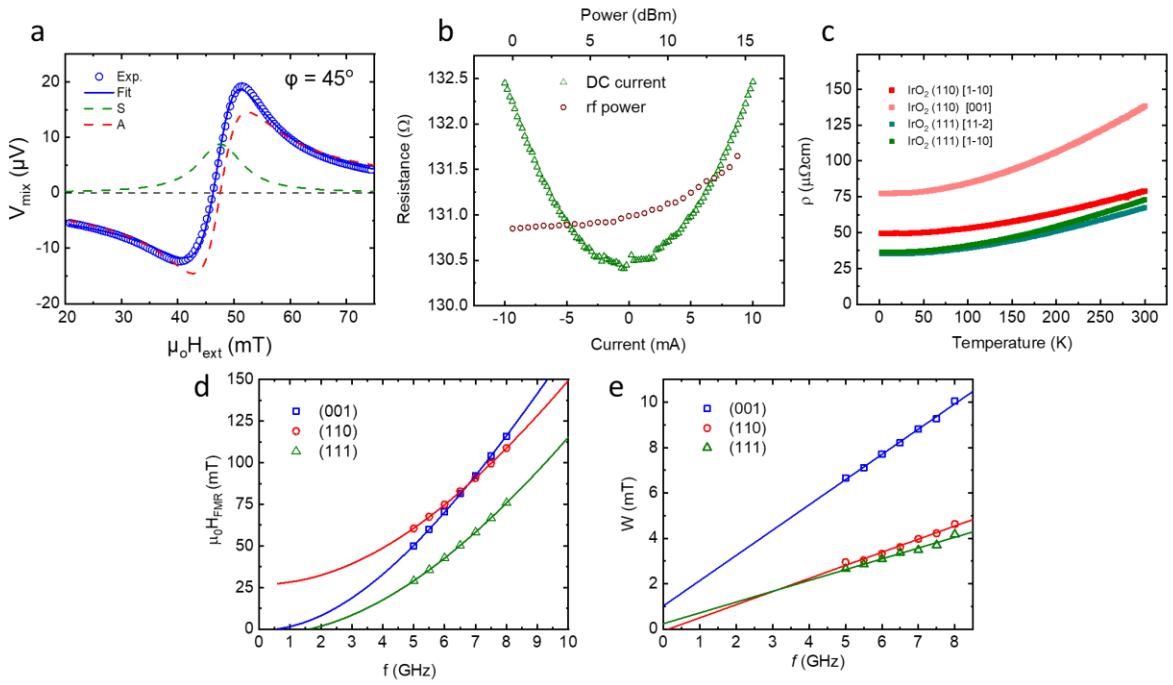

Figure 3.3: Lineshape analysis, RF calibration, and transport properties. a, ST-FMR spectrum at 7GHz 10dBm for a IrO_2 (111) sample showing the symmetric (green) and antisymmetric (red) contributions when an external magnetic field is applied 45° rotated in-plane from the applied current. b, resistance change as a function of applied DC current (green) and rf power (red). c, in-plane resistivity as a function of temperature for (110) and (111) oriented IrO_2 along the principle axes. d, resonance field (H_{FMR}) as a function of the applied rf current frequency with current applied along the [100] direction for (001), [1-10] for the (110), and [1-10] for the (111) and an applied field 45° from the current direction fitted with Kittel's formula. e, linewidth as a function of the applied rf current frequency for each orientation fitted with a linear fit.

To quantitatively determine all torque contributions, ST-FMR measurements were performed as a function of applied in-plane magnetic field angle (φ). In conventional heavy-metal/ferromagnetic bilayers the AMR of Py ($\frac{dR}{d\varphi}$) has an angular dependance proportional to sin(2φ) and the out-of-plane ($\tau_\perp$) and the in-plane ($\tau_\parallel$) torques are proportional to cos(φ) resulting in the $V_{mix,S}$ and $V_{mix,A}$ being in the form of sin (2 φ)cos(φ). Additional unconventional torques that have different spin polarization directions, however, can contribute to the angular dependance resulting in a more general form of the angular dependance:

$$\tau_{\parallel} = \tau_{x,AD}\sin(\varphi) + \tau_{y,AD}\cos(\varphi) + \tau_{z,FL} \quad (3)$$

$$\tau_{\perp} = \tau_{x,FL}\sin(\varphi) + \tau_{y,FL}\cos(\varphi) + \tau_{z,AD} \quad (4)$$

$V_{mix,S}$ and $V_{mix,A}$ can then be expressed in the form of $\sin(2\varphi)(\tau_{x,AD}\sin(\varphi) + \tau_{y,AD}\cos(\varphi) + \tau_{z,FL})$ and $\sin(2\varphi)(\tau_{x,FL}\sin(\varphi) + \tau_{y,FL}\cos(\varphi) + \tau_{z,AD})$, respectively.

Figure 4 shows the angular dependance of $V_{mix,S}$ and $V_{mix,A}$ for IrO_2 (001), (110), and (111) films for fixed directions of applied current as illustrated in the insets. We find that the angular dependance of both $V_{mix,S}$ and $V_{mix,A}$ for the (001) orientation fits well only with conventional contributions to the torques whereas the (110) and (111) orientations require additional torque components to fit well with the raw data. We find contributions from in-plane conventional spin torques (perpendicular to the charge current direction) and in-plane unconventional spin polarized torques (aligned along the charge current direction) for both the (110) and (111) oriented films. The (111) orientation also shows a contribution from out-of-plane spin polarized torques. The conventional SHC has a value of σ_{zx}^{y} = 116 ± 1 ($10^3\hbar/2e(\Omega m)^{-1}$) for the (111) oriented films, 180 ± 4 ($10^3\hbar/2e(\Omega m)^{-1}$) for the (001) oriented films, and 114 ± 8 ($10^3\hbar/2e(\Omega m)^{-1}$) for the (110) oriented films. The unconventional SOTs for (110) and (111) were fully characterized as a function of the in-plane angular dependance.

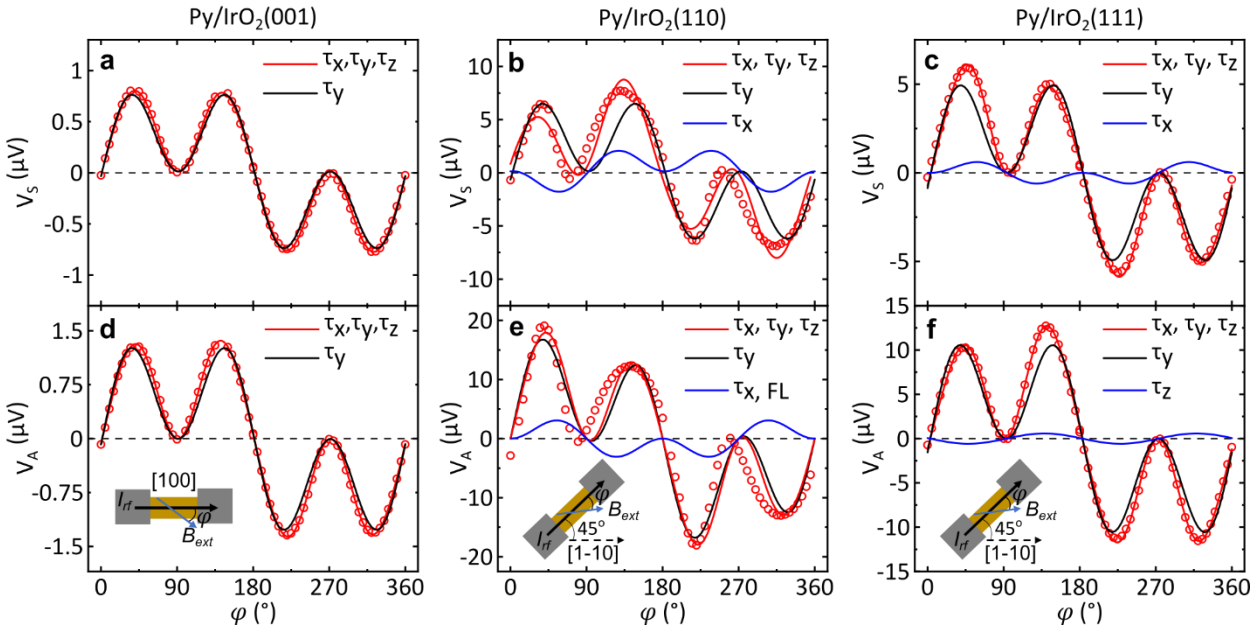

Figure 3.4: Angular ST-FMR results for (001), (110), and (111) IrO_2. a, Symmetric component of the mixing voltage V_s from angular ST-FMR measurements for IrO_2 (001) with the in-set showing the current I_{rf} direction along the [100] direction while the applied external field B_{ext} is rotated with respect to I_{rf} by some angle φ. Fittings are shown for only τ_y and for combined τ_x, τ_y, τ_z. b, V_s for IrO_2 (110) as I_{rf} is applied 45° rotated in-plane from the [1-10] direction. Showing contributions from conventional τ_y and unconventional in-plane τ_x. c, V_s for IrO_2 (111) as I_{rf} is applied 45° rotated in-plane from the [1-10] direction. Showing contributions from conventional τ_y and unconventional in-plane τ_x. d, Antisymmetric component V_A for IrO_2 (001) showing contributions from conventional τ_y. e, V_A for IrO_2 (110) showing contributions from conventional τ_y and a field-like $\tau_{x,FL}$. f, V_A for IrO_2 (111) showing contributions from conventional τ_y and unconventional out-of-plane τ_z.

The usual field-like and damping-like torques produced by high-symmetry materials and acting on magnets with negligible in-plane anisotropy have a dependence on the angle of applied magnetic field φ proportional to $\cos(\varphi)$. In addition to this term, we also detect $\cos(3\varphi)$ higher-harmonic angular dependencies in our angular ST-FMR measurements. Compared to the expressions in Eq. 3 and 4, we can improve our fits by also including this higher-harmonic term, yielding the fitting equations:

$$\sin(2\varphi)(\tau_{x,AD}\sin(\varphi) + \tau_{y,AD}\cos(\varphi) + \tau_{z,FL} + S_3\cos(3\varphi)) \quad (5)$$

$$\sin(2\varphi)(\tau_{x,FL}\sin(\varphi) + \tau_{y,FL}\cos(\varphi) + \tau_{z,AD} + A_3\cos(3\varphi)) \quad (6)$$

where S_3 and A_3 are the higher harmonic coefficients. We compare the fits with and without the $\cos(3\varphi)$ terms in Figure 3.5c and 3.5d for both (111) and (110) orientations. The origin of this higher harmonic is likely due to magnetic anisotropy in our bilayers, arising because in the presence of anisotropy the true magnetization angle φ_M can differ slightly from the applied field angle φ (see the discussion below in the paragraph following Eq. (10)). A similar effect has also been seen in WTe_2/permalloy samples in which interaction with the WTe_2 induces significant within-plane uniaxial magnetic anisotropy[6].

We also find additional harmonic contributions to the anisotropic magnetoresistance (AMR) of the (110) orientation due to significant in-plane uniaxial anisotropy. The AMR was determined by measuring the device resistance as a function of in-plane magnetic field angle seen in Figure 3.5a for a (111) oriented film and Figure 3.5b for a (110) with applied magnetic field of 0.2T. AMR for magnetic materials with uniaxial anisotropy measurement should be described using the following equation:

$$R_o + \Delta\mathrm{R}\cos(\varphi_M)^2 \tag{7}$$

where R_o is the resistance with zero applied field and $\Delta\mathrm{R}$ is the difference in resistance when field is applied along the current direction and perpendicular to the current direction. Depending on how large the uniaxial anisotropy is, the magnetization can deviate from the applied magnetic field direction as:

$$\varphi_M = \varphi + \mathrm{K}\sin(2\varphi_M - 2\varphi_{ani}) \;\approx\; \varphi + \mathrm{K}\sin(2\varphi - 2\varphi_{ani}) \tag{8}$$

where the coefficient K scales with the uniaxial anisotropy energy, and φ_{ani} is the angle between the current direction and anisotropy axis. Including this term in the AMR Equation

7 as $R_o + \Delta\mathrm{R}\cos\left(\varphi + \mathrm{K}\sin(2\varphi - 2\varphi_{ani})\right)^2$ and after a Taylor expansion, we can model our AMR signal using:

$$R_o + \Delta\mathrm{R}\cos(\varphi)^2 - K\sin(2\varphi)\sin(2\varphi - 2\varphi_{ani}) \quad (9)$$

We find only small contributions from the $K\sin(2\varphi)\sin(2\varphi - 2\varphi_{ani})$ term in our (111) oriented samples and the AMR signal can fit well simply to $R_o + \Delta\mathrm{R}\cos(\varphi)^2$ as seen in Figure 3.5a. This was expected as we found a very small in-plane anisotropy field H_K of 0.4mT extracted from Kittel's formula. For the (110) on the other hand, we find a much larger in-plane anisotropy field H_K of 2.7mT, which leads to a larger $K\sin(2\varphi)\sin(2\varphi - 2\varphi_{ani})$ contribution in the AMR signal as seen in Figure 3.5b. We find φ_{ani} to be closely aligned with the [001] in-plane axis on our (110) films.

We then obtain $\frac{dR}{d\varphi_M}$, which is needed for analyzing the angular ST-FMR seen in Equation 5 and 6, by differentiating Eq. (7) and then Taylor expanding to account for the difference between φ_M and φ. This leads to $\frac{dR}{d\varphi_M} \propto (\sin(2\varphi) + a\sin(4\varphi - 2\varphi_{ani}))$ where the coefficient *a* is a constant. Finally, we arrive at the following equation to analyze the angular ST-FMR:

$$(\sin(2\varphi) + a\sin(4\varphi - 2\varphi_{ani}))(\tau_{x,FL}\sin(\varphi) + \tau_{y,FL}\cos(\varphi) + \tau_{z,AD} + A_3\cos(3\varphi)) \quad (10)$$

The coefficient *a* is fixed by the AMR measurement, so the adjustable parameters used to fit the angular dependence of the antisymmetric ST-FMR amplitude are $\tau_{x,FL}$, $\tau_{y,FL}$, $\tau_{z,AD}$, and A_3. We find negligible contributions from the additional $\sin(4\varphi - 2\varphi_{ani})$ term for the (111) orientation, however, we find that the fitting for the (110) greatly improves when this term is

added as seen in Figure 3.5d. By the same reasoning as for the additional AMR contributions mentioned above, the dominant torque in the angular ST-FMR signal has an angular dependence of $\cos(\varphi_M) = \cos(\varphi + \mathrm{K}\sin(2\varphi - 2\varphi_{ani}))$ and after a Taylor expansion and if φ_{ani} is 0, we get $\cos(\varphi) - 2\mathrm{K}(1 - \cos(\varphi)^2)\cos(\varphi)$ which leads to $\cos(\varphi) + A_3\cos(3\varphi)$. This can explain the higher harmonic $A_3\cos(3\varphi)$ contribution mentioned previously.

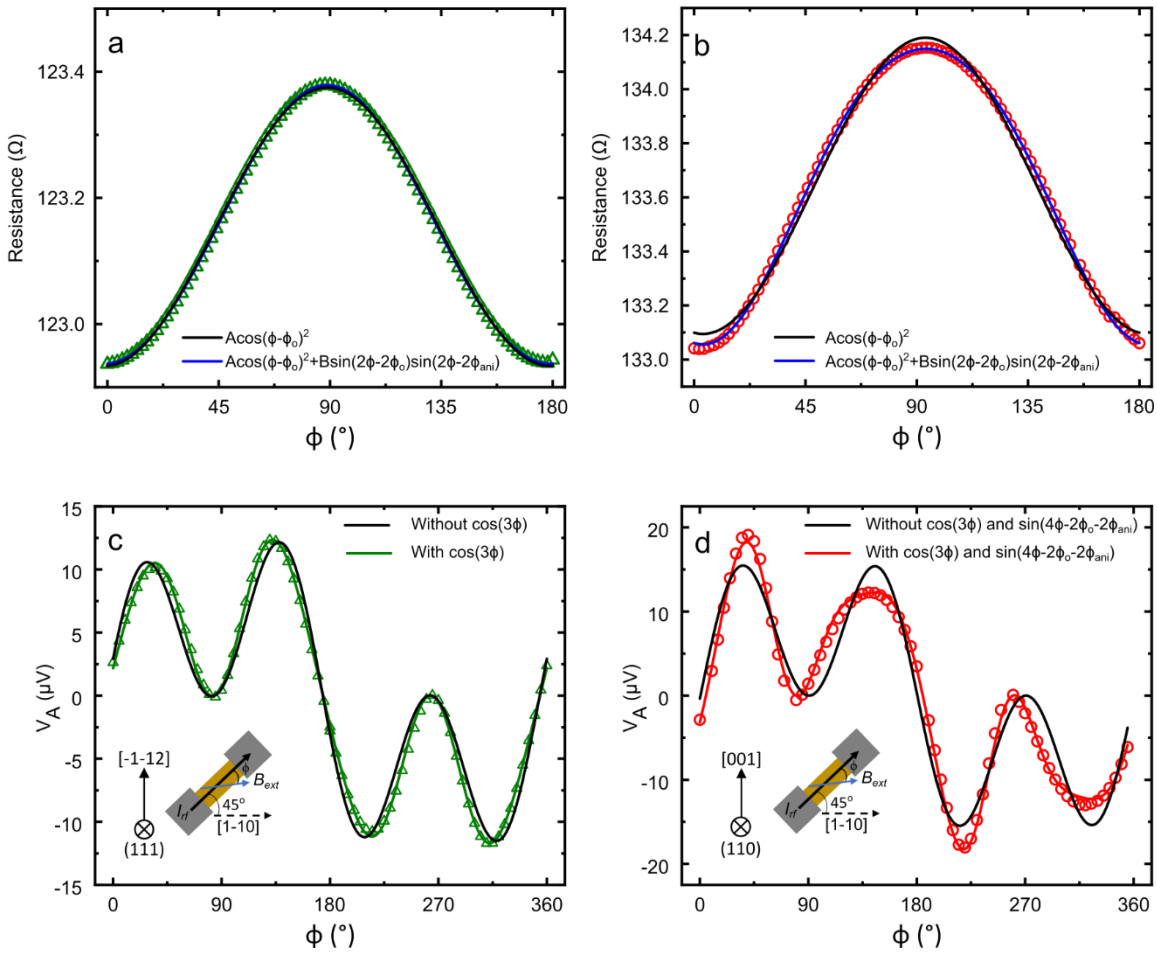

Figure 3.5: Angular ST-FMR fittings with and without higher harmonic AMR contributions for (111) and (110) orientations. a,b, AMR measurement where the resistance was measured as a function of in-plane magnetic field of 0.2T for (111) and (110) oriented films, respectively. c, antisymmetric component of the angular ST-FMR for (111) oriented IrO_2 and d, (110) oriented IrO_2 where the raw data is fitted with and without the higher harmonic terms. Both spectra are for current applied in-plane 45° from the [1-10] in plane direction depicted by the inset.

3.5 ST-FMR crystallographic dependance

The unconventional SHCs obtained in (111) and (110) oriented IrO_2 are dependent on the in-plane current direction with respect to the crystallographic axes due to symmetry operations. Theoretical calculations predict σ_{zx}^{x} to be proportional to sin(2ψ) for both (111) and (110) and σ_{zx}^{z} to be proportional to cos(ψ) for (111) where ψ is the angle between the applied current and the in-plane [-110] crystallographic axis shown in Figure 3.6a and 3.6b. The in-plane angular dependance of J_c for σ_{zx}^{x} for both the (110) and the (111) orientations can be seen in Figure 3.6c and 3.6d. Both orientations show a clear sin(2ψ) dependance agreeing well with theoretical calculations both qualitatively and quantitatively. We find the maximum σ_{zx}^{x} at 45° to be 130 ± 29 ($\hbar$/e(Ωcm)$^{-1}$) for the (110) orientation and 51 ± 5 ($\hbar$/e(Ωcm)$^{-1}$) for the (111) orientation. Additionally, Figure 3.6e and 3.6f show the angular dependance of σ_{zx}^{z} which shows no out-of-plane unconventional SHC within experimental error for the (110) orientation and a cos(ψ) dependance for the (111) orientation with a maximum σ_{zx}^{z} when current is applied perpendicular to the (1-10) mirror plane with a value of 9 ± 1 ($\hbar$/e(Ωcm)$^{-1}$, agreeing qualitatively with the theoretical calculations.

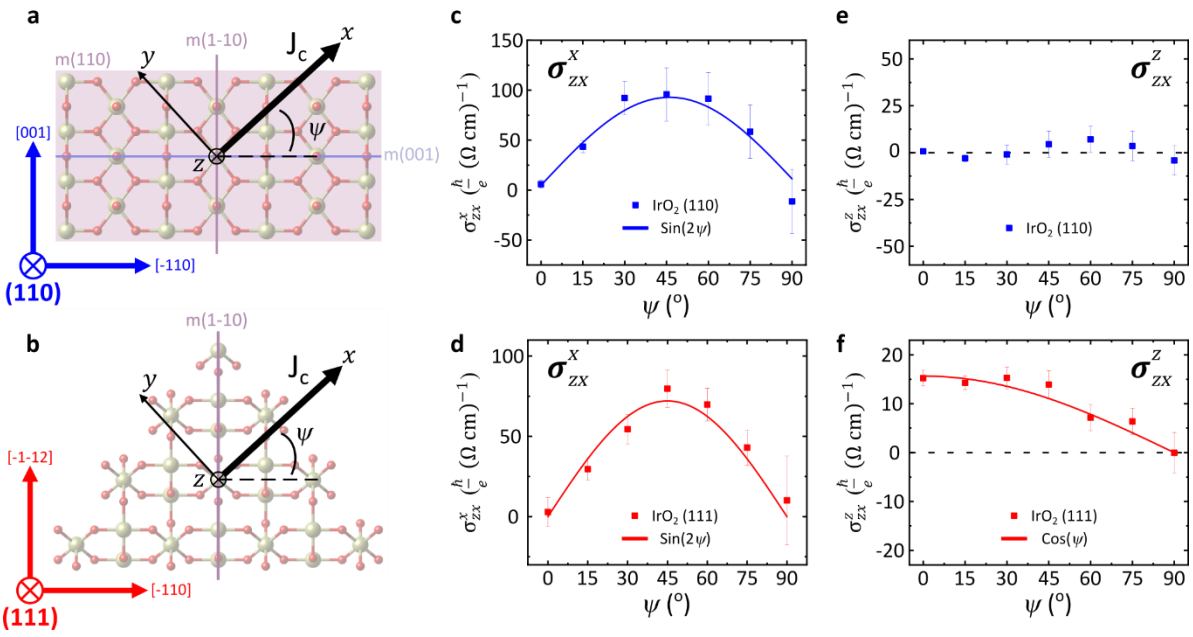

Figure 3.6: In-plane crystallographic dependance on unconventional SHCs a,b IrO_2 (110) and (111) projections where $\psi = 0^o$ when charge current J_c is applied along the [-110] direction for both orientations. c,d,e,f In-plane and out-of-plane unconventional SHCs for the (110) and (111) orientation where each data point (red square) are determined from the angular ST-FMR done at 7GHz and 10dBm on a device angled ψ away from the [-110] crystallographic axis compared with the theoretical calculations (black dashed line).

The experimental results of the unconventional SHCs in our IrO_2 (110) and (111) films qualitatively agree with theoretical predictions using DFT calculations. The unconventional in-plane SHC σ_{zx}^{x} clearly follows a sin(2ψ) in-plane angular dependance experimentally for both the (110) and (111) orientations which is expected due to the lack of out-of-plane 4-fold rotational symmetry. The unconventional out-of-plane SHC σ_{zx}^{z} clearly follows a cos(ψ) in-plane angular dependance for the (111) orientation and is zero within experimental error for the (110) due to the out-of-plane (110) mirror plane. Quantitative differences between theory and experimental are quite common across many material systems such as Pt and IrO_2[44,45,12] even for conventional SHCs suggesting that there may be something missing in the DFT calculations. Interestingly, we do find our unconventional in-plane SHC σ_{zx}^{x} to match very well with DFT calculations for both (110) and (111) orientations. In addition to the data

shown, IrO_2 (111) films undergo lattice distortions induced by the anisotropic epitaxial strain which were characterized using synchrotron x-ray measurements. Using these distortions in our DFT calculations show σ_{zx}^{x} to be two times larger than what is predicted for bulk IrO_2 (111), agreeing very well with our data shown. These results demonstrate that we can generate and control unconventional SOTs using epitaxial design which can be used as a guide for other material systems that have not been studied in lower symmetry orientations.

3.6 Conclusion

In summary, we have shown unconventional spin-orbit torques in a high symmetry spin source material, IrO_2, using symmetry design in epitaxial heterostructures. Unconventional torques are not present in high symmetry orientations such as (001) due to vanishing unconventional SHC in the presence of multiple rotational and mirror symmetries of IrO_2 relative to the film growth direction. In the (110) and (111) orientations, we experimentally observe in-plane unconventional SOTs. Additionally, the (111) orientation shows unconventional out-of-plane SOTs. This is due to the fact that these low symmetry oriented films are only invariant to a small number of symmetry constraints that allows the unconventional SHCs. The unconventional out-of-plane SHC σ_{zx}^{z} observed in our IrO_2 (111) films are on the same order of magnitude as other low symmetry materials such as non-collinear antiferromagnetic Mn_3GaN and Mn_3Pt, collinear antiferromagnetic RuO_2, and 2D TMD WTe_2[6,11,13,14], indicating this route to be promising towards finding spintronic materials for PMA switching. This work could provide a route to designing and discovering unconventional spin-torques in other high symmetry materials by using low symmetry orientations. Using this approach, all one needs is a DFT calculation in one orientation for a

given material and, using rotation matrices, one can predict unconventional SOTs for lower symmetry orientations.

Supplemental Note: Theoretical Calculations

DFT calculations were performed using a Quantum-ESPRESSO code[20]. The plane-wave pseudopotential method with the fully relativistic ultrasoft pseudopotentials[21] was employed in the calculations. The exchange and correlation effects were treated within the generalized gradient approximation (GGA)[22]. The plane-wave cut-off energy of 40 Ry and a 16 × 16 × 16 k-point mesh in the irreducible Brillouin zone were used in the calculations. Spin-orbit coupling was included in all the calculations.

The spin Hall effect is given by:

$$\sigma_{ij}^{k} = \frac{e^2}{\hbar}\int \frac{d^3\vec{k}}{(2\pi)^3}\sum_{n} f_{n\vec{k}}\Omega_{n,ij}^{k}(\vec{k}), \tag{5}$$

$$\Omega_{n,ij}^{k}(\vec{k}) = -2Im\sum_{n\neq n'}\frac{\langle n\vec{k}|J_i^k|n'\vec{k}\rangle\langle n'\vec{k}|v_j|n\vec{k}\rangle}{\left(E_{n\vec{k}} - E_{n'\vec{k}}\right)^2}\quad , \tag{6}$$

where $f_{n\vec{k}}$ is the Fermi-Dirac distribution for the *n*th band, $J_i^k = \frac{1}{2}\{v_i, s_k\}$ is the spin current operator with spin operator s_k, $v_j = \frac{1}{\hbar}\frac{\partial H}{\partial k_j}$ is the velocity operator, and $i, j, k = x, y, z$. $\Omega_{n,ij}^{k}(\vec{k})$ is referred to as the spin Berry curvature in analogy to the ordinary Berry curvature. In order to calculate the spin Hall conductivities, we construct the tight-binding Hamiltonians using PAOFLOW code[23,24] based on the projection of the pseudo-atomic orbitals (PAO) from the non-self-consistent calculations with a 16 × 16 × 16 *k*-point mesh. The spin Hall conductivities were calculated using the tight-binding Hamiltonians with a 48 × 48 × 48 *k*-

point mesh by the adaptive broadening method to get the converged values. The elements of the spin Hall conductivity tensors for different plane $[111]$, $[110]$ etc. can be transformed from the spin Hall conductivity tensors of [001] plane as

$$\sigma^{s}_{ij,[plane]} = \sum_{l,m,n} R_{il} R_{jm} R_{kn} \, \sigma^{s}_{lm,[001]}, \tag{7}$$

Where *i* is the spin current direction j is the charge current direction, *s* is the spin polarization direction, and R_{il} is an element of the rotation matrix R which transforms from [001] to the desired orientation.

Chapter 4 Complete experimental determination of spin Hall conductivity in epitaxial IrO_2 thin films

4.1 Introduction

Unconventional spin-orbit torques arising from electric-field-generated spin currents in anisotropic materials have promising potential for spintronic applications, including for perpendicular magnetic switching in high-density memory applications. Here we determine all the independent elements of the spin torque conductivity tensor allowed by bulk crystal symmetries for the tetragonal conductor IrO_2, via measurements of conventional (in plane) anti-damping torques for IrO_2 thin films in the high-symmetry (001) and (100) orientations. We then test that rotational transformations of this same tensor can predict both the conventional and unconventional anti-damping torques for IrO_2 thin films in the lower-symmetry (101), (110), and (111) orientations, finding good agreement. The results confirm that spin-orbit torques from all these orientations are consistent with the bulk symmetries of IrO_2, and show how simple measurements of conventional torques from high-symmetry orientations of anisotropic thin films can provide an accurate prediction of the unconventional torques from lower-symmetry orientations.

The linear-response spin current generated by an applied electric field within a material is described by a third-rank spin Hall conductivity (SHC) tensor σ_{ij}^{s}, where *s* is the index for the spin polarization direction, *i* for the spin flow direction, and *j* for the applied electric field direction. If the spin current is absorbed by an adjacent magnetic layer, it will apply a torque that can efficiently reorient the magnetization. The 27 elements within σ_{ij}^{s} are often highly constrained by symmetry, and in commonly-used high-symmetry materials most of the

elements are zero because symmetries can require the spin polarization, spin flow, and electric field to be mutually orthogonal. We will term the torques generated by such a spin current as "conventional". For some applications, however, unconventional spin torques are highly desired. In particular, out-of-plane anti-damping torques associated with tensor elements of the form σ_{zj}^{z} (where *z* is the direction normal to the device plane) are needed to drive efficient anti-damping switching of magnetic memory devices with perpendicular magnetic anisotropy. Such out-of-plane anti-damping torques have been realized using spin-source materials in which the symmetry constraints are relaxed by very low crystal symmetries or magnetic ordering[46–57] or by interfacial effects[58–60]. We have also recently proposed a simple alternative strategy for generating out-of-plane anti-damping torques -- to use a relatively high-symmetry but anisotropic material as the spin source (e.g., a tetragonal or orthorhombic structure) and to grow thin films with a growth axis tilted away from any high symmetry direction (e.g., tilted in a (101) or (111) orientation). In this case, the tilt of the crystal axes relative to the sample plane can break the necessary symmetries to allow a nonzero value for σ_{zj}^{z} and an associated unconventional torque. We demonstrated this qualitatively in ref. [[57]] for the tetragonal material IrO_2. Here we test this approach quantitatively. By measuring the electric-field generated spin torque for (001) and (100) thin films of IrO_2 we determine all of the independent elements of the spin torque conductivity tensor associated with the absorbed spin current, and then we test whether rotational transformations of this single tensor can provide consistent quantitative predictions for the torques in three lower-symmetry film orientations: (110), (101), and (111). We find excellent

agreement between the measurements and the predictions of the rotated tensor for both conventional and unconventional torques in all 5 crystal orientations.

4.2 Theory and crystallographic symmetry restrictions

First, one note regarding notation. The electric-field-generated torque applied to the magnetic layer in a spin-source/magnet bilayer will differ from the spin current generated in the spin-source layer by an interfacial transmission coefficient which describes what fraction of the spin current is absorbed by the magnetic layer. Spin-torque experiments therefore do not measure the spin current directly. In the following, we will assume that the interfacial transmission coefficient is to a good approximation a constant ($T < 1$) that does not depend on the thin-film orientation or the spin orientation, so that for purposes of calculating torques we can define a spin torque conductivity (STC) tensor as simply proportional to the spin Hall conductivity tensor: $\tau_{ij}^{s} = T\sigma_{ij}^{s}$. The purpose of this paper is to test this assumption, i.e., to test the degree to which rotational transformations of a single STC tensor can give an accurate description of the measured torques for different crystal orientations.

The bulk crystal symmetries for the tetragonal structure of rutile IrO_2 dictate that the spin Hall conductivity tensor can be defined in terms of three independent elements. For the corresponding STC tensor we will call these elements *a*, *b*, and *c*. If we define basis vectors in terms of the IrO_2 crystal axes as X = [100], Y = [010], and Z = [001], the most general form allowed for the STC tensor is:

$$\tau^{X} \qquad \tau^{Y} \qquad \tau^{Z}$$

$$\begin{bmatrix} 0 & 0 & 0 \\ 0 & 0 & b \\ 0 & -a & 0 \end{bmatrix} \qquad \begin{bmatrix} 0 & 0 & -b \\ 0 & 0 & 0 \\ a & 0 & 0 \end{bmatrix} \qquad \begin{bmatrix} 0 & c & 0 \\ -c & 0 & 0 \\ 0 & 0 & 0 \end{bmatrix}.$$

Examples of spin currents corresponding to purely the *a*, *b*, and *c* processes are depicted in Figure 4.1c. If a thin film of IrO_2 is grown in an orientation different than (001), one can perform a change of basis in order to define the STC tensor relative to basis vectors in the plane and perpendicular to the thin film. This is achieved through a rotational transformation of the form:

$$\tau_{ij}^{s} = \sum_{l,m,n} R_{il} R_{mj} R_{sn} \tau_{lm}^{n} \qquad (1)$$

where R_{il} are the elements of the appropriate rotation matrix. For example, for a (100) oriented IrO_2 film, using the basis vectors X = $[010]$, Y = [001], Z = [100], the STC tensor takes the form

$$\tau^{X} \qquad \tau^{Y} \qquad \tau^{Z}$$

$$\begin{bmatrix} 0 & 0 & 0 \\ 0 & 0 & a \\ 0 & -b & 0 \end{bmatrix} \qquad \begin{bmatrix} 0 & 0 & -c \\ 0 & 0 & 0 \\ c & 0 & 0 \end{bmatrix} \qquad \begin{bmatrix} 0 & b & 0 \\ -a & 0 & 0 \\ 0 & 0 & 0 \end{bmatrix}.$$

The transformed forms of the STC tensor appropriate for the (101), (110), and (111) thin-film orientations of IrO_2 are listed in the Appendix.

4.3 Determining non-zero SHC components

To determine the full STC tensor in IrO_2, the three elements *a, b,* and *c* must be experimentally measured. Spin-torque measurements in spin-source/magnet bilayer samples are only sensitive to spin currents flowing perpendicular to the sample plane,

because only for this flow direction can the spin current be transmitted to the magnetic layer to exert a torque. This means that only the elements in the bottom rows (i.e., σ_{Zj}^{S}) of the STC tensor are accessible. The first element, a, can be measured using the (001)-orientated film, where an electric field is applied along the [010] direction resulting in a $[\bar{1}00]$-polarized spin current flowing in the out-of-plane [001] direction as indicated in Figure 4.1b. The second element, *b*, can be measured using the (100) orientation, with an electric field applied along the in-plane [001] direction resulting in a $[0\bar{1}0]$-polarized spin current flowing in the out-of-plane [100] direction seen in Figure 4.1e. The third and last term, *c*, can also be measured in the (100) orientation. An electric field applied along the [010] direction results in a $[001]$-polarized spin current flowing in the out-of-plane [100] direction seen in Figure 4.1g.

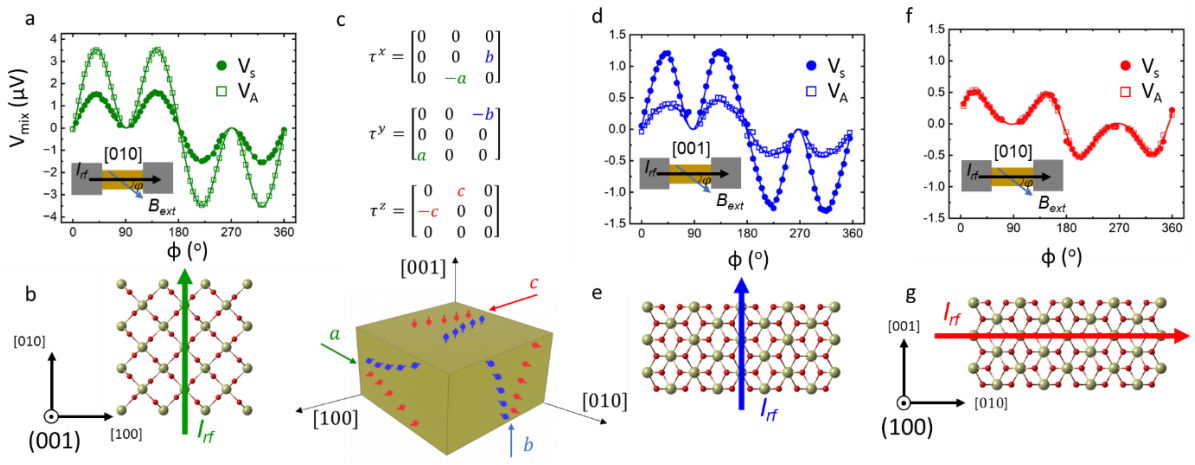

Figure 4.1: a, Symmetric and antisymmetric ST-FMR amplitudes as a function of magnetic-field angle for the (001) orientation with charge current along the [010] direction as depicted in b. c, experimental determination of the 3 non-zero STC elements using the (001) and (100) orientations. d, ST-FMR amplitudes as a function of magnetic-field angle for the (100) orientation with charge current along the [001] direction, as depicted in e. f, ST-FMR amplitudes as a function of magnetic-field angle for the (100) orientation with charge current along the [010] direction, as depicted in g.

To measure the electric-field-generated torques experimentally, high crystalline thin films of IrO_2 were grown via RF magnetron sputtering on different orientations of TiO_2 substrates, then capped *in situ* with ferromagnetic permalloy (Py), and patterned into device structures

using the same methods described in our previous report[57]. High resolution x-ray diffraction (HRXRD) demonstrated a single high crystalline phase for all five thin-film IrO_2 orientations studied in this paper: (001), (100), (110), (101), and (111) (see Figure 4.2a-e), and scanning transmission electron microscopy (STEM) also demonstrated sharp IrO_2/Py interfaces using STEM as shown in Figure 4.2f-i. The spin-torque ferromagnetic resonance (ST-FMR) technique was used to characterize the SHC components by measuring ST-FMR resonance spectra as a function of sweeping the magnetic-field magnitude for a series of different directions of the magnetic-field within the plane of the sample.

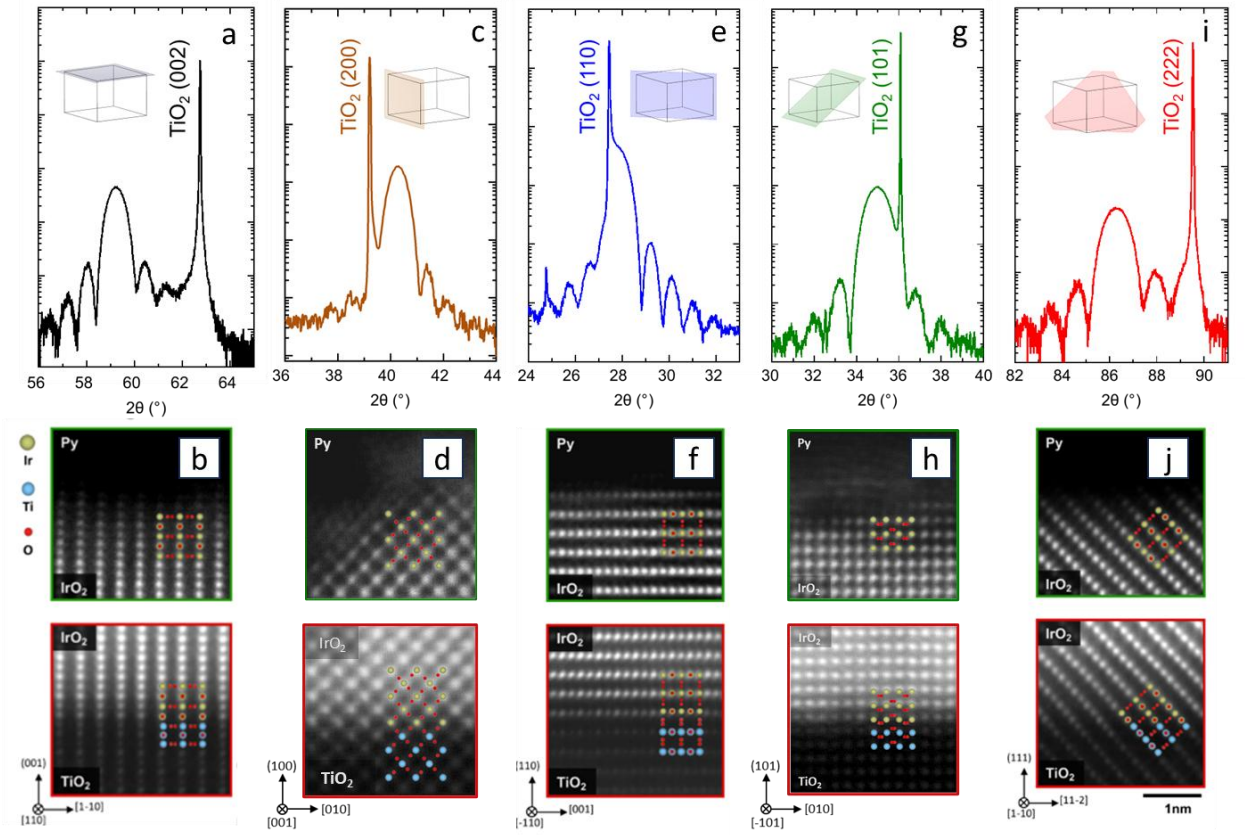

Figure 4.2: a, HR-XRD of the out of plane (002) peak and b, STEM of the interface between IrO_2 and Py and TiO_2 and IrO_2 with [1-10] zone axis. c, HR-XRD of the out of plane (200) peak and d, STEM of the interface between IrO_2 and Py and TiO_2 and IrO_2 with [010] zone axis. e, HR-XRD of the out of plane (110) peak and f, STEM of the interface between IrO_2 and Py and TiO_2 and IrO_2 with [001] zone axis. g, HR-XRD of the out of plane (101) peak and h, STEM of the interface between IrO_2 and Py and TiO_2 and IrO_2 with [010] zone axis. And i, HR-XRD of the out of plane (222) peak and j, STEM of the interface between IrO_2 and Py and TiO_2 and IrO_2 with [11-2] zone axis.

The symmetric and antisymmetric ST-FMR amplitudes for the (001) and (100) orientations are shown in Figure 4.1a,d, and f as a function of the angle of an in-plane applied magnetic field. The symmetric signals allow us to determine the three independent elements that define the anti-damping STC tensor of IrO_2. The first term *a*, determined in the (001) orientation, has a value of 520 ± 19 ($\frac{\hbar}{e}\ (\Omega\ \mathrm{cm})^{-1}$). The second term *b*, determined in the (100) orientation with an electric field applied along the [001] direction, has a value of 238 ± 5 ($\frac{\hbar}{e}\ (\Omega\ \mathrm{cm})^{-1}$). The third term *c* determined in the (100) orientation with electric field along the [010] direction, has a value of 493 ± 15 ($\frac{\hbar}{e}\ (\Omega\ \mathrm{cm})^{-1}$). As required by symmetry for the (001) and (100) orientations with these electric-field directions, we detect no unconventional torque components.

To test whether this same tensor gives a quantitative description of both the conventional and unconventional torques for other thin-film orientations, we also performed ST-FMR measurements for (110), (101), and (111) IrO_2 thin films. For each thin-film orientation, the measurements were made using various directions (ψ) of in-plane electric field (and hence charge current), with ψ measured relative to the direction defined as the X axis for that orientation. For convenience in distinguishing the conventional and unconventional torques, we will plot the measured torque tensor components using a different set of coordinate axes (using lower-case x, y, and z), in which the x axis is along the applied electric field direction and z remains normal to the sample plane. The anti-damping torque components we measure for each orientation are then the conventional in-plane torque perpendicular to *E* (the tensor component τ_{zx}^{y}), the unconventional in-plane torque parallel to E (τ_{zx}^{x}), and the

unconventional out-of-plane torque (τ_{zx}^{z}). The results are shown as the symbols within the Figure 4.3 graphs. The solid lines in Figure 4.3 are the predicted STC values from the rotated experimental tensor, using the values of *a*, *b*, and *c* as determined above with no adjustable fit parameters. We find that, by using the STC tensor elements from the experimental (001) and (100) ST-FMR results and assuming the torque is governed by the bulk symmetries of IrO_2, the tensor rotation gives a good description of both the conventional and unconventional torque components for the other orientations. For the (100), (110), (101), and (111) orientations, an unconventional in-plane STC was observed and followed the expected sin(2ψ) angular dependence, with a magnitude within 30 ($\frac{\hbar}{e}$ $(\Omega\ \mathrm{cm})^{-1}$) of the value predicted by the tensor rotation.. For the (101) and (111) orientations, unconventional out-of-plane anti-damping torque was also present, following an expected sin(ψ) dependence, with a magnitude within 10 ($\frac{\hbar}{e}$ $(\Omega\ \mathrm{cm})^{-1}$) compared to the expectation from the tensor rotation. Both types of unconventional torques are significantly weaker than the conventional in-plane anti-damping torques, but this is fully consistent with the tensor rotation given the measured values of *a*, *b*, and *c*. For example, in the (111) orientation, the largest amplitude predicted by the tensor rotation for the out-of-plane anti-damping torque is predicted to be $(a - c)/2$ = 14 ± 24 ($\frac{\hbar}{e}$ $(\Omega\ \mathrm{cm})^{-1}$) or less than 3% of the conventional torque for the (001) orientation. For the conventional in-plane anti-damping torque, the tensor rotation correctly predicts the observed dependence on the electric-field angle, but the magnitudes in some cases show somewhat larger deviations than for the unconventional torques. For example, the predicted conventional in-plane torque for the (111) orientation is about 20% lower than

the measurements. One possible explanation for this could be due to the surface quality of the (001) and (100) orientations compared to (111). Due to the low surface energy of the (111) orientation, the interface between IrO_2 and Py is much sharper compared to the (001) and (100) orientations which could change the spin transparency at the interface. Compared to previous measurements for IrO_2 (001) and (110) grown by reactive oxide molecular beam epitaxy, the torque magnitudes for our (110) samples are in close agreement, whereas the torques for (001) orientation in our films are about a factor of two smaller.[32] This difference could be due to an Ir spacer layer included in the previous work or due to different growth techniques. The results in Figure 4.3 correspond to anti-damping torque components. In addition, unconventional field-like torques were present in the (100), (110), (101), and (111) orientations which we attribute to anisotropic resistances within these orientations[49,61]. Additional field-like x-SOTs were observed in the (100), (101), (110), and (111) as seen in Figure 4.4 with Dresselhaus-like symmetry. We attribute this contribution to anisotropic resistivity within the material similar to other anisotropic materials such as 2D transition-metal dichalcogenides where current transverse to the applied current in the device can arise due to anisotropic resistance. These currents then result in Oersted fields that can be analyzed in the angular ST-FMR as having $\sim \sin(2\varphi)\sin(\varphi)$ angular dependance in the $V_{A,mix}$ signal.

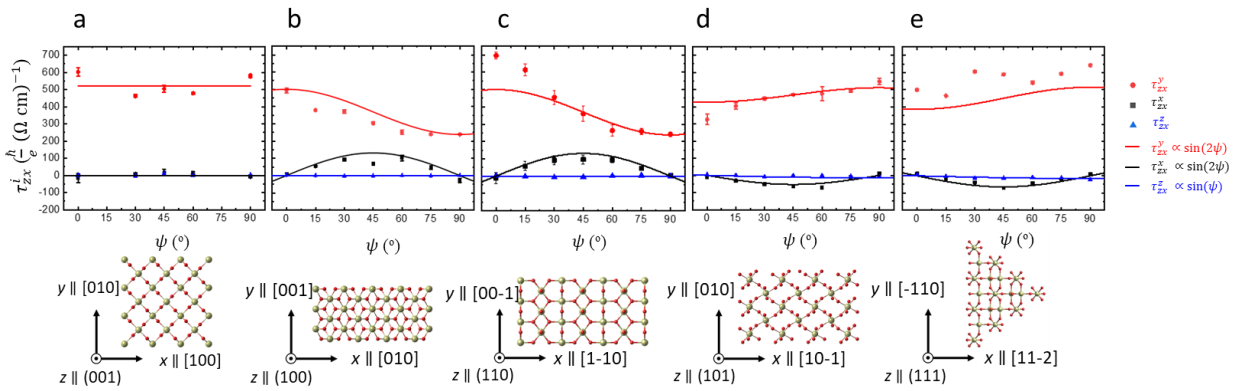

Figure 4.3: a-e, (001), (100), (110), (101), and (111) conventional and unconventional spin torque conductivities as a function of the angle ψ of the in-plane electric field with respect to the x axis shown for each projection. Solid lines represent predictions based on rotating the experimental STC tensor, using the tensor elements determined from the ST-FMR results in the (001) and (100) orientations and the bulk symmetries of IrO_2.

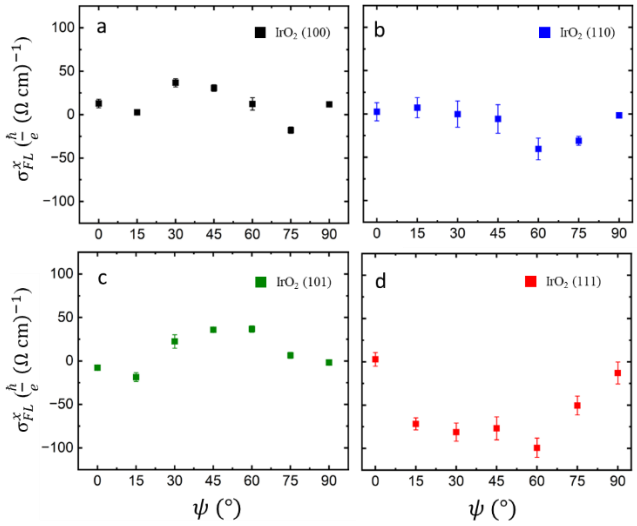

Figure 4.4: a-d, unconventional field-like x-SOTs for (100), (110), (101), and (111), respectively vs in-plane direction of the charge current.

Despite the consistency of the experimentally-determined anti-damping spin-torque tensor for different crystal orientations, the experimental results are inconsistent with density-functional-theory (DFT) calculations of the spin Hall conductivity. The DFT predictions for the elements of the spin Hall conductivity tensor corresponding to the *a*, *b*, *c* parameters of the STC tensor are a_{SHC} = 254 $(\frac{\hbar}{e}\,(\Omega\,\mathrm{cm})^{-1})$, b_{SHC} = 162 $(\frac{\hbar}{e}\,(\Omega\,\mathrm{cm})^{-1})$, and c_{SHC} = 18

($\frac{\hbar}{e}$ $(\Omega\,\mathrm{cm})^{-1}$). Despite the fact that the SHC magnitudes should be larger than the STC magnitudes on account of the interfacial spin transmission factor (T < 1), the spin Hall conductivities predict values that are too small, by more than a factor of 2 for the *a* parameter and by a factor of 27 for the *c* parameter. This leads to the measured conventional spin-orbit torques being significantly larger than expected from the DFT predictions. In contrast, the measured unconventional out-of-plane torque for low-symmetry crystal orientations is nevertheless much smaller than predicted by DFT. This is because the out-of-plane anti-damping torque is proportional to $a - c$, and this difference is much smaller for the torque parameters than the difference predicted by DFT, $a_{SHC} - c_{SHC}$. The poor agreement between measurements of spin-orbit torque and DFT predictions is true not only for IrO_2, but also for most materials including the prototypical spin source Pt [62,63]. This indicates that essential physics is still missing from this comparison. Nevertheless, since our tensor-rotation analysis depends only on the bulk symmetries of IrO_2 with no assumptions about microscopic mechanisms, predictions based on the rotated-tensor analysis remain valid and accurate. Zoomed in plots of the unconventional SOTs for the (100), (110), (101) and (111) orientations can be seen in Figure 4.5.

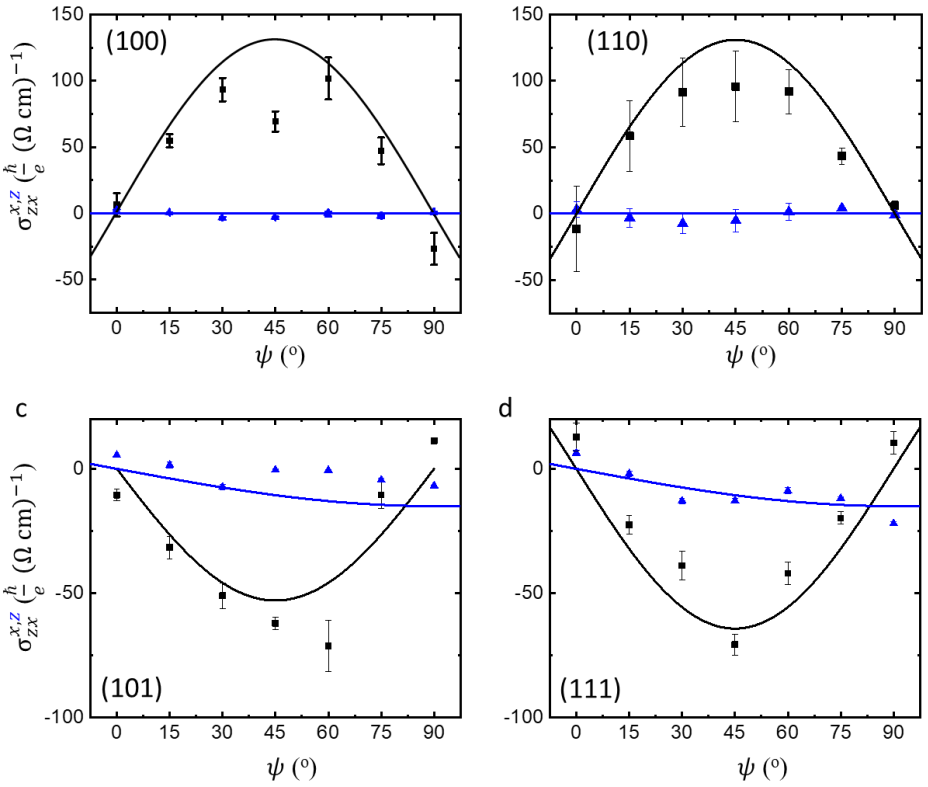

Figure 4.5: a-d, unconventional damping-like x-SOTs (black) and unconventional damping-like z-SOTs (blue) for (100), (110), (101), and (111), respectively vs in-plane direction of the charge current.

DC tuned measurements were also performed on the (001) and (100) orientations for further validation of the SHC tensor. Some oxide substrates including $SrTiO_3$, $KTaO_3$, and TiO_2 have high dielectric loss resulting in current shunting when using high frequency rf currents, which can lead to a large symmetric V_{mix} during ST-FMR measurements[17]. DC tuned measurements have been used as an independent way to measure the spin Hall conductivity which applies a constant dc current in addition to the rf current during ST-FMR measurements, which can be used to isolate the true SHC of a material as the rf current shunting should not be affected by the applied dc current. The linear relationship between the linewidth of the mixing voltage signal during ST-FMR measurements and the DC current can be used to determine the SHC. During the DC-tuned measurements, a DC bias was applied at currents ranging between -2

to 2 mA in addition to a fixed rf current by using a bias tee. The spin Hall angle can be determined using the following equation:

$$\theta_{DL} = \frac{2e}{\hbar}\left(\frac{(H_{FMR} + \frac{M_{eff}}{2})\mu_0 M_s t_{Py}}{\sin(\varphi)}\right)\frac{\Delta\alpha_{eff}}{\Delta J_c}$$

Where t_{Py} is the thickness of permalloy and $\frac{\Delta\alpha_{eff}}{\Delta J_c}$ is the linear slope of effective damping coefficient, determined from the linear relationship between the linewidth (w) and the frequency $w = w_0 + \left(\frac{2\pi}{\gamma}\right) * f$, vs the charge current going through the IrO_2 layer determined using parallel resistor model. Figure 4.5 shows the DC tuned results for (001) oriented IrO_2, (100) oriented IrO_2 with current along the [001] direction, and (100) oriented IrO_2 with current along the [010] direction and the results are summarized in Table 4.1. Although the DC-tuned results are in good agreement with the theoretical calculations, we chose to use the angular ST-FMR results for the experimental SHC tensor to compare to the other orientations in the main text as determining the unconventional SHCs can be difficult and not straight forward using DC-tuned techniques.

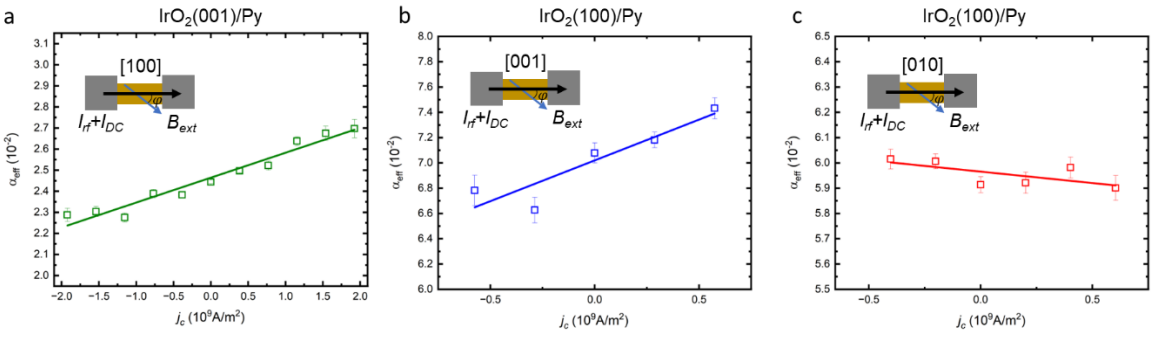

Figure 4.6: a, DC-tuned ST-FMR for the (001) orientation, b, (100) orientation with current along the [001] direction, and c, (100) orientation with current along the [010] direction where α_{eff} is the effective gilbert damping coefficient and j_c is the DC current going through the IrO_2 layer.

Table 4.1: Summary of angular and DC-tune ST-FMR results for the (001) and (100) orientations giving the 3 non-zero SHC terms a ,b and c.

Orientation	SHC term	Method	θ^y	σ^y $(\frac{\hbar}{e}\ (\Omega\ \mathrm{cm})^{-1})$
IrO_2(001) j_c ‖ [010]	*a*	Angular ST-FMR	0.12±0.01	520 ± 19
IrO_2(001) j_c ‖ [010]	*a*	DC-tuned	0.035± 0.003	247 ± 21
IrO_2(100) j_c ‖ [001]	*b*	Angular ST-FMR	0.08 ± 0.002	238 ± 5
IrO_2(100) j_c ‖ [001]	*b*	DC-tuned	0.06 ± 0.015	190 ± 50
IrO_2(100) j_c ‖ [010]	*c*	Angular ST-FMR	0.20±0.006	493 ± 15
IrO_2(100) j_c ‖ [010]	*c*	DC-tuned	-0.03 ± 0.006	-34 ± 14

4.5 Conclusion

We have experimentally determined the full anti-damping spin torque conductivity tensor for IrO_2, and showed that this single tensor provides consistent and accurate results of the measured electric-field-driven torques for five different thin-film orientations, including both conventional and unconventional torques. The good agreement between the experimental measurements of the anti-damping spin torques and the predictions from the tensor rotation in Figure 4.3 confirm that the electric-field-induced torques generated by IrO_2 originate from bulk spin currents within the IrO_2, with perhaps a minor contribution to the conventional spin torque in the (111) orientation from an additional interfacial effect. We observe no indication of large differences in interfacial spin transmission for different crystal orientations that would invalidate the tensor analysis. In addition, the tensor analysis show that it is possible to fully characterize the spin-torque tensor of an anisotropic material using measurements of conventional spin-orbit torque for selected high-symmetry crystal

orientations, and then to obtain accurate predictions of the unconventional torques for lower-symmetry crystal orientations by means of a simple tensor rotation.

Chapter 5 Orbital Hall effect in IrO_2

5.1 Introduction

The recent discovery of orbital currents has opened the possibility of utilizing the orbital degree of freedom of electrons as an information carrier, promoting orbitronics as a promising candidate for next-generation quantum technology beyond the conventional electronics.[64,65] The orbital Hall effect (OHE)[66–71] – a phenomenon where an orbital-polarized current is generated by an external electric field – has been verified in various experiments via magneto-optical effect[72,73], magnetoresistance[74–77], and current-induced torques[78–84] . The OHE is particularly promising for spintronics due to its ability to manipulate magnetization when orbital angular momentum is injected to a ferromagnet[85], which may surpass the efficiency of other conventional mechanisms based on spin currents such as spin Hall effect (SHE). Moreover, the OHE can be much stronger than the SHE in broad range of materials, including environment-friendly and non-toxic elements[86].

However, the main difficulty in detecting orbital current by current-induced torque measurements has been to unambiguously disentangle the spin and orbital current contributions to the torque. Previous works have partly resolved the issue by measuring the current-induced torque for different ferromagnets[79,81], which sensitively depends on the correlation between the spin and orbital angular momenta in the electronic structure and by converting orbital current to spin current by an insertion layer with strong spin-orbit coupling (SOC) such as Pt[78,82]. Orbital current has also been clarified by examining its long-range characteristics of the dephasing in a ferromagnet, which can be significantly longer than the

spin dephasing length ~< 1nm [83,84,87]. However, most of the experiments performed so far rely on several assumptions and quantitative estimation by theory.

In this work, we demonstrate an unambiguous way to disentangle the SHE and OHE by utilizing the crystal-symmetry-dependent orbital Hall conductivity (OHC) and spin Hall conductivity (SHC) tensors. Because the energy bands with different orbital characters are split by the crystal-field potential, the OHC varies significantly depending on the crystal orientation. Here, we use spin torque ferromagnetic resonance (ST-FMR) in various orientations of IrO_2 with a Ni detection overlay to uncover the crystallographic dependance of the OHC orbital torques. In comparison with theoretical calculations, we find qualitative agreement for the relative signs for the experimentally determined OHC and SHC in the (001) and (100) orientations. We also find orbital contributions for the unconventional out-of-plane polarization in the (111) orientation. These results can provide alternative approaches for highly efficient low power spintronic devices.

5.2 Theory and observation of OHC using Ni

We study IrO_2 epitaxial thin films grown via RF magnetron sputtering on TiO_2 (001), (100), and (111) substrates. We use spin-torque ferromagnetic resonance (ST-FMR) measurements to determine the SHC and OHC. To experimentally distinguish the spin and orbital contributions to the torque on the magnetization, we perform separate measurements on IrO_2/Py and IrO_2/Ni. We assume that Py is insensitive to orbital currents, while Ni is susceptible to both spin and orbital currents. Importantly, we utilize the distinct absorption lengths for the spin and orbital angular momenta in Ni, where the orbital torque is long-

ranged over several nanometers. By varying the thickness of the Ni layer, we can fit the experimental results to:

$$\sigma^{i}_{jk\ net} = \sigma^{i}_{jk\ SHC} + \sigma^{i}_{jk\ OHC,eff}[1 - \mathrm{sech}\left(\frac{t_{Ni}}{\lambda_{Ni}}\right)] \quad (1)$$

where $\sigma^{i}_{jk\ SHC}$ is the SHC contribution, $\sigma^{i}_{jk\ OHC,eff}$ is the effective OHC contribution, and λ_{Ni} is the spin diffusion length. It's important to note that $\sigma^{i}_{jk\ net}$ is proportional to the total torque acting on the local magnetic moment of Ni. It incorporates the two separate contributions from the angular-momentum currents in IrO_2 and also the efficiency of transmission of those angular momentum currents across the interface to a apply a torque to the magnetic layer.

Table 5.1: Calculated spin and orbital Hall conductivity for IrO_2 in the (001) basis.

	$\boldsymbol{\sigma^x}$	$\boldsymbol{\sigma^y}$	$\boldsymbol{\sigma^z}$
IrO_2 a = b = 4.498 Å c = 3.154 Å x‖ [100] y‖ [010] z‖ [001]	$\begin{bmatrix} \sigma^{x}_{xx} & \sigma^{x}_{xy} & \sigma^{x}_{xz} \\ \sigma^{x}_{yx} & \sigma^{x}_{yy} & \sigma^{x}_{yz} \\ \sigma^{x}_{zx} & \sigma^{x}_{zy} & \sigma^{x}_{zz} \end{bmatrix}$	$\begin{bmatrix} \sigma^{y}_{xx} & \sigma^{y}_{xy} & \sigma^{y}_{xz} \\ \sigma^{y}_{yx} & \sigma^{y}_{yy} & \sigma^{y}_{yz} \\ \sigma^{y}_{zx} & \sigma^{y}_{zy} & \sigma^{y}_{zz} \end{bmatrix}$	$\begin{bmatrix} \sigma^{z}_{xx} & \sigma^{z}_{xy} & \sigma^{z}_{xz} \\ \sigma^{z}_{yx} & \sigma^{z}_{yy} & \sigma^{z}_{yz} \\ \sigma^{z}_{zx} & \sigma^{z}_{zy} & \sigma^{z}_{zz} \end{bmatrix}$
SHC $(\frac{\hbar}{e}\ (\Omega\ \mathrm{cm})^{-1})$	$\begin{bmatrix} 0 & 0 & 0 \\ 0 & 0 & 162 \\ 0 & -254 & 0 \end{bmatrix}$	$\begin{bmatrix} 0 & 0 & -162 \\ 0 & 0 & 0 \\ 254 & 0 & 0 \end{bmatrix}$	$\begin{bmatrix} 0 & 18 & 0 \\ -18 & 0 & 0 \\ 0 & 0 & 0 \end{bmatrix}$
OHC $(\frac{\hbar}{e}\ (\Omega\ \mathrm{cm})^{-1})$	$\begin{bmatrix} 0 & 0 & 0 \\ 0 & 0 & 160 \\ 0 & 77 & 0 \end{bmatrix}$	$\begin{bmatrix} 0 & 0 & -160 \\ 0 & 0 & 0 \\ -77 & 0 & 0 \end{bmatrix}$	$\begin{bmatrix} 0 & -194 & 0 \\ 194 & 0 & 0 \\ 0 & 0 & 0 \end{bmatrix}$

Based on our DFT calculations, IrO_2 is predicted to generate a large anisotropic orbital Hall effect depending on the charge current direction. The SHC denoted as σ^{i}_{jk} (where *i* is the spin

polarization direction, *j* is the spin flow direction, and *k* is the charge current direction) is a 27-element property tensor of a material. For high symmetry materials only some of these elements are non-zero due to crystal symmetry restrictions. For IrO_2, the symmetry of the tetragonal rutile crystal structure only allows for 3 non-zero unique SHC terms including σ_{zy}^{x}, σ_{yz}^{x}, and σ_{xy}^{z}. This is also the case for the OHC tensor. The IrO_2 calculation results for both SHC and OHC for IrO_2 are shown in Table 5.1. Due to the anisotropy of the SHC and OHC tensors, measuring the contributions from spin polarization and orbital polarization have different dependence on the charge current direction. For example, considering the (001) orientation with charge current along the [-100] direction, spin polarization along the [010] direction, and spin current along the (001) direction is calculated to generate a positive SHC and negative OHC as shown in Figure 5.1a where the orbital Berry curvatures exhibit highly anisotropic feature, and their hotspots can significantly differ in the Brillouin zone. This is the direct consequence of the anisotropic orbital-dependent level splitting. Next, considering the (100) orientation with charge current along the [010] direction, spin polarization along the [00-1] direction, and spin current along the (100) direction should generate a positive SHC and positive OHC as shown in Figure 5.1b where the spin and orbital Berry curvatures both show positive hotspots. Lastly, considering the (010) orientation with charge current along the [001] direction, spin polarization along the [-100] direction, and spin current along the (010) direction should generate a positive SHC and negative OHC as shown in Figure 5.1c where the spin Berry curvature shows positive hotspots, and the orbital Berry curvature shows negative hotspots. This demonstrates that the anisotropy of SHC and OHC in IrO_2 can be distinguished by measuring $\sigma_{jk\ net}^{i}$ for the different crystal orientations.

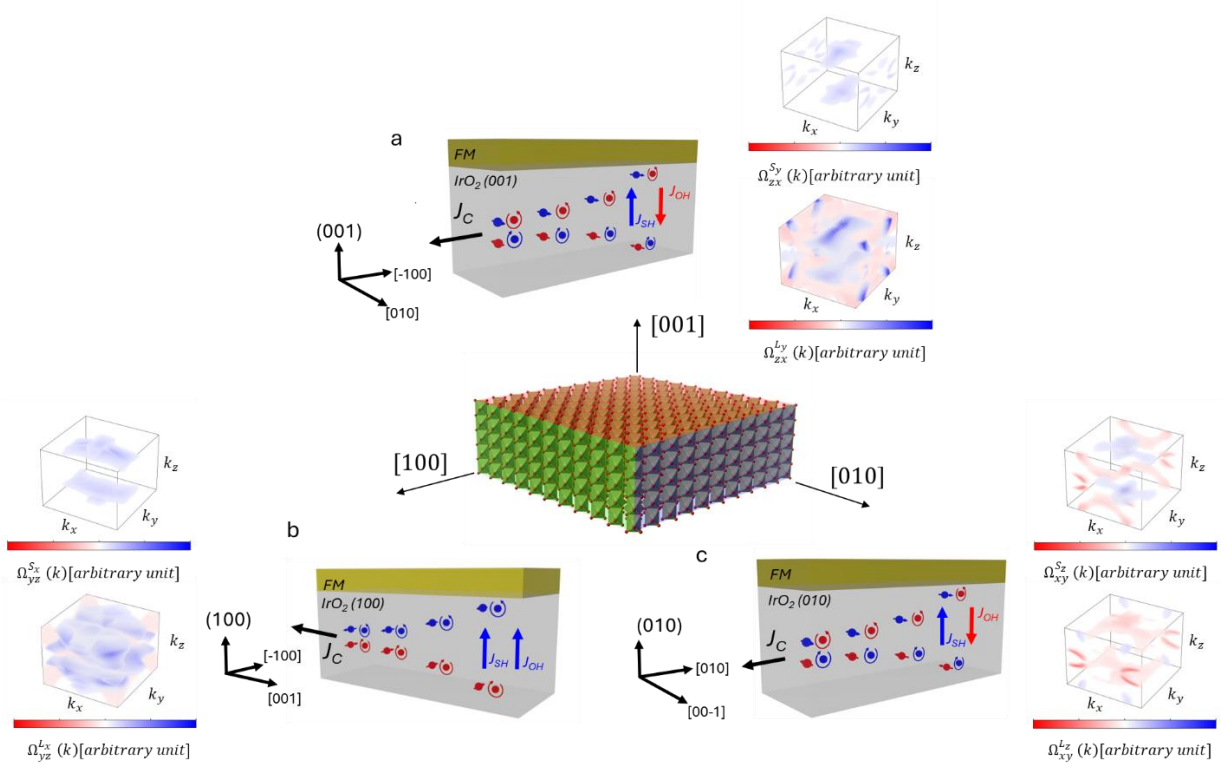

Figure 5.1: a, spin Hall conductivity and orbital Hall conductivity for IrO_2 for a, the (001), b, the (100), and c, the (010) orientations with spin and orbital Berry curvature for each orientation.

To determine the σ_{zy}^{x}, σ_{yz}^{x}, and σ_{xy}^{z} terms, we measure the (001) orientation which gives σ_{zy}^{x} with charge current along any in-plane direction and measure the (100) orientation which gives $-\sigma_{yz}^{x}$, with charge along the [001] direction, and $-\sigma_{xy}^{z}$ with charge current along the [010] direction. The experimental results can be seen in Figure 5.2 where the value at $t_{Ni} = 0$ is the reference point from the IrO_2/Py bilayers which should have very little sensitivity to OHC contributions, and thus represent the spin current contribution. The results for the (001) orientation, which allows to probe σ_{zy}^{x}, show a decreasing trend with increasing Ni thickness, implying a negative orbital Hall contribution and exhibiting a spin diffusion length of 5.8 $\pm$ 1nm. This qualitatively agrees with the relative signs for SHC and OHC from the theoretical calculations. Next, we find OHC contributions with the same sign as SHC in the (100)

orientation along the [001] direction with spin diffusion length of 4 ± 0.6nm and OHC contributions with opposite sign to SHC for charge current along [010] with spin diffusion length of 2.1 ± 0.7nm, agreeing qualitatively to the theoretical predictions.

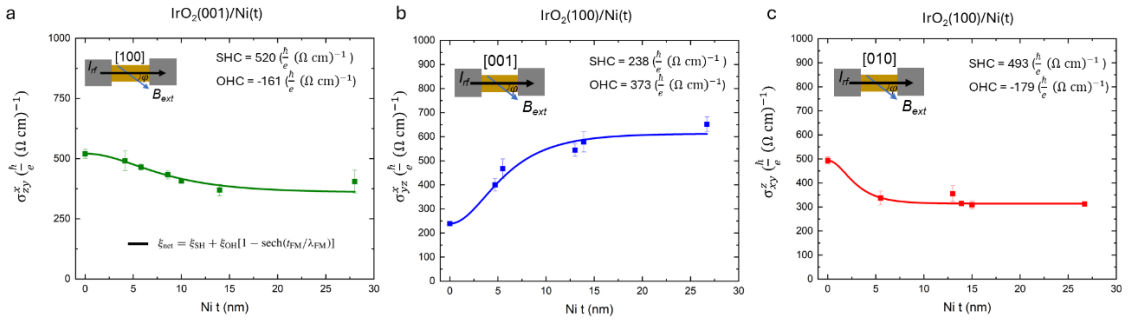

Figure 5.2: a Spin Hall Conductivity vs Ni thickness for (001) oriented IrO_2, b for (100) oriented IrO_2 with charge current along the [001] direction, and c for (100) oriented IrO_2 with charge current along the [010] direction.

Lastly, we study the OHC contributions in the IrO_2 (111) orientation, which hosts unconventional SOTs due to the low crystalline symmetry in this orientation. The OHC contributions can be seen in both the $[11\bar{2}]$ (defined as capital *Y*) and $[1\bar{1}0]$ (defined as capital *X*) directions seen in Figure 5.3a and b, respectively. In both cases, the SHC and OHC show positive contributions. Additionally, we study the angular ST-FMR with current along the $[1\bar{1}0]$ which should generate the unconventional z-spin polarized current. In the IrO_2 (111)/Py samples, we found a small non-zero unconventional z-spin SHC of 8 ± 1 $(\frac{\hbar}{e}\ (\Omega\ \mathrm{cm})^{-1})$. In the IrO_2 (111)/Ni samples, we find a large increase with increasing thickness for Ni, indicating a large unconventional OHC with z-polarization of 40 ± 8 $(\frac{\hbar}{e}\ (\Omega\ \mathrm{cm})^{-1})$ seen in Figure 5.3c.

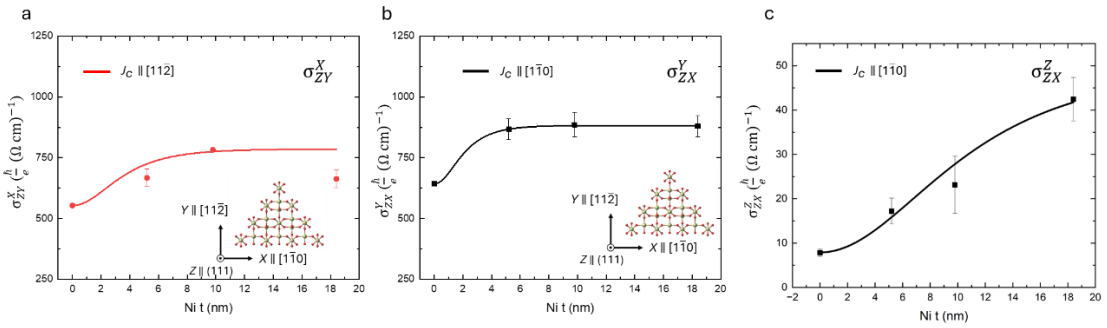

Figure 5.3: a Conventional OHC contributions for IrO_2 (111) for various Ni thickness for charge current along the $[11\bar{2}]$, b conventional OHC contributions for IrO_2 (111) for various Ni thickness for charge current along the $[1\bar{1}0]$, and c, the unconventional z-polarized contribution of the OHC for charge current along the $[1\bar{1}0]$. Here, we define X along $[1\bar{1}0]$, Y along $[11\bar{2}]$, and Z perpendicular to the (111) surface.

5.3 Orbital-spin conversion using Pt

Another approach to probe the OHC is using Pt bilayers which has been proposed and backed with experimental evidence to convert orbital currents to spin currents which can then be detected as a torque on an adjacent ferromagnet material. Although Pt itself can generate a large spin Hall effect, by growing a Pt/Py/Pt heterostructure where both Pt layers have the same thickness we can effectively cancel out all contributions from Pt. Based on other reports, we chose a thickness of ~1.5nm of Pt which should allow for maximum conversion[84]. The finite symmetric voltage signal we found in the Pt/Py/Pt control sample is likely due to RF current shunting into the TiO_2 substrate due to high dielectric loss which is a known problem in other oxide substrates[17]. To minimize signals coming from the substrate, we measure DC-tuned ST-FMR which applies a constant dc current in addition to the rf current during ST-FMR measurements, which can be used to isolate the true SHC of a material as the rf current shunting should not be affected by the applied dc current[17–19]. The linear relationship between the linewidth of the mixing voltage signal during ST-FMR measurements and the DC current can be used to determine the SHC which is proportional

to $\frac{\Delta\alpha_{eff}}{\Delta J_c}$ where the sign of the slope indicates the sign of the SHC. During the DC-tuned measurements, a DC bias was applied at currents ranging between -2 to 2 mA in addition to a fixed rf current by using a bias tee. The spin Hall angle can be determined using the following equation:

$$\theta_{DL} = \frac{2e}{\hbar}\left(\frac{(H_{FMR} + \frac{M_{eff}}{2})\mu_0 M_s t_{Py}}{\sin(\varphi)}\right)\frac{\Delta\alpha_{eff}}{\Delta J_c}$$

Where t_{Py} is the thickness of permalloy and $\frac{\Delta\alpha_{eff}}{\Delta J_c}$ is the linear slope of effective damping coefficient, determined from the linear relationship between the linewidth (w) and the frequency $w = w_0 + \left(\frac{2\pi}{\gamma}\right) * f$, vs the charge current going through the IrO_2 layer determined using parallel resistor model. Finally, we can obtain the spin Hall conductivity from $\sigma_{jk}^{i} = \frac{\theta_i}{\rho_{IrO2}}\frac{\hbar}{2e}$. In the Pt/Py/Pt control sample, we find no change in the damping coefficient vs varying DC current seen in Figure 5.4b. We then measured the DC-tuned ST-FMR for IrO_2 (001) and (100) with Pt/Py/Pt. For the (001) orientation seen in Figure 5.4a, we find the SHC to be 188 $\pm$ 16 ($\frac{\hbar}{e}$ $(\Omega\,\mathrm{cm})^{-1}$) compared to IrO_2 (001)/Py of 247$\pm$ 14 ($\frac{\hbar}{e}$ $(\Omega\,\mathrm{cm})^{-1}$). For the (100) orientation with charge current along the [001] direction seen in Figure 5.4b, we find the SHC to be 310 $\pm$ 21 ($\frac{\hbar}{e}$ $(\Omega\,\mathrm{cm})^{-1}$) compared to IrO_2 (100)/Py of 190$\pm$ 50 ($\frac{\hbar}{e}$ $(\Omega\,\mathrm{cm})^{-1}$). Lastly, for the (100) orientation with charge current along the [010] direction seen in Figure 5.4d, we find the SHC to be -171 $\pm$ 8 ($\frac{\hbar}{e}$ $(\Omega\,\mathrm{cm})^{-1}$) compared to IrO_2 (100)/Py of -34 $\pm$ 14 ($\frac{\hbar}{e}$ $(\Omega\,\mathrm{cm})^{-1}$). In Table 5.2, we summarize the results from IrO_2/Py which should not be sensitive to orbital currents, to the IrO_2/Pt/Py/Pt samples for both angular ST-FMR and DC-tuned ST-FMR.

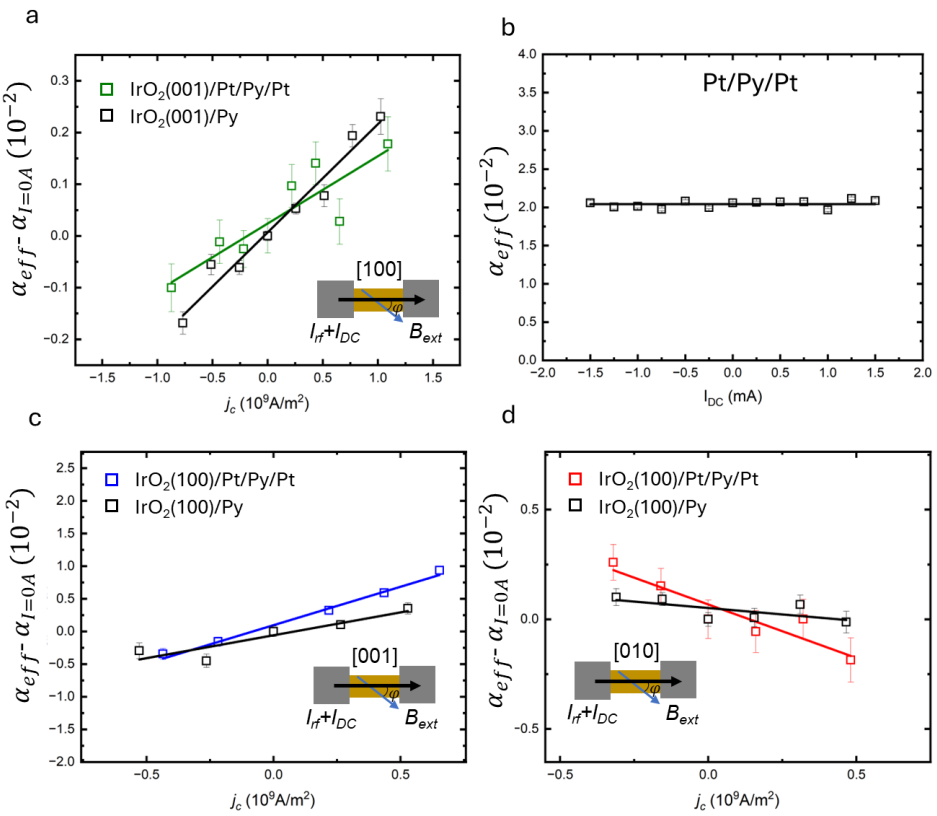

Figure 5.4: a DC-tuned ST-FMR for IrO_2(001)/Pt/Py/Pt and IrO_2(001)/Py, b DC-tuned ST-FMR for IrO_2(100)/Pt/Py/Pt and IrO_2(100)/Py with charge current along the [001] direction, c DC-tuned ST-FMR for IrO_2(100)/Pt/Py/Pt and IrO_2(100)/Py with charge current along the [010] direction, and d, DC-tuned ST-FMR for Pt/Py/Pt control sample.

Table 5.2: Spin Hall angle $\boldsymbol{\theta^y}$ and spin Hall conductivity $\boldsymbol{\sigma^y}$ ($\frac{\hbar}{e}$ $(\Omega\ cm)^{-1}$) for IrO_2/Py and IrO_2/Pt/Py/Pt bilayers for angular ST-FMR and DC-tuned ST-FMR measurements.

Sample	$\boldsymbol{\theta^y_{DC-tuned}}$	$\boldsymbol{\sigma^y_{DC-tuned}}$
IrO_2(001)/Py	0.035± 0.003	247 ± 21
IrO_2(001)/Pt/Py/Pt	0.036 ± 0.002	188± 16
IrO_2(100)/Py [00$\bar{1}$]	0.06 ± 0.015	190 ± 50
IrO_2(100)/Pt/Py/Pt [00$\bar{1}$]	0.068 ± 0.003	310 ± 21
IrO_2(100)/Py [010]	-0.03 ± 0.006	-34 ± 14
IrO_2(100)/Pt/Py/Pt [010]	-0. 057 ± 0.002	-171 ± 8

5.4 Conclusion

These results demonstrate a large orbital Hall conductivity present in IrO_2 with a strong dependence on crystallographic symmetry. We extract the OHC from the experimental torque measurements by measuring samples with Ni thicknesses spanning the absorption length of orbital angular momentum for the (001), (100), and (111) oriented IrO_2. In the (001) orientation, a decreasing experimental torque signal with increasing Ni thickness indicates an OHC contribution opposite in sign to the SHC. For the (100) orientation, we find similar OHC contributions for current along the [010] and [00$\bar{1}$] directions, agreeing with theoretical predictions. We also find evidence for a large unconventional OHC in IrO_2 (111). These results provide design approaches for efficient spintronic and orbitronic devices by tuning the strength of the spin Hall effect vs orbital Hall effect via the crystallographic orientation. Additionally, these results offer an alternative approach for highly efficient field-free magnetic switching using unconventional out-of-plane spin and orbital currents. Further experiments using PMA switching can give insight into the switching efficiency for orbital currents compared to spin currents by using IrO_2 (111)/Pt bilayers. This work also opens new avenues for orbitronics using oxide systems which have additional tuning knobs such as octahedral rotations, strain engineering, stoichiometry, and other thin film engineering tools. Using these engineering approaches in other oxide systems that may host large OHC could demonstrate the advantages of using oxide systems for spintronic and orbitronic applications.

Supplemental Note: First-principles calculations

For the computation of the orbital Hall conductivity (OHC) and spin Hall conductivity (SHC) in IrO_2, we carry out the three-step calculation based on first-principles methods. In the first step, we perform self-consistent density functional theory (DFT) calculation, by employing the FLEUR code which implements the full-potential linearly augmented plane wave (FLAPW) method[88]. For the exchange and correlation effects, we use the Perdew-Burke-Ernzerhof functional[89] based on the generalized gradient approximation. The lattice constants are set $a_1 = a_2 = 8.50a_0$ and $a_3 = 5.96a_0$ in the rutile structure, where a_0 is the Bohr radius. The fractional coordinates of atoms are given by

Atom	c_1	c_2	c_3
Ti-1	0.0	0.0	0.0
Ti-2	0.5	0.5	0.5
O-1	0.1916	0.8084	0.5
O-2	0.3084	0.3084	0.0
O-3	0.6916	0.6916	0.0
O-4	0.8084	0.1916	0.0

by which the relative position of an atom with respect to the center of the unit cell is $\delta\boldsymbol{r} = c_1\boldsymbol{a}_1 + c_2\boldsymbol{a}_2 + c_3\boldsymbol{a}_3$. The following calculation parameters specific to the FLAPW method are used: $R_{\mathrm{Ir}} = 2.30a_0$ and $R_{\mathrm{O}} = 1.30a_0$ for the muffin-tin ardii of Ir and O atoms, respectively, $l_{\max} = 12$ for the harmonic expansion in the muffin-tin for both Ir and O atoms, and $K_{\max} =$

$5.0a_0^{-1}$ for the plane wave cutoff in the interstitial region. We sample the **k**-points in the first Brillouin zone on the $12 \times 12 \times 16$ Monkhorst-Pack mesh.

In the second step, from the converged electronic structure from the DFT calculation, i.e. the potential and Kohn-Sham states, we construct maximally localized Wannier functions (MLWFs) by employ the WANNIER90 code[90] which is interfaced with the FLEUR code[91]. We project the Kohn-Sham states onto $d_{xy}, d_{yz}, d_{zx}, d_{x^2-y^2}, d_{z^2}$ orbitals on Ir site and p_x, p_y, p_z orbitals on O site as the initial guess and iteratively minimize the spread of the Wannier functions. For the disentanglement, we set the maximum of the frozen energy window 3 eV above the Fermi energy. All the necessary operators (Hamiltonian, position, orbital angular momentum, and spin), which are first represented in the Kohn-Sham states in **k**-space, are transformed into the representations based on the MLWFs in real space.

In the third step, we diagonalize the Wannier Hamiltonian in an interpolated fine **k**-mesh ($256 \times 256 \times 256$). The OHC is computed by the Kubo formula (details in[92]),

$$\sigma_{\alpha\beta}^{L_\gamma} = -\frac{e\hbar}{2}\int \frac{d^3k}{(2\pi)^3}\sum_{nn'}(f_{n\boldsymbol{k}} - f_{n'\boldsymbol{k}})\frac{\mathrm{Im}\left[\langle\psi_{n\boldsymbol{k}}|(v_\alpha L_\gamma + L_\gamma v_\alpha)|\psi_{n'\boldsymbol{k}}\rangle\langle\psi_{n'\boldsymbol{k}}|v_\beta|\psi_{n\boldsymbol{k}}\rangle\right]}{(E_{nk} - E_{n'k})^2 + \Gamma^2},$$

where $e > 0$ is the unit charge, $\hbar$ is the reduced Planck constant, n and n' are band indices, ψ_{nk} is a Bloch state with the energy eigenvalue E_{nk}, v_α and v_β are the velocity operators along α and β directions, respectively, and L_γ is the γ component of the orbital angular momentum operator. For the calculation of the SHC, L_γ is replaced by the spin operator S_γ. We introduce a phenomenological broadening by constant Γ, which we set 25 meV.

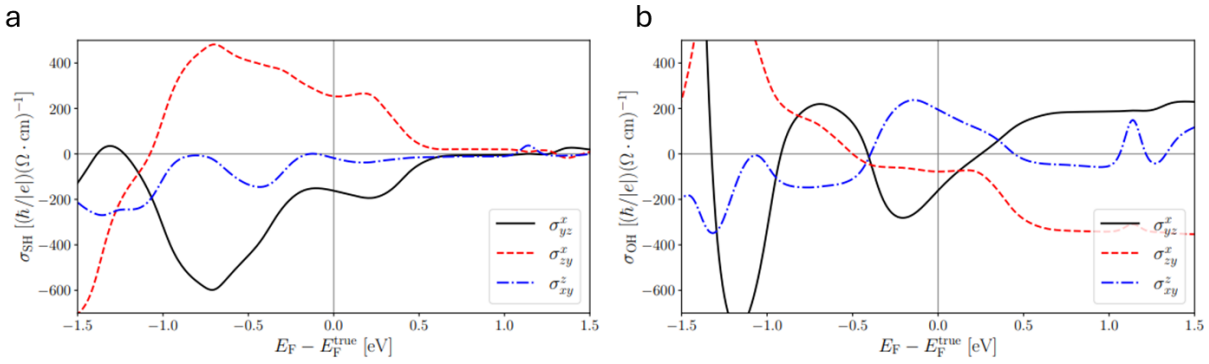

Figure 5.5: a, spin Hall conductivity for the 3 non-zero components in the (001) basis as a function of the Fermi energy. b, orbital Hall conductivity for the 3 non-zero components in the (001) basis as a function of the Fermi energy.

Chapter 6 Field-free switching via out-of-plane spin orbit torques in IrO_2 (111) thin films

6.1 Introduction

Field-free switching of perpendicular magnetic materials has promising applications for highly efficient and low power consumption spintronics devices. Field-free switching have been achieved in low symmetry materials such as antiferromagnets, transition metal dichalcogenides, magnetic trilayers, and other low crystalline symmetry materials. However, the z-spin polarized spin-orbit torque that is required to switch out-of-plane magnetic moments have typically been small leading to large current densities which is a disadvantage for commercial applications. Recent work on IrO_2 has demonstrated unconventional z-polarized spin orbit torques using angular spin torque ferromagnetic resonance measurements in the (111) orientation due to the low symmetry with respect to the out-of-plane direction. Here we demonstrate field-free perpendicular magnetic switching using IrO_2(111)/$[Pt/Co]_N$/Pt heterostructures. We find the switching current density along the [1-10] direction to be 4.7 x 10^6 A/cm^2, which is among the lowest switching current densities of materials that generate unconventional z-spin polarized currents due to low crystalline symmetry. Furthermore, we demonstrate the crystallographic dependance of the field-free switching. These results provides an alternative material for low density high efficient spintronic devices.

Spintronic devices have potential for next generation electronic applications by utilizing the spins of electrons for logic devices, memory applications, and spin detectors. Conventionally, the polarization of the spins are restricted to be orthogonal to the charge

current direction and spin current direction due to the symmetry of the material. In low symmetry materials, however, the lack of symmetry can lead to large unconventional spin-orbit torques (SOTs) that can be used for efficient field-free switching of perpendicular magnetic anisotropic (PMA) materials.[46,53,93–101] However, using SOTs for switching PMA has not been practically implemented in commercial devices due to the low efficiency of the unconventional z-SOTs in these materials. For efficient devices that can make useful in commercial applications, higher efficient materials are required.

Recent work has demonstrated the unconventional z-SOTs in semi-metallic IrO_2 demonstrated using epitaxial design by lowering the crystalline symmetry at the interface in the (111) orientation.[57] Compared to other materials systems that have shown field-free switching, IrO_2 can be easily grown on commercially available substrates and don't require membrane fabrication or other challenging heterostructure engineering. In addition, the z-SOTs can be controlled by changing the in-plane charge current direction. This has also been demonstrated in a three-fold symmetry material where the switching of PMA can be tuned.[53] This adds additional tunability that can be used in the design of spintronic memory applications.

Here, we show field-free deterministic switching of $[Pt/Co]_N$/Pt PMA multilayers using z-SOTs generated in epitaxial IrO_2 (111) thin films. We show PMA switching when current is applied along the [1-10] direction, but not in the [11-2] direction. Additionally, we show the angular dependance of the field-free switching as applied current pulses changes direction throughout the crystal structure. The field-free switching of the perpendicular magnetization is also confirmed at the same time by using polar MOKE imaging. And the angular

dependence on These results indicate that IrO_2 can be a suitable material for efficient spintronic devices.

6.2 Field-Free switching in IrO_2/Pt(Co) multilayers

IrO_2 has a rutile crystal structure that belongs to space group 136. This crystal structure has higher symmetry than other unconventional z-SOT generating materials as there are several mirror planes and rotational symmetries throughout the structure. However, the relative crystal symmetry with respect to the out-of-plane direction can be tuned by growing IrO_2 in lower symmetry orientations.[57] In the (111) orientation, only one mirror plane, the (1-10), is orthogonal to the out-of-plane direction, which leads to unconventional z-SOTs when current is applied towards that mirror plane. Our previous results demonstrated the angular dependance of these z-SOTs as the in-plane charge current was angled away from the (1-10) mirror plane using spin-torque ferromagnetic resonance (ST-FMR). Here, we make use of the unconventional z-SOTs generated in IrO_2 (111) thin films to show field-free switching of PMA.

To demonstrate the field-free switching, IrO_2 thin films were grown using rf-magnetron sputtering. Epitaxial IrO_2 was grown on TiO_2 (111) substrates by RF magnetron sputtering. IrO_2 films were grown at 320°C at a pressure of 20 mTorr with 10% oxygen partial pressure. The target power was 20 W. After growth the sample was cooled in an O_2 atmosphere. The samples were then fabricated using photolithography and ion beam milling, followed by sputter deposition of 100 nm Pt/10nm Ti and lift off techniques for the electrodes. Following the IrO_2 growth, Pt(Co) multilayers were grown ex-situ and patterned for device switching

using photolithography and ion milling techniques followed by Ti/Pt electrode growth for contact using liftoff techniques.

Field-free SOT switching experiments were then done on the IrO_2 (111)/Pt(Co) heterostructures. During the experiment, current pulses were applied along Hall bars at different in-plane directions to induce SOT switching of the PMA. The magnetization was probed by measuring the anomalous Hall resistance (R_{xy}). The SOT-induced magnetization switching is measured by anomalous Hall resistance and polar MOKE microscopy at the same time. The current pulses were applied by a Keithley B2901A current source with a duration of 1 micro-second. And the anomalous Hall resistance is recorded using a Keithley 2182A nanovoltmeter under a low probe current of 100 μA. The polar MOKE signal is measured with a microscopy from Yanghongxing Cooperation. Figure 6.1a shows the change in R_{xy} for Hall bars at different in-plane direction where 0° is the current along the [1-10] direction and 90° is current along the [11-2] direction. We find that the switching probability of the PMA increases as the current is applied closer to the orthogonal direction of [1-10]. No field-free switching was observed for currents applied 60° and 90° with respect to the (1-10) mirror plane. The critical current density for switching in the Hall bars perpendicular to the (1-10) mirror plane was measured to be 4.7×10^6 (A/cm^2).

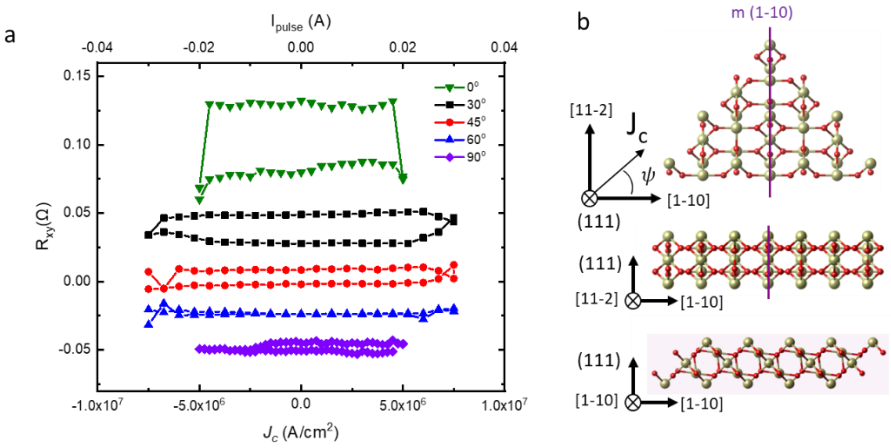

Figure 6.1: a, anomalous Hall resistance as a function of the pulsed DC current for Hall bars at various angles way from the (1-10) mirror plane. b, surface projection and in-plane crystal projections of the rutile crystal structure in the (111) orientation.

Additional measurements were done along the [1-10] Hall bars and the [11-2] Hall bars with small in-plane assisted magnetic fields. Figure 6.2c and d shows the assisted PMA switching. We find large switching probabilities for current along the [1-10] direction when small in-plane magnetic fields are applied at 10mT. This is likely due to the strong conventional SOTs present in IrO_2 which can be used to switch PMA magnetizations that are canted in-plane. In the [11-2] direction, we find assisted PMA switching with 10mT applied in-plane, again likely due to the large conventional SOTs.

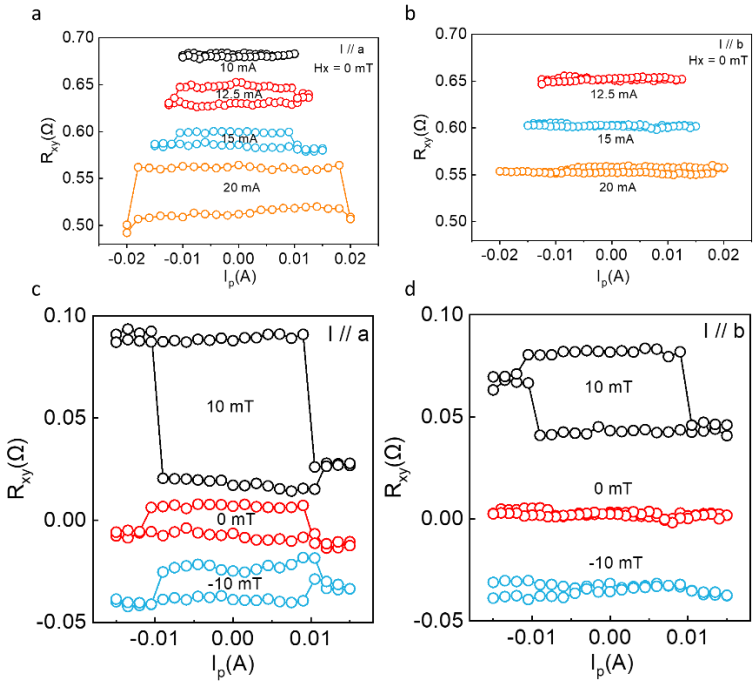

Figure 6.2: a, anomalous Hall resistance as a function of the pulsed DC current for Hall bars oriented along the [1-10] direction. b, anomalous Hall resistance as a function of the pulsed DC current for Hall bars oriented along the [11-2] direction. c, anomalous Hall resistance as a function of the in-plane assisted magnetic field for Hall bars oriented along the [1-10] direction. And c, anomalous Hall resistance as a function of the in-plane assisted magnetic field for Hall bars oriented along the [11-2] direction.

These results demonstrate the high efficiency and low current densities required for PMA switching using SOTs in IrO_2 (111) thin films. With current along the [1-10] direction, we find a critical switching current density of 4.7 x 10^6 A/cm^2, which is among the lowest materials to demonstrate deterministic field-free PMA switching as seen in Table 6.1.

Table 6.1: Comparison of critical switching current density (J_{SW}) of materials showing field-free PMA switching

Material	J_{SW} (A/cm^2) x 10^6	**Ref.**
$L1_1$ CuPt/CoPt	24	[53]
Mn_3Sn/CoTb	1.3	[98]
$TaIrTe_4$	2.35	[99]
YIG/Pt(N)	11.3	[100]
Mn_3Ir/CoFeB	14.8	[101]
IrO_2 (111)	4.7	This work

6.3 Conclusion

In conclusion, IrO_2 can efficiently switch PMA without needing external fields. This has large implications for efficient spintronic memory applications as IrO_2 is among the lowest switching current densities of known materials to exhibit field-free PMA switching. Additionally, the control of PMA switching by changing the in-plane current direction with respect to the (111) surface can be used as an additional degree of freedom in spintronic applications.

Chapter 7 Summary and outlook

7.1 Summary of work

The work outlined in this thesis demonstrates the unique spintronic and orbitronic properties in high quality epitaxial IrO_2 thin films. This work highlights that low crystalline symmetry is not required for unconventional spin-orbit torques and can be generated in a non-magnetic high symmetry materials such as IrO_2 using epitaxial design. By reducing the relative crystalline symmetry with respect to the growth direction, large unconventional spin currents and hence spin-orbit torques can be generated. Furthermore, the spin polarizations detected in (001), (110), and (111) oriented IrO_2 thin films show which crystal symmetries restrict unconventional spin transport. Understanding and tuning unconventional spin transport generation in high symmetry materials can provide a new route towards energy-efficient magnetic switching in spintronic devices and the work presented can be used as guide for other high symmetry materials.

Another important aspect of this work is the relationship between theory and experimental work on spintronic properties. By experimentally comparing the conventional and unconventional spin-orbit torques in 5 orientations of IrO_2 including (001), (100), (101), (110), and (111) we fully determined the anisotropic spin Hall conductivity of IrO_2 experimentally and compared with theoretical DFT calculations. Using what we call the experimental SHC tensor determined from the (001) and (100) orientations, we accurately predicted both conventional and unconventional spin orbit-torques across all orientations, including the z-spin polarized torque. These results could provide insight into missing elements in the theoretical calculations and this approach can be used as a guide to discover large

unconventional spin-orbit torques in orientations that haven't been studied in other material systems.

Recent interest in orbital currents via the orbital Hall effect has demonstrated large effects in light metals, however, there have been very few studies in oxide systems as well as discussion on unconventional orbital Hall effects. We showed the crystallographic dependance of the OHC by studying spin torque ferromagnetic resonance (ST-FMR) on various IrO_2 orientations with Ni as our ferromagnetic layer. Additionally, we studied the ST-FMR results in samples with Pt/Py/Pt layers, where the Pt acts as an orbital-spin conversion layer. In comparison with theoretical calculations, we find experimental agreement for the OHC and SHC in the (001) and (100) orientations. We also find orbital contributions for the unconventional out-of-plane polarization in the (111) orientation. These results can provide alternative approaches for highly efficient low power spintronic devices.

7.2 Outlook and future directions

Recent work has shown IrO_2 to be a promising candidate for unconventional spin orbit torque (SOT) generation. Due to the lowering of crystal symmetry when IrO_2 is grown along low symmetry direction, unconventional SOTs can be observed[57]. The strength of these unconventional SOTs, however, are fixed due to fixed strain from the lattice mismatch. Membrane fabrication, a new approach in thin film techniques, can be used to further study and manipulate the strength of these SOTs for spintronic devices[102–107]. For example, if we consider the (001) orientation seen in Figure 7.1a, if we apply uniaxial strain along 1 direction, we can break the fourfold out-of-plane symmetry within the material. Similarly, if we

consider the (111) orientation seen in Figure 7.1b and c, we can apply strain along the (1-10) mirror plane or away from this plane to manipulate the crystal symmetry of our system.

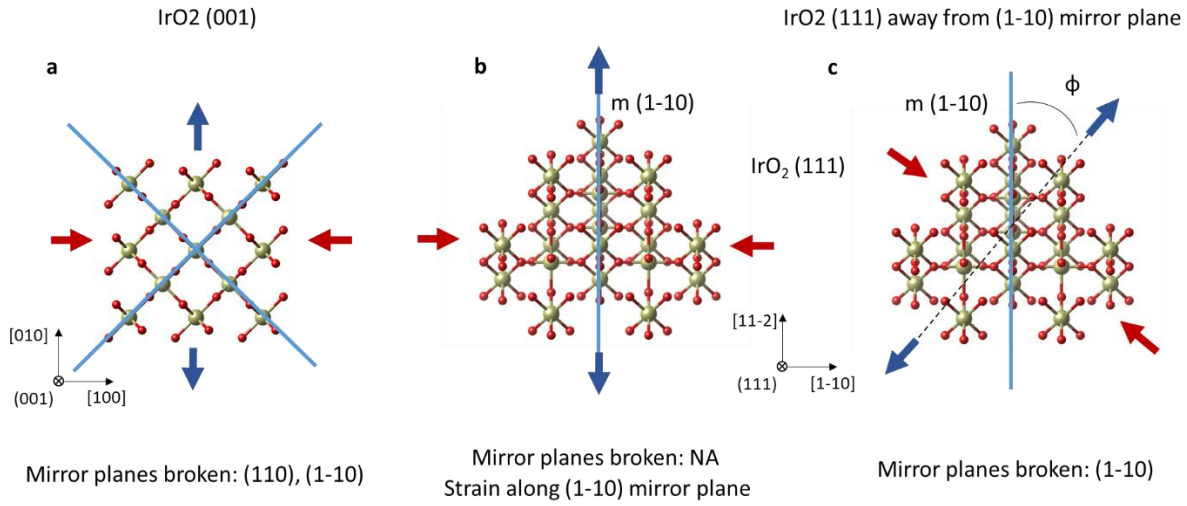

Figure 7.1: strain mediation in IrO_2 in a, (001) and in b-c, (111).

High quality IrO_2 thin films have already been grown and measured as seen in Chapter 2. Recent work has shown fabrication of TiO_2 membranes using VO_2 as a sacrificial layer that can be etched using a hydrogen peroxide (H2O2) solution[108]. The next step is to fabricate membranes using a VO_2 sacrificial layer outlined in Figure 7.2a-e. First, VO_2 and TiO_2 thin films are grown on TiO_2 substrates. Next, IrO_2 and Py are grown on the template. Device fabrication is then done etching down to the VO_2 layer using ion milling techniques and then electrodes are grown. Finally, the VO_2 can be etch using H_2O_2 and the devices can be transferred to Kapton films.

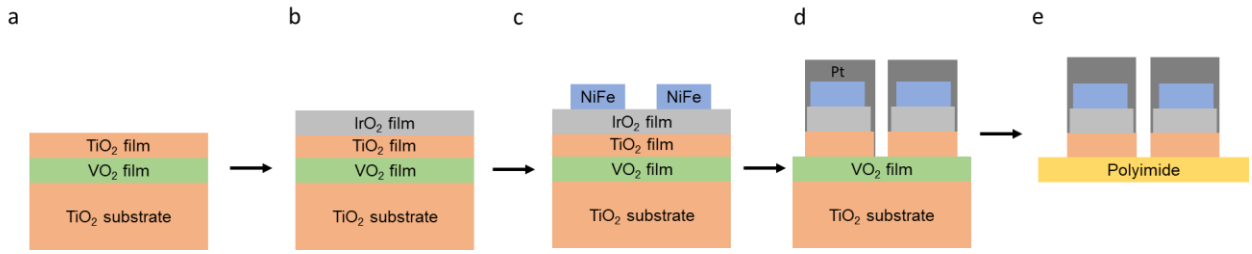

Figure 7.2: Membrane fabrication process using VO2 sacrificial layer.

High quality IrO_2 heterostructures have been made as seen by the out-of-plane HR-XRD of the (002) peaks in Figure 7.3. On the left we see the IrO_2 film peak and on the right we see the VO_2 peak. During growth, a thin TiO_2 layer was grown between the VO_2 and IrO_2 layers to protect the VO_2 from degrading during the IrO_2 growth which has been experienced in the past. During the membrane fabrication process, however, many bubbles form during the H2O2 etching process due to the oxygen evolution reaction IrO_2 is known for. These bubbles causes many cracks and non-uniform etching of the VO_2 layer. Further optimization of this process is required to make high quality and large scale IrO_2 membranes for ST-FMR measurements.

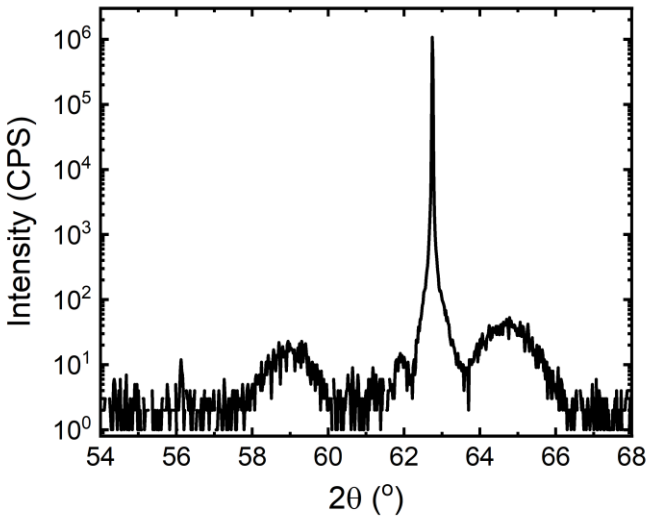

Figure 7.3: Out-of-plane XRD of the (002) peaks for IrO_2 film (left), TiO_2 substrate (middle), and VO_2 film (right).

Once the devices have been transferred to Kapton films, the membranes can be stretched using a custom built strain setup seen in Figure 7.4 following the design used in a recent study[109]. This setup includes four micromanipulators each with extended arms that can be used to clamp the edges of the Kapton film. For uniaxial strain, only two micromanipulators opposite from one another can be used to stretch the Kapton film which the other two apply partial strain to keep the Kapton film flat. For biaxial strain, all four micromanipulators can be used. For this strain setup, we can achieve up to ~7-8% strain which is only limited due to the tensile failure of the Kapton film above these strains. In order to do measurements such as ST-FMR, however, we need to lock in the strain states in order to move it to another testing location. To do this, we have included a heater block which can heat up polycaprolactone pellets, which become viscous about ~110° C. By applying strain to the membrane while slowly making contact with the viscous polycaprolactone, we can cool the polycaprolactone

where it becomes rigid at room temperature, allowing us to maintain the strained state which we can then use for a variety of measurements.

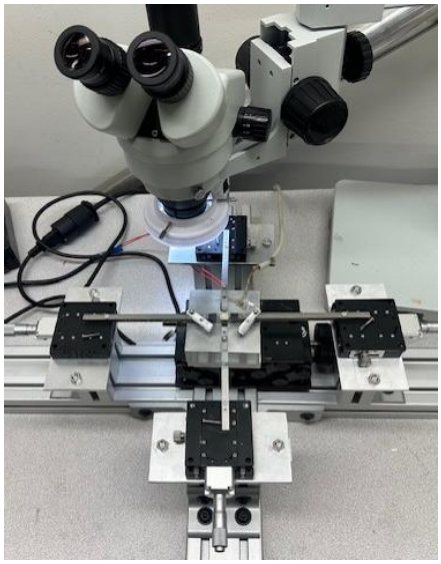

Figure 7.4: membrane strain setup using four micromanipulators, a heating block, and an optical microscope for precise strain states.

7.3 Concluding remarks

IrO_2 hosts many unique spin and orbital transport properties making it useful for spintronic applications and devices. The work outlined in this thesis aims to study these properties in a systematic approach to exploit the crystal symmetries using epitaxial design. Although the evidence of unconventional SOTs and orbital currents have been experimentally observed, more efforts into device structures could show the usefulness of IrO_2 in spintronic applications such as switching perpendicular magnetic materials and neuromorphic computing. Additionally, IrO_2 has the potential to be used for flexo-spintronics devices following successful large scale membrane fabrication that can be used for a variety of flexo-electronics and sensor applications. Beyond IrO_2, oxide systems host many unique electronic, spintronic, magnetic, piezoelectric, multiferroic, and other properties that can be

further studied using the approaches seen throughout this thesis. Other oxide materials that could benefit from further research into the spin and orbital properties include RuO_2, $BiFeO_3$, and $KTaO_3$, as well as doped oxide systems, which could show the benefits of using oxide platforms in spintronic applications.

References

1. Liu, L. *et al.* Spin-Torque Switching with the Giant Spin Hall Effect of Tantalum. *Science* **336**, 555–558 (2012).

2. Pai, C.-F. *et al.* Spin transfer torque devices utilizing the giant spin Hall effect of tungsten. *Appl. Phys. Lett* **101**, 122404 (2012).

3. Liu, L., Lee, O. J., Gudmundsen, T. J., Ralph, D. C. & Buhrman, R. A. Current-Induced Switching of Perpendicularly Magnetized Magnetic Layers Using Spin Torque from the Spin Hall Effect. *Phys Rev Lett* **109**, (2012).

4. Kao, I.-H. *et al.* Deterministic switching of a perpendicularly polarized magnet using unconventional spin-orbit torques in WTe 2. *Nat Mater* **21**, 1029–1034 (2022).

5. Shi, S. *et al.* Observation of the Out-of-Plane Polarized Spin Current from CVD Grown WTe2. *Adv Quantum Technol* **4**, 2100038 (2021).

6. MacNeill, D. *et al.* Control of spin–orbit torques through crystal symmetry in WTe2/ferromagnet bilayers. *Nat Phys* **13**, 300–305 (2017).

7. Zhao, B. *et al.* Unconventional Charge–Spin Conversion in Weyl-Semimetal WTe2. *Advanced Materials* **32**, 2000818 (2020).

8. Guimarã, M. H. D., Stiehl, G. M., Macneill, D., Reynolds, N. D. & Ralph, D. C. Spin−Orbit Torques in NbSe2/Permalloy Bilayers. *Nano Lett* **18**, 1311−1316 (2018).

9. Xue, F., Rohmann, C., Li, J., Amin, V. & Haney, P. Unconventional spin-orbit torque in transition metal dichalcogenide-ferromagnet bilayers from first-principles calculations. *Phys Rev B* **102**, 14401 (2020).

10. You, Y. *et al.* Cluster magnetic octupole induced out-of-plane spin polarization in antiperovskite antiferromagnet. *Nat Commun* **12**, (2021).

11. Bai, H. *et al.* Control of spin-orbit torques through magnetic symmetry in differently oriented noncollinear antiferromagnetic Mn3Pt. *Phys Rev B* **104**, 104401 (2021).

12. Liu, Y. *et al.* Current-induced Out-of-plane Spin Accumulation on the (001) Surface of the IrMn 3 Antiferromagnet. *Phys Rev Appl* **12**, 64046 (2019).

13. Nan, T. *et al.* Controlling spin current polarization through non-collinear antiferromagnetism. *Nat Commun* **11**, 4671 (2020).

14. Bose, A. *et al.* Tilted spin current generated by the collinear antiferromagnet ruthenium dioxide. *Nat Electron* **5**, 267–274 (2022).

15. Tshitoyan, V. *et al.* Electrical manipulation of ferromagnetic NiFe by antiferromagnetic IrMn. *Phys Rev B* **92**, 214406 (2015).

16. Zhang, W. *et al.* All-electrical manipulation of magnetization dynamics in a ferromagnet by antiferromagnets with anisotropic spin Hall effects. *Phys Rev B* **92**, 144405 (2015).

17. Jiang, D. *et al.* Substrate-induced spin-torque-like signal in spin-torque ferromagnetic resonance measurement. *Phys Rev Appl* **21**, (2024).

18. Liu, L., Moriyama, T., Ralph, D. C. & Buhrman, R. A. Spin-torque ferromagnetic resonance induced by the spin Hall effect. *Phys Rev Lett* **106**, (2011).

19. Nan, T. *et al.* Comparison of spin-orbit torques and spin pumping across NiFe/Pt and NiFe/Cu/Pt interfaces. *Phys Rev B Condens Matter Mater Phys* **91**, (2015).

20. Browning, R. *et al.* QUANTUM ESPRESSO: a modular and open-source software project for quantum simulations of materials. *J. Phys.: Condens. Matter* **21**, 395502 (2009).

21. Vanderbilt, D. Soft self-consistent pseudopotentials in a generalized eigenvalue formalism. *Phys Rev B* **41**, 7892–7895 (1990).

22. Perdew, J. P., Burke, K. & Ernzerhof, M. Generalized Gradient Approximation Made Simple. *Phys Rev Lett* **77**, 3865–3868 (1996).

23. Agapito, L. A., Ferretti, A., Calzolari, A., Curtarolo, S. & Nardelli, M. B. Effective and accurate representation of extended Bloch states on finite Hilbert spaces. *Phys Rev B* **88**, 165127 (2013).

24. Agapito, L. A., Ismail-Beigi, S., Curtarolo, S., Fornari, M. & Buongiorno Nardelli, M. Accurate tight-binding Hamiltonian matrices from ab initio calculations: Minimal basis sets. *Phys Rev B* **93**, 35104 (2016).

25. Fujiwara, K. *et al.* 5d Iridium Oxide As a Material for Spin-Current Detection. *Nat Commun* **4**, 1–6 (2013).

26. Bose, A. *et al.* Effects of Anisotropic Strain on Spin-Orbit Torque Produced by the Dirac Nodal Line Semimetal IrO2. *ACS Appl Mater Interfaces* **12**, 55411–55416 (2020).

27. Nelson, J. N. *et al.* Dirac nodal lines protected against spin-orbit interaction in IrO2. *Phys Rev Mater* **3**, 64205 (2019).

28. Xu, X. *et al*. Strong spin-orbit coupling and Dirac nodal lines in the three-dimensional electronic structure of metallic rutile IrO2. *Phys Rev B* **99**, 1–6 (2019).

29. Sun, Y., Zhang, Y., Liu, C. X., Felser, C. & Yan, B. Dirac nodal lines and induced spin Hall effect in metallic rutile oxides. *Phys Rev B* **95**, 1–7 (2017).

30. Xu, X. *et al*. Strong spin-orbit coupling and Dirac nodal lines in the three-dimensional electronic structure of metallic rutile IrO2. *Phys Rev B* **99**, 1–6 (2019).

31. Shao, Y. *et al*. Electronic correlations in nodal-line semimetals. doi:10.1038/s41567-020-0859-z.

32. Bose, A. *et al*. Effects of Anisotropic Strain on Spin-Orbit Torque Produced by the Dirac Nodal Line Semimetal IrO2. *ACS Appl Mater Interfaces* **12**, 55411–55416 (2020).

33. Nelson, J. N. *et al*. Dirac nodal lines protected against spin-orbit interaction in IrO2. *Phys Rev Mater* **3**, 64205 (2019).

34. Fujiwara, K. *et al*. 5d Iridium Oxide As a Material for Spin-Current Detection. *Nat Commun* **4**, 1–6 (2013).

35. Ueda, K. *et al*. Spin-orbit torque generation in NiFe/${\rm{Ir}}{{\rm{O}}_2}$ bilayers. *Phys Rev B* **102**, 134432 (2020).

36. Jiménez-Cavero, P. *et al*. Strong crystallographic influence on spin hall mechanism in pld-grown iro2 thin films. *Nanomaterials* **11**, (2021).

37. Baek, S.-H. C. *et al*. Spin currents and spin-orbit torques in ferromagnetic trilayers. *Nat Mater* **17**, 509–513 (2018).

38. Humphries, A. M. *et al*. Observation of spin-orbit effects with spin rotation symmetry. *Nat Commun* **8**, 911 (2017).

39. Grover, B., Hazra, K. & Ma, T. Crystallographic dependence of the spin Hall angle in epitaxial Pt films: Comparison of optical and electrical detection of spin-torque ferromagnetic resonance techniques. *Appl. Phys. Lett* **120**, 172406 (2022).

40. Ikebuchi, T., Shiota, Y. & Ono, T. Crystal orientation dependence of spin Hall angle in epitaxial Pt/FeNi systems. *Appl. Phys. Lett* **120**, 72406 (2022).

41. Sinova, J., Valenzuela, S. O., Wunderlich, J., Back, C. H. & Jungwirth, T. Spin Hall effects. *Rev Mod Phys* **87**, 1213–1260 (2015).

42. Liu, L., Moriyama, T., Ralph, D. C. & Buhrman, R. A. Spin-torque ferromagnetic resonance induced by the spin Hall effect. *Phys Rev Lett* **106**, 1–4 (2011).

43. Garello, K. *et al.* Symmetry and magnitude of spin-orbit torques in ferromagnetic heterostructures. *Nat Nanotechnol* **8**, 587–593 (2013).

44. Zhu, L., Zhu, L., Sui, M., Ralph, D. C. & Buhrman, R. A. Variation of the giant intrinsic spin Hall conductivity of Pt with carrier lifetime. *Sci Adv* **5**, (2019).

45. Zhu, L. & Buhrman, R. A. Maximizing Spin-Orbit-Torque Efficiency of Pt/Ti Multilayers: Trade-Off Between Intrinsic Spin Hall Conductivity and Carrier Lifetime. *Phys Rev Appl* **10**, 51002 (2019).

46. Fukami, S., Anekawa, T., Zhang, C. & Ohno, H. A spin-orbit torque switching scheme with collinear magnetic easy axis and current configuration. *NATURE NANOTECHNOLOGY* | **11**, (2016).

47. Humphries, A. M. *et al.* Observation of spin-orbit effects with spin rotation symmetry. *Nat Commun* **8**, 911 (2017).

48. MacNeill, D. *et al.* Control of spin–orbit torques through crystal symmetry in WTe2/ferromagnet bilayers. *Nat Phys* **13**, 300–305 (2017).

49. Stiehl, G. M. *et al.* Current-Induced Torques with Dresselhaus Symmetry Due to Resistance Anisotropy in 2D Materials. *ACS Nano* **13**, 2599−2605 (2019).

50. Liu, Y. *et al.* Current-induced Out-of-plane Spin Accumulation on the (001) Surface of the IrMn 3 Antiferromagnet. *Phys Rev Appl* **12**, 64046 (2019).

51. Nan, T. *et al.* Controlling spin current polarization through non-collinear antiferromagnetism. *Nat Commun* **11**, 4671 (2020).

52. Zhao, B. *et al.* Unconventional Charge–Spin Conversion in Weyl-Semimetal WTe2. *Advanced Materials* **32**, 2000818 (2020).

53. Liu, L. *et al.* Symmetry-dependent field-free switching of perpendicular magnetization. *Nat Nanotechnol* **16**, 277–282 (2021).

54. You, Y. *et al.* Cluster magnetic octupole induced out-of-plane spin polarization in antiperovskite antiferromagnet. *Nat Commun* **12**, 6524 (2021).

55. Bai, H. *et al.* Control of spin-orbit torques through magnetic symmetry in differently oriented noncollinear antiferromagnetic Mn3Pt. *Phys Rev B* **104**, 104401 (2021).

56. Bose, A. *et al.* Tilted spin current generated by the collinear antiferromagnet ruthenium dioxide. *Nat Electron* **5**, 267–274 (2022).

57. Patton, M. *et al.* Symmetry Control of Unconventional Spin–Orbit Torques in IrO2. *Advanced Materials* **35**, (2023).

58. Baek, S.-H. C. *et al.* Spin currents and spin-orbit torques in ferromagnetic trilayers. *Nat Mater* **17**, 509–513 (2018).

59. Stiehl, G. M. *et al.* Layer-dependent spin-orbit torques generated by the centrosymmetric transition metal dichalcogenide β-MoTe2. *Phys Rev B* **100**, 184402 (2019).

60. Zhao, T. *et al.* Enhancement of Out-of-Plane Spin–Orbit Torque by Interfacial Modification. *Advanced Materials* **35**, (2023).

61. Guimarã, M. H. D., Stiehl, G. M., Macneill, D., Reynolds, N. D. & Ralph, D. C. Spin−Orbit Torques in NbSe2/Permalloy Bilayers. *Nano Lett* **18**, 1311−1316 (2018).

62. Kontani, H., Naito, M., Hirashima, D. S., Yamada, K. & Inoue, J. Study of intrinsic spin and orbital Hall effects in Pt based on a (6s, 6p, 5d) tight-binding model. (2007) doi:10.1143/JPSJ.76.103702.

63. Zhu, L., Ralph, D. C. & Buhrman, R. A. Spin-Orbit Torques in Heavy-Metal-Ferromagnet Bilayers with Varying Strengths of Interfacial Spin-Orbit Coupling. *Phys Rev Lett* **122**, (2019).

64. Go, D., Jo, D., Lee, H. W., Kläui, M. & Mokrousov, Y. Orbitronics: Orbital currents in solids. *EPL* vol. 135 Preprint at https://doi.org/10.1209/0295-5075/ac2653 (2021).

65. Jo, D., Go, D., Choi, G.-M. & Lee, H.-W. Spintronics meets orbitronics: Emergence of orbital angular momentum in solids. *npj Spintronics* **2**, 19 (2024).

66. Bernevig, B. A., Hughes, T. L. & Zhang, S. C. Orbitronics: The intrinsic orbital current in p-doped silicon. *Phys Rev Lett* **95**, 3–6 (2005).

67. Kontani, H., Tanaka, T., Hirashima, D. S., Yamada, K. & Inoue, J. Giant orbital hall effect in transition metals: Origin of large spin and anomalous hall effects. *Phys Rev Lett* **102**, (2009).

68. Go, D., Jo, D., Kim, C. & Lee, H. W. Intrinsic Spin and Orbital Hall Effects from Orbital Texture. *Phys Rev Lett* **121**, (2018).

69. Canonico, L. M., Cysne, T. P., Rappoport, T. G. & Muniz, R. B. Two-dimensional orbital Hall insulators. *Phys Rev B* **101**, 1–5 (2020).

70. Bhowal, S. & Vignale, G. Orbital Hall effect as an alternative to valley Hall effect in gapped graphene. *Phys Rev B* **103**, 1–8 (2021).

71. Busch, O., Mertig, I. & Göbel, B. Orbital Hall effect and orbital edge states caused by s electrons. *Phys Rev Res* **5**, (2023).

72. Choi, Y. G. *et al.* Observation of the orbital Hall effect in a light metal Ti. *Nature* **619**, 52–56 (2023).

73. Lyalin, I., Alikhah, S., Berritta, M., Oppeneer, P. M. & Kawakami, R. K. Magneto-Optical Detection of the Orbital Hall Effect in Chromium. *Phys Rev Lett* **131**, 156702 (2023).

74. Ding, S. *et al.* Observation of the Orbital Rashba-Edelstein Magnetoresistance. *Phys Rev Lett* **128**, 67201 (2022).

75. Ding, S., Noël, P., Krishnaswamy, G. K. & Gambardella, P. Unidirectional orbital magnetoresistance in light-metal-ferromagnet bilayers. *Phys Rev Res* **4**, (2022).

76. Sala, G., Wang, H., Legrand, W. & Gambardella, P. Orbital Hanle Magnetoresistance in a 3d Transition Metal. *Phys Rev Lett* **131**, 156703 (2023).

77. Hayashi, H. & Ando, K. Orbital Hall magnetoresistance in Ni/Ti bilayers. *Appl Phys Lett* **123**, (2023).

78. Ding, S. *et al.* Harnessing Orbital-to-Spin Conversion of Interfacial Orbital Currents for Efficient Spin-Orbit Torques. *Phys Rev Lett* **125**, 177201 (2020).

79. Kim, J. *et al.* Nontrivial torque generation by orbital angular momentum injection in ferromagnetic-metal/ Cu/Al2 O3 trilayers. *Phys Rev B* **103**, (2021).

80. Lee, S. *et al.* Efficient conversion of orbital Hall current to spin current for spin-orbit torque switching. *Commun Phys* **4**, (2021).

81. Lee, D. *et al.* Orbital torque in magnetic bilayers. *Nat Commun* **12**, 1–8 (2021).

82. Sala, G. & Gambardella, P. Giant orbital Hall effect and orbital-to-spin conversion in 3d, 5d, and 4f metallic heterostructures. *Phys Rev Res* **4**, (2022).

83. Hayashi, H. *et al.* Observation of long-range orbital transport and giant orbital torque. *Commun Phys* **6**, (2023).

84. Bose, A. *et al.* Detection of long-range orbital-Hall torques. *Phys Rev B* **107**, 23–27 (2023).

85. Go, D. & Lee, H. W. Orbital torque: Torque generation by orbital current injection. *Phys Rev Res* **2**, (2020).

86. Jo, D., Go, D. & Lee, H. W. Gigantic intrinsic orbital Hall effects in weakly spin-orbit coupled metals. *Phys Rev B* **98**, 1–11 (2018).

87. Go, D. *et al*. Long-Range Orbital Torque by Momentum-Space Hotspots. *Phys Rev Lett* **130**, (2023).

88. %immer, E., Krakauer, H., Weinert, M. & Freeman, A. J. *Full-Potential Self-Consistent Linearized-Augmented-Plane-Wave Method for Calculating the Electronic Structure of Molecules and Surfaces: 02 Molecule*. *PHYSICAL REVIEW B* vol. 24 (1981).

89. Perdew, J. P., Burke, K. & Ernzerhof, M. *Generalized Gradient Approximation Made Simple*. (1996).

90. Pizzi, G. *et al*. Wannier90 as a community code: New features and applications. *Journal of Physics Condensed Matter* **32**, (2020).

91. Freimuth, F., Mokrousov, Y., Wortmann, D., Heinze, S. & Blügel, S. Maximally localized Wannier functions within the FLAPW formalism. *Phys Rev B Condens Matter Mater Phys* **78**, (2008).

92. Go, D., Lee, H. W., Oppeneer, P. M., Blügel, S. & Mokrousov, Y. First-principles calculation of orbital Hall effect by Wannier interpolation: Role of orbital dependence of the anomalous position. *Phys Rev B* **109**, (2024).

93. Wang, F. *et al*. Field-free switching of perpendicular magnetization by two-dimensional PtTe2/WTe2 van der Waals heterostructures with high spin Hall conductivity. *Nat Mater* (2024) doi:10.1038/s41563-023-01774-z.

94. Liu, Y. *et al*. Field-free switching of perpendicular magnetization at room temperature using out-of-plane spins from TaIrTe4. *Nat Electron* (2023) doi:10.1038/s41928-023-01039-2.

95. Xue, F. *et al*. Field-free spin-orbit torque switching assisted by in-plane unconventional spin torque in ultrathin [Pt/Co] N. doi:10.1038/s41467-023-39649-1.

96. Xie, Q. *et al*. Field-free magnetization switching induced by the unconventional spin-orbit torque from WTe2. *APL Mater* **9**, 51114 (2021).

97. Kao, I.-H. *et al*. Field-free deterministic switching of a perpendicularly polarized magnet using unconventional spin-orbit torques in WTe2.

98. Meng, D. *et al.* Field-Free Spin-Orbit Torque Driven Perpendicular Magnetization Switching of Ferrimagnetic Layer Based on Noncollinear Antiferromagnetic Spin Source. *Adv Electron Mater* **10**, (2024).

99. Zhang, Y. *et al. Room Temperature Field-Free Switching of Perpendicular Magnetization through Spin-Orbit Torque Originating from Low-Symmetry Type II Weyl Semimetal*. https://www.science.org (2023).

100. Bai, H. *et al.* Current Induced Field-Free Switching in a Magnetic Insulator with Enhanced Spin-Orbit Torque. *Adv Electron Mater* (2024) doi:10.1002/aelm.202300785.

101. Pu, Y. *et al.* Field-Free Switching of Perpendicular Magnetization by Anisotropic Spin Hall Effect in Mn3Ir. *Adv Funct Mater* (2024) doi:10.1002/adfm.202400143.

102. Heidler, J. *et al.* Manipulating magnetism in La 0.7 Sr 0.3 MnO 3 via piezostrain. *Phys Rev B* **91**, 24406 (2015).

103. Nan, T. *et al.* A Strain-Mediated Magnetoelectric-Spin-Torque Hybrid Structure. *Adv Funct Mater* **29**, (2019).

104. Li, M. *et al.* An Ultrathin Flexible Programmable Spin Logic Device Based on Spin – Orbit Torque. (2023) doi:10.1021/acs.nanolett.3c00231.

105. Chiabrera, F. M. *et al.* Freestanding Perovskite Oxide Films: Synthesis, Challenges, and Properties. *Ann Phys* **534**, (2022).

106. Hao, Q. *et al.* 2D Magnetic Heterostructures and Emergent Spintronic Devices. *Adv Electron Mater* **8**, (2022).

107. Sierra, J. F., Fabian, J., Kawakami, R. K., Roche, S. & Valenzuela, S. O. Spin dynamics in 2D materials Van der Waals heterostructures for spintronics and opto-spintronics. doi:10.1038/s41565-021-00936-x.

108. Lee, D. K. *et al.* Heterogeneous integration of single-crystalline rutile nanomembranes with steep phase transition on silicon substrates. *Nat Commun* **12**, (2021).

109. Sae Hong, S. *et al. Extreme Tensile Strain States in La 0.7 Ca 0.3 MnO 3 Membranes*. https://www.science.org.

Appendix

Appendix Note 1: Tensor rotation from the (001) basis to other orientations

Spin Torque Conductivity for IrO_2 (001)

$\hat{X} = [100], \hat{Y} = [010], \hat{Z} = [001]$

$$\tau^x = \begin{pmatrix} 0 & 0 & 0 \\ 0 & 0 & b \\ 0 & -a & 0 \end{pmatrix} \quad \tau^y = \begin{pmatrix} 0 & 0 & -b \\ 0 & 0 & 0 \\ a & 0 & 0 \end{pmatrix} \quad \tau^z = \begin{pmatrix} 0 & c & 0 \\ -c & 0 & 0 \\ 0 & 0 & 0 \end{pmatrix}$$

For E ∥ $\cos\psi\hat{x} + \sin\psi\hat{y}$, the in-plane spin = $-a\sin\psi\hat{x} + a\cos\psi\hat{y}$.

$\tau^y_{zx} = (-\sin\psi\hat{x} + \cos\psi\hat{y}) \cdot (-a\sin\psi\hat{x} + a\cos\psi\hat{y}) = a.$

$\tau^x_{zx} = 0.$

$\tau^z_{zx} = 0.$

Spin Torque Conductivity for IrO_2 (100)

$\hat{X} = [010],\ \hat{Y} = [001],\ \hat{Z} = [100]$

$$R = \begin{pmatrix} 0 & 1 & 0 \\ 0 & 0 & 1 \\ 1 & 0 & 0 \end{pmatrix}$$

$$\tau^x_{\square} = \begin{pmatrix} 0 & 0 & 0 \\ 0 & 0 & a \\ 0 & -b & 0 \end{pmatrix} \quad \tau^y_{\square} = \begin{pmatrix} 0 & 0 & -c \\ 0 & 0 & 0 \\ c & 0 & 0 \end{pmatrix} \quad \tau^z_{\square} = \begin{pmatrix} 0 & b & 0 \\ -a & 0 & 0 \\ 0 & 0 & 0 \end{pmatrix}$$

For E ∥ $\cos\psi\hat{x} + \sin\psi\hat{y}$, the in-plane spin = $-b\sin\psi\hat{x} + c\cos\psi\hat{y}$.

$\tau^y_{zx} = (-\sin\psi\hat{x} + \cos\psi\hat{y}) \cdot (-b\sin\psi\hat{x} + c\cos\psi\hat{y}) = (b\sin^2\psi + c\cos^2\psi) = b + \cos^2\psi(c - b)$

$= 0.5(b + c) + 0.5(c - b)\cos 2\psi$

$\tau^x_{zx} = (\cos\psi\hat{x} + \sin\psi\hat{y}) \cdot (-b\sin\psi\hat{x} + c\cos\psi\hat{y}) = \sin\psi\cos\psi(c - b) = 0.5(c - b)\sin 2\psi.$

$\tau^z_{zx} = 0.$

Spin Torque Conductivity for IrO_2 (101)

$\hat{X} = \cos\theta[100] - \sin\theta[001],\ \hat{Y} = [010],\ \hat{Z} = \sin\theta[100] + \cos\theta[001]$

$\tan\theta = [001]$ lattice spacing/$[100]$ lattice spacing $= 0.7012,\ \sin\theta = 0.574,\ \cos\theta = 0.819$

$$R = \begin{pmatrix} \cos\theta & 0 & -\sin\theta \\ 0 & 1 & 0 \\ \sin\theta & 0 & \cos\theta \end{pmatrix}$$

$$\tau_{\square}^{x} = \begin{pmatrix} 0 & -\sin\theta\cos\theta(c-a) & 0 \\ \sin\theta\cos\theta(c-b) & 0 & b\cos^2\theta + c\sin^2\theta \\ 0 & -a\cos^2\theta - c\sin^2\theta & 0 \end{pmatrix}$$

$$\tau_{\square}^{y} = \begin{pmatrix} -\sin\theta\cos\theta(a-b) & 0 & -b\cos^2\theta - a\sin^2\theta \\ 0 & 0 & 0 \\ b\sin^2\theta + a\cos^2\theta & 0 & \sin\theta\cos\theta(a-b) \end{pmatrix}$$

$$\tau_{\square}^{z} = \begin{pmatrix} 0 & a\sin^2\theta + c\cos^2\theta & 0 \\ -b\sin^2\theta - c\cos^2\theta & 0 & -\sin\theta\cos\theta(c-b) \\ 0 & -\sin\theta\cos\theta(a-c) & 0 \end{pmatrix}$$

For E ∥ $\cos\psi\hat{x} + \sin\psi\hat{y}$, the in-plane spin = $\sin\psi(-a\cos^2\theta - c\sin^2\theta)\hat{x} + \cos\psi(b\sin^2\theta + a\cos^2\theta)\hat{y}$.

$\tau_{zx}^{y} = (-\sin\psi\hat{x} + \cos\psi\hat{y}) \cdot (\sin\psi(-a\cos^2\theta - c\sin^2\theta)\hat{x} + \cos\psi(b\sin^2\theta + a\cos^2\theta)\hat{y}) =$
$(a\cos^2\theta + c\sin^2\theta)\sin^2\psi + (b\sin^2\theta + a\cos^2\theta)\cos^2\psi$

$= (a\cos^2\theta + c\sin^2\theta) + \cos^2\psi\sin^2\theta(b-c)$

$= (a\cos^2\theta + c\sin^2\theta) + (1 + \cos2\psi)\sin^2\theta(b-c)/2$

$= \left(a\cos^2\theta + \frac{(c+b)}{2}\sin^2\theta\right) + \cos2\psi\sin^2\theta(b-c)/2$

$= 0.670a + 0.165(c+b) - \cos2\psi\ 0.165(c-b)$

$\tau_{zx}^{x} = (\cos\psi\hat{x} + \sin\psi\hat{y}) \cdot (\sin\psi(-a\cos^2\theta - c\sin^2\theta)\hat{x} + \cos\psi(b\sin^2\theta + a\cos^2\theta)\hat{y})$

$= -\sin\psi\cos\psi\sin^2\theta(c-b).$

$= -\sin2\psi\ 0.165(c-b).$

$\tau_{zx}^{z} = -\sin\psi\ \sin\theta\cos\theta(a-c) = -\sin\psi\ 0.47(a-c).$

Spin Torque Conductivity for IrO_2 (110)

$\hat{X} = \frac{1}{\sqrt{2}}([100] - [010]), \quad \hat{Y} = [00\bar{1}], \quad \hat{Z} = \frac{1}{\sqrt{2}}([100] + [010])$

$$R = \begin{pmatrix} \frac{1}{\sqrt{2}} & -\frac{1}{\sqrt{2}} & 0 \\ 0 & 0 & -1 \\ \frac{1}{\sqrt{2}} & \frac{1}{\sqrt{2}} & 0 \end{pmatrix}$$

$$\tau_{\square}^{x} = \begin{pmatrix} 0 & 0 & 0 \\ 0 & 0 & a \\ 0 & -b & 0 \end{pmatrix} \quad \tau_{\square}^{y} = \begin{pmatrix} 0 & 0 & -c \\ 0 & 0 & 0 \\ c & 0 & 0 \end{pmatrix} \quad \tau_{\square}^{z} = \begin{pmatrix} 0 & b & 0 \\ -a & 0 & 0 \\ 0 & 0 & 0 \end{pmatrix}$$

For E ∥ $\cos\psi\hat{x} + \sin\psi\hat{y}$, the in-plane spin = $-\sin\psi b\hat{x} + \cos\psi c\hat{y}$.

$\tau_{zx}^{y} = (-\sin\psi\hat{x} + \cos\psi\hat{y}) \cdot (-\sin\psi b\hat{x} + \cos\psi c\hat{y}) = b\sin^2\psi + c\cos^2\psi = b + \cos^2\psi(c - b)$

$= 0.5(b + c) + \cos 2\psi\ 0.5(c - b)$

$\tau_{zx}^{x} = (\cos\psi\hat{x} + \sin\psi\hat{y}) \cdot (-\sin\psi b\hat{x} + \cos\psi c\hat{y}) = 0.5\sin 2\psi(c - b).$

$\tau_{zx}^{z} = 0.$

Spin Torque Conductivity for IrO_2 (111)

$R \equiv [100]$ lattice spacing/$[001]$ lattice spacing =1.426.

$\hat{Z} = \frac{1}{\sqrt{2+(R)^2}}([100] + [010] + (R)[001]) = 0.498[100] + 0.498[010] + 0.710[001]$

$\hat{Y} = -0.707[100] + 0.707[010] + 0[001]$

$\hat{X} = [100] + [010] - 0.996(0.498[100] + \ 0.498[010] + 0.710[001])$

$$\rightarrow 0.502[100] + 0.502[010] - 0.704[001]$$

$$R = \begin{pmatrix} 0.502 & 0.502 & -0.704 \\ -0.707 & +0.707 & 0 \\ 0.498 & 0.498 & 0.710 \end{pmatrix}$$

$$\tau_{\square}^{x} = 0.502\left[\begin{pmatrix} 0.3535(a-b) & 0.498a & 0.3565b + 0.351a \\ -0.498b & 0 & 0.502b \\ -0.351b - 0.3565a & -0.502a & -0.3535(a-b) \end{pmatrix}\right]$$

$$+0.502\left[\begin{pmatrix} -0.3535(a-b) & 0.498a & -0.3565b - 0.351a \\ -0.498b & 0 & 0.502b \\ 0.351b + 0.3565a & -0.502a & 0.3535(a-b) \end{pmatrix}\right]$$

$$-0.704\left[\begin{pmatrix} 0 & 0.710c & 0 \\ -0.710c & 0 & -0.704c \\ 0 & 0.704c & 0 \end{pmatrix}\right]$$

$$= \left[\begin{pmatrix} 0 & 0.5(a-c) & 0 \\ 0.5(c-b) & 0 & 0.504b+0.496c \\ 0 & -0.504a-0.496c & 0 \end{pmatrix}\right]$$

$$\tau^{y}_{\square} = -0.707\left[\begin{pmatrix} 0.3535(a-b) & 0.498a & 0.3565b+0.351a \\ -0.498b & 0 & 0.502b \\ -0.351b-0.3565a & -0.502a & -0.3535(a-b) \end{pmatrix}\right]$$

$$+0.707\left[\begin{pmatrix} -0.3535(a-b) & 0.498a & -0.3565b-0.351a \\ -0.498b & 0 & 0.502b \\ 0.351b+0.3565a & -0.502a & 0.3535(a-b) \end{pmatrix}\right]$$

$$= \left[\begin{pmatrix} -0.5(a-b) & 0 & -0.504b-0.496a \\ 0 & 0 & 0 \\ 0.504a+0.496b & 0 & 0.5(a-b) \end{pmatrix}\right]$$

$$\sigma^{z} = 0.498\left[\begin{pmatrix} 0.3535(a-b) & 0.498a & 0.3565b+0.351a \\ -0.498b & 0 & 0.502b \\ -0.351b-0.3565a & -0.502a & -0.3535(a-b) \end{pmatrix}\right]$$

$$+0.498\left[\begin{pmatrix} -0.3535(a-b) & 0.498a & -0.3565b-0.351a \\ -0.498b & 0 & 0.502b \\ 0.351b+0.3565a & -0.502a & 0.3535(a-b) \end{pmatrix}\right]$$

$$+0.710\left[\begin{pmatrix} 0 & 0.710c & 0 \\ -0.710c & 0 & -0.704c \\ 0 & 0.704c & 0 \end{pmatrix}\right]$$

$$= \left[\begin{pmatrix} 0 & 0.496a+0.504c & 0 \\ -0.496b-0.504c & 0 & -0.5(c-b) \\ 0 & -0.5(a-c) & 0 \end{pmatrix}\right]$$

For E ∥ $\cos\psi\hat{x} + \sin\psi\hat{y}$, the in-plane spin $= [\sin\psi(-0.504a - 0.496c)]\hat{x} + [\cos\psi(0.504a + 0.496b)]\hat{y}$.

$$\tau^{y}_{zx} = (-\sin\psi\hat{x} + \cos\psi\hat{y}) \cdot ([\sin\psi(-0.504a - 0.496c)]\hat{x} + [\cos\psi(0.504a + 0.496b)]\hat{y})$$

$$= \sin^2\psi(0.504a + 0.496c) + \cos^2\psi(0.504a + 0.496b)$$

$$= (0.504a + 0.496c) - \cos^2\psi(0.496(c-b))$$

$$= 0.504a + 0.248c + 0.248b - \cos 2\psi(0.248(c-b))$$

$$\tau^{x}_{zx} = (\cos\psi\hat{x} + \sin\psi\hat{y}) \cdot ([\sin\psi(-0.504a - 0.496c)]\hat{x} + [\cos\psi(0.504a + 0.496b)]\hat{y}) =$$

$$= -\cos\psi\sin\psi\ 0.496(c-b) = -\sin 2\psi\ 0.248(c-b)$$

$$\tau^{z}_{zx} = -\sin\psi(0.5(a-c))$$